Advanced Geometries by Additive Manufacturing and Topology Optimization for Internal Cooling of Gas Turbine Airfoil

by

Sarwesh Narayan Parbat

Bachelor of Technology in Mechanical Engineering, SRM University, India, 2011

Master of Science in Mechanical Engineering, University of Pittsburgh, US, 2015

Submitted to the Graduate Faculty of the

Swanson School of Engineering in partial fulfillment

of the requirements for the degree of

Doctor of Philosophy

University of Pittsburgh

2022

UNIVERSITY OF PITTSBURGH

SWANSON SCHOOL OF ENGINEERING

This dissertation was presented

by

Sarwesh Narayan Parbat

It was defended on

October 17, 2022

and approved by

Dr. Sung Kwon Cho, PhD, Professor, Department of Mechanical Engineering and Materials Science

Dr. Xiayun Zhao, PhD, Assistant Professor, Department of Mechanical Engineering and Materials Science

Dr. Bruce Kang, PhD, Professor, Department of Mechanical and Aerospace Engineering, West Virginia University

Dissertation Director: Dr. Minking K. Chyu, PhD, Professor, Department of Mechanical Engineering and Materials Science

Advanced Geometries by Additive Manufacturing and Topology Optimization for Internal Cooling of Gas Turbine Airfoil

Sarwesh Narayan Parbat, PhD

University of Pittsburgh, 2022

In the past few decades, the growth in the ability of materials to retain strength at high temperatures has occurred remarkably slower than the rise in combustion temperature in gas turbine engines. With an aim to attain overall cycle efficiency of 65% in the next few years, the gas turbine inlet temperature is slated to reach in excess of 1700^{o} C. As a result, there is a need to identify innovative and more effective cooling technologies for the hot gas path components, such as airfoils, to maintain them within their working thermal envelope.

The presented research developed and demonstrated that advanced lattice geometries fabricated by direct metal laser sintering (DMLS) based additive manufacturing (AM) process could be effectively used in the cooling of gas turbine airfoils. The effect of unit cell topology, ligament diameter, and orientation with respect to fluid flow on the aerothermal performance of these geometries was investigated. In addition, a new type of integrated cooling architecture was also developed by combining AM fabricated transpiration and lattice geometries. This architecture could simultaneously provide external and internal cooling to the airfoils while also alleviating the harmful effects of pore blockage, which is a limiting factor with transpiration-based cooling. Three state-of-the-art experimental techniques and detailed numerical analysis were utilized to characterize the performance of these geometries.

Finally, a new topology optimization (TO) method based on second law analysis was proposed to optimize the overall aerothermal performance of lattice geometries. Within this method, the relative strength of heat transfer and dissipative losses was calculated using local

entropy generation rates. A set of criteria was proposed to precisely isolate high-dissipation fluid regions and modify them to suppress form-losses and improve local heat transfer, yielding the optimized topology. The proposed TO method presented several advantages: 1) the method could be implemented as a post-process script, thus eliminating the need for a custom solver, 2) optimization could be performed on prespecified geometries in a high Reynolds number flow, and 3) it provided a quantitative insight into the best operating point for a given geometry in terms of inlet flow conditions.

Table of Contents

Acknowledgments ..... **xvi**

1.0 Introduction **1**

1.1 Gas Turbine Engines and the Need for Cooling **1**

1.1.1 Internal Cooling of Gas Turbine Components using Extended Surfaces **3**

1.1.2 External Cooling **8**

1.2 Topology Optimization **10**

1.3 Statement of Research **15**

1.3.1 Study of Conjugate Aerothermal Performance **15**

1.3.2 Investigation of Local Heat Transfer Coefficient on End Wall **16**

1.3.3 Propose Novel Integrated Lattice-Transpiration Cooling Architecture **16**

1.3.4 Propose Second Law Analysis of Lattice Geometries and Perform Topology Optimization **17**

2.0 Conjugate Heat Transfer in Additively Manufactured Lattices: Effect of Topology, Diameter, and Orientation **19**

2.1 Unit Cell and Lattice Geometries **19**

2.2 Fabrication of Test Coupons Using DMLS AM Process **28**

2.3 Build Quality and Roughness Characterization **30**

2.4 Experimental Technique and Methodology **34**

2.5 Results and Discussions **39**

2.5.1 Effect of AM Roughness on Heat Transfer **39**

2.5.2 Heat Transfer in Lattice Geometries **40**

2.5.3 Pressure Drop in Lattice Geometries 45

2.5.4 Augmentation in Heat Transfer and Pressure Drop 48

3.0 Investigation of End Wall Heat Transfer Coefficient in Lattice Geometries: Effect of Topology and Orientation 58

3.1 Scaled-up Lattice Geometries..... 59

3.2 Fabrication of Lattice Samples using Stereolithography (SLA) AM Process..... 61

3.3 Experimental Technique and Methodology 62

3.4 Experiment Results and Discussions 68

3.4.1 Heat Transfer in Baseline Pin Fins.....68

3.4.2 Local Distribution of Heat Transfer Coefficient on End Walls of Lattice Channels.....70

3.4.3 Overall Averaged Heat Transfer Coefficient for Fully Developed Region...77

3.5 Numerical Analysis of Flow Field in Cooling Channels with Lattice Geometries . 79

3.6 Numerical Flow Field 84

4.0 Novel Integrated Lattice-Transpiration Cooling Architecture 90

4.1 Geometries..... 91

4.2 Experimental Technique and Methodology 94

4.2.1 Test Plate for The Plenum-Fed Configuration.....97

4.2.2 Test Plate for Crossflow-Fed Configuration 97

4.3 Results and Discussions..... 101

4.3.1 Overall Cooling Effectiveness of Transpiration Only Coupons 101

4.3.2 Overall Cooling Effectiveness of Integrated Lattice-Transpiration Coupons 103

5.0 Second Law Analysis and Topology Optimization for Lattice Geometries..... 114

5.1 Lattice Geometry and Numerical Setup for Second Law Analysis 114

5.2 Effect of Filtering Criteria 121

5.3 Topology Optimization of Unit Cell Using Second Law Analysis..... 125

5.3.1 Proposed Topology Optimization Scheme and Implementation 125

5.3.2 Extracting Regions of Interest 126

5.3.3 Comparison of Performance 128

6.0 Conclusions and Future Work..... 134

6.1 Major Accomplishments 134

6.1.1 Conjugate Aerothermal Analysis of True-Scale Additively Manufactured Lattice Geometries 135

6.1.2 Impact of Lattice Topology and Orientation on End Wall Heat Transfer Coefficient 136

6.1.3 Novel Integrated Lattice-Transpiration Cooling Architectures and Characterization of Their Overall Cooling Effectiveness 137

6.1.4 Introduction of Second Law Based Analysis to Lattice Geometries and New Topology Optimization Scheme 138

6.2 Future Work 139

Bibliography 141

List of Tables

Table 2.1 Geometric details for baseline pin fins 27

Table 2.2 Geometric details of lattices 28

Table 2.3 Average roughness (Ra) values on different surfaces of DMLS coupons 34

Table 3.1 Key geometric parameters 61

Table 4.1 Summary of blowing ratio and crossflow rate for tested geometries 100

Table 5.1 Result of grid independence study 116

List of Figures

Figure 1.1 A typical gas turbine engine showing the different sections and close-up of the turbine stages [1,2]. 2

Figure 1.2 Cooling technologies implemented in a gas turbine airfoil [7] 3

Figure 2.1 Overview of the unit cell geometries and important parameters..... 21

Figure 2.2 Effect of rotation on the projected area of the unit cell 22

Figure 2.3 Overview of the lattices generated using the four types of unit cells and the three orientations used (shown here for d = 0.75 mm)..... 23

Figure 2.4 The layout of the two baseline pin fins (staggered array of 15 × 15 pins)..... 24

Figure 2.5 Details of the test coupon with embedded lattice geometry (shown for BC0-0.75 lattice)..... 25

Figure 2.6 Comparison of important geometrical parameters between lattices and baseline pin fins (black bars) 27

Figure 2.7 Overview of DMLS process and the EOS M290 system used in this research ... 29

Figure 2.8 (a) Sample unit cells fabricated to assess the impact of ligament diameter and build orientation on the quality, (b) successful build with 45° tilt and softer recoater blade 31

Figure 2.9 (Top) Cartoon depicting the 45° orientation, and (bottom) AM fabricated IN718 coupons on the build plate..... 32

Figure 2.10 Closeup of surface and sample of the measured surface profile for IN718 coupon fabricated using DMLS 33

Figure 2.11 Details of the test rig and the schematic of the test facility established for this research. (Left) cross-sectional view of the assembled test rig and external view of the rig, and (right) schematic of the test facility. 38

Figure 2.12 (a) Nu augmentation in DMLS fabricated smooth channels, and (b) validation of experiment based on correlation from [100] 40

Figure 2.13 Effect of the diameter on Nu for the tested lattice geometries 42

Figure 2.14 Effect of the orientation on Nu for the four lattice geometries 44

Figure 2.15 Effect of the diameter on f for the four lattice geometries 46

Figure 2.16 Effect of the orientation on f for the four lattice geometries 48

Figure 2.17 Augmentation in Nu for the tested lattices and baseline pin fins compared to the smooth channel correlation 51

Figure 2.18 Increase in f for the tested lattices and baseline pin fins compared to the smooth channel correlation 52

Figure 2.19 Plots depicting fin efficiency for the analyzed BC, FC, and Kagome geometries 53

Figure 2.20 Plots depicting fin effectiveness for the analyzed BC, FC, and Kagome geometries 54

Figure 2.21 Comparison between the overall performance of the lattices and baseline pin fin geometries 56

Figure 3.1 Lattices generated from the above unit cells for both 0^o and 45^o flow orientations. The unit cells are highlighted in red. 60

Figure 3.2 Sample of parts printed using the stereolithography method (a) FC45, (b) OCTA0, and (c) Kagome unit cells 62

Figure 3.3 Variation of green channel intensity with video frame. Savitzky-Golay filtering has been applied to minimize the effect of noise on determination of the frame number at peak intensity. 65

Figure 3.4 Sample test channel with embedded lattice 66

Figure 3.5 Test setup schematic for transient liquid crystal technique 68

Figure 3.6 Comparison of the overall $Nu_{D,ave}$ between the current experiment and literature data (top); comparison of row-wise averaged Nusselt number ratio between the experiments and literature data (bottom) 70

Figure 3.7 Local distribution of h on the end wall for lattice and baseline pin fin channel at Re ~ 11,600 71

Figure 3.8 Key features in the local h on end wall and for a single unit cell in fully developed region for BC lattices 73

Figure 3.9 Key features in the local h on end wall and for a single unit cell in fully developed region for FC lattices 74

Figure 3.10 Key features in the local h on end wall and for a single unit cell in fully developed region for OCTA lattices 76

Figure 3.11 Key features in the local h on end walls for Kagome lattice 77

Figure 3.12 Overall averaged Nu on the end wall for the tested lattices 78

Figure 3.13 Heat transfer enhancement compared with smooth channel correlation 79

Figure 3.14 BC0 lattice highlighting the planes of symmetry and the coordinate system for CFD 81

Figure 3.15 Meshed BC domain highlighting the different types of elements, domains, boundary conditions 83

Figure 3.16 Result of grid independence study for area averaged h and pressure drop using BC0 lattice..... 84

Figure 3.17 Velocity streamlines highlighting the sub-channel flow in BC, FC, and OCTA lattices with 0° and 45° orientations..... 86

Figure 3.18 For Kagome0, the top plate experienced a slower flow compared to bottom plate 87

Figure 3.19 Comparison of velocity field at the horizontal plane at H/2 for rows 2-4 87

Figure 3.20 Distribution of TKE on a xy plane 0.1H below the end wall, and the predicted h (inset)..... 88

Figure 4.1 Proposed integrated lattice-transpiration cooling architecture 91

Figure 4.2 (A) Example of the integrated architecture shown for FC lattice, (B) transpiration cooling holes blocked by lattice footprint, and (C) integrated cooling test coupons fabricated using DMLS and IN718 92

Figure 4.3 Close-up of Kagome_L and BC_L coupons showing the roughness on the ligaments (above), and holes blocked by lattice footprint in AM coupon (below).... 93

Figure 4.4 Schematic comparing the coolant flow in plenum-fed and crossflow-fed configurations..... 94

Figure 4.5 Overview of the wind tunnel with the test plate assembly installed 96

Figure 4.6 Plenum and test coupon assembly for PL-Fed configuration..... 97

Figure 4.7 Schematic of the crossflow-fed test plate assembly and the tested coupons..... 98

Figure 4.8 Comparison of overall cooling effectiveness between PL-fed transpiration only coupons..... 102

Figure 4.9 Comparison of overall cooling effectiveness between CF-fed transpiration only coupons..... 103

Figure 4.10 Local distribution of φ on integrated lattice-transpiration coupons in PL-fed configuration 104

Figure 4.11 Comparison between overall cooling effectiveness between integrated cooling coupons and the corresponding transpiration only coupons 105

Figure 4.12 Spanwise averaged effectiveness, φ, for the tested integrated coupons 108

Figure 4.13 Spanwise averaged overall effectiveness, φ, for the tested baseline coupon... 109

Figure 4.14 Overall cooling effectiveness for all the CF-fed integrated lattice coupons highlighting the impact of fixed crossflow with varying total flow 110

Figure 4.15 Overall cooling effectiveness for all the CF-fed integrated lattice coupons highlighting the impact of fixed total flow rate with varying crossflow 111

Figure 4.16 Comparison between the overall averaged φ for all the tested cases 112

Figure 5.1 Comparison of filtered fluid volume, V_{Be}, by selecting two different Be_{cutoff} and varying Re..... 117

Figure 5.2 The three zones in the channel based on flow field (shown for Be_{cutoff} = 0.01 and Re = 5000) 118

Figure 5.3 Effect of the filtering criterion on selection of fluid regions for Re = 11,800 and Be_{cutoff} = 0.025 120

Figure 5.4 Vortex flow and regions with u < 0 m/s in BC0 lattice..... 120

Figure 5.5 Plots comparing the cumulative change in volume and entropy generation rates of the filtered fluid region in Zone 2 using the three types of criteria at different Re 123

Figure 5.6 Comparison of fluid region (Re = 11,800) filtered by fixing the $S_f/S_{f,tot}$ = 0.025. The three resulting Be_{cutoff} values were 0.0075 for V_{Be}, 0.0585 for V_{vel}, and 0.0183 for V_Q. 124

Figure 5.7 Overview of the proposed topology optimization sccheme using the second law analysis 126

Figure 5.8 Selection of regions for topology optimization in BC0: (a) wake regions identified by u <= 0 m/s, and (b) after subtracting high Be regions (V_{vel}) 127

Figure 5.9 Exporting and converting the point cloud into solid domain to obtain the modified topology 128

Figure 5.10 Optimized BC unit cell topology 128

Figure 5.11 (Top) reduction in targetted low Be regions for 2nd row unit cell after TO. (Bottom) Comparison between original and modified topology simulation results. The x-axis represents the % change in BC0-Rev compared to the BC0 lattice..... 130

Figure 5.12 Comparison of total entropy generated by the two mechanisms between BC0 and BC0 Rev at different channel Re 131

Figure 5.13 Variation of entropy generation in each row vs channel Re for BC0 (above) and BC0-Rev (below) 132

Acknowledgments

Taking up this PhD has been an immensely life-changing experience for me and it definitely would have been impossible without the help and direction that I obtained from many people.

I would like to first and foremost thank Dr. Minking Chyu, my advisor, for believing in me and providing all the guidance, support, and motivation over these years. Without his constant guidance and feedback, this PhD would not have been achievable.

I would also like to express my gratitude towards Dr. Bruce Kang, Dr. Sung Kwon Cho, and Dr. Xiayun Zhao for taking out the time to be on my advisory committee and providing invaluable feedback during the dissertation period. I am also thankful to my labmates Dr. Min, Dr. Yang, and Dr. Xu for sharing their knowledge and passion for the subject with me. I am grateful to the US Department of Energy for the funding provided through the UTSR program, and also to the people at NETL, Morgantown, for their insightful discussions.

The work done during this PhD would not have been completed without the help from Andy, Brandon, and Jeff in fabricating the test samples and test rig components. Special thanks to my friends and roommates who made Pittsburgh feel like another home.

A heartful thanks you to my mother, father, sisters, and brothers-in-law for always believing in me, encouraging me to follow my dreams, and being there through this challenging period. I am highly indebted to them for pushing me to achieve my career goals.

1.0 Introduction

1.1 Gas Turbine Engines and the Need for Cooling

Gas turbine engines are one of the marvels of modern-day engineering and are the workhorse for the power and aviation industries. They are responsible for generating a significant part of the world's total energy requirements. Hence, increasing the overall efficiency of the gas turbine engines is one of the central focuses for realizing a low carbon emission future. A typical gas turbine engine is shown in Fig. 1.1 [1,2]. The ambient air is sucked from an air intake located at the front of the engine and is compressed to a high pressure in the compressor section. This high-pressure air is then supplied to the combustion chamber, where it is mixed with fuel and ignited to produce high-pressure and temperature combustion gases. These gases flow through a cascade of vanes and are directed to the turbine stages. The blades located in these stages have an airfoil shape and create lift when these gases flow over them, and in turn, rotate the turbine disc, thus converting thermal energy into mechanical work. The efficiency of these engines is dependent on the turbine inlet temperature (TIT), and it is predicted that the TIT will reach 1700^{o}C in order to achieve a 65% overall cycle efficiency [3]. Most of the superalloy materials used for fabricating critical hot gas path components for these engines are incapable of maintaining their mechanical properties at such high temperatures. Although there has been significant development in the superalloys which can retain their strength at high temperatures, they are far behind the corresponding rise in combustion temperature [4,5]. As a result, the components that are exposed to the hot combustion gases require additional cooling in order to maintain them within their thermal-mechanical performance envelope.

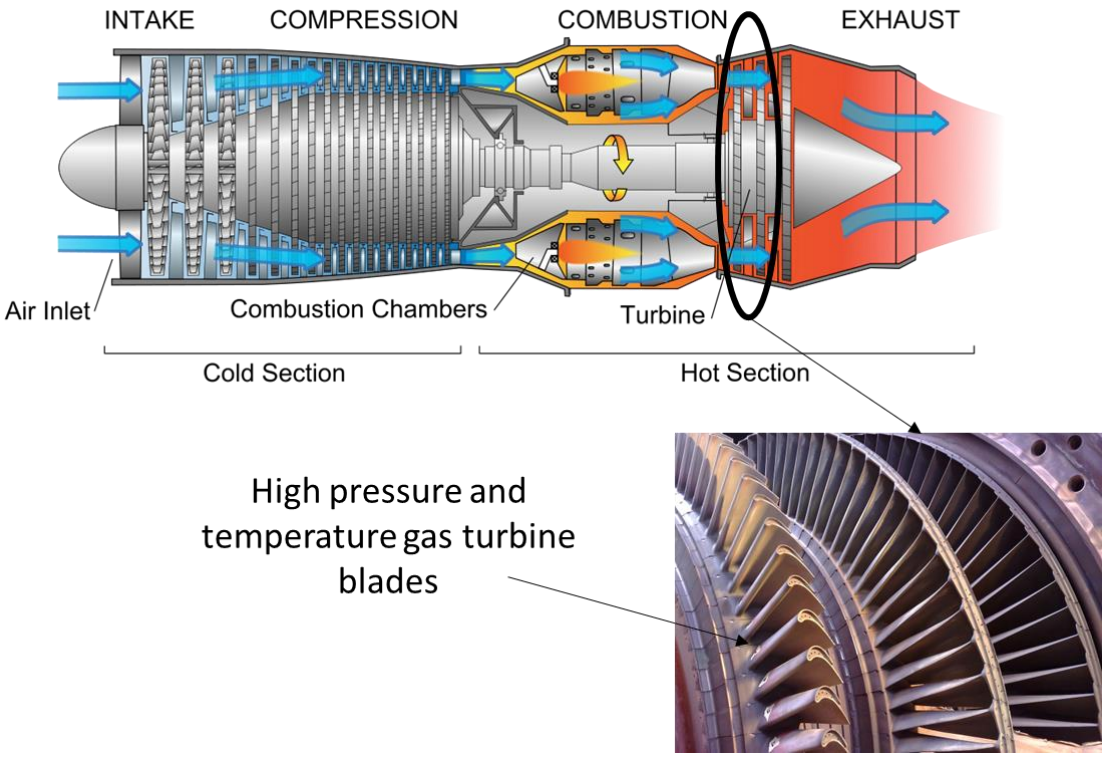

Figure 1.1 A typical gas turbine engine showing the different sections and close-up of the turbine stages [1,2].

Traditionally, the coolant supply comprises of air bled from one of the stages of the compressor and allowed to flow through the cooling channels located within the airfoil. This air, which can reach up to 20% of the total compressor flow rate [6], is unavailable for combustion, thereby reducing the work output and efficiency of the cycle. Thus, it is desirable to realize technologies that could provide high cooling at low coolant flow rates. A host of such cooling technologies are implemented within the gas turbine airfoil and vanes, as shown in Fig. 1.2 [7]. These technologies can be broadly classified into internal and external cooling.

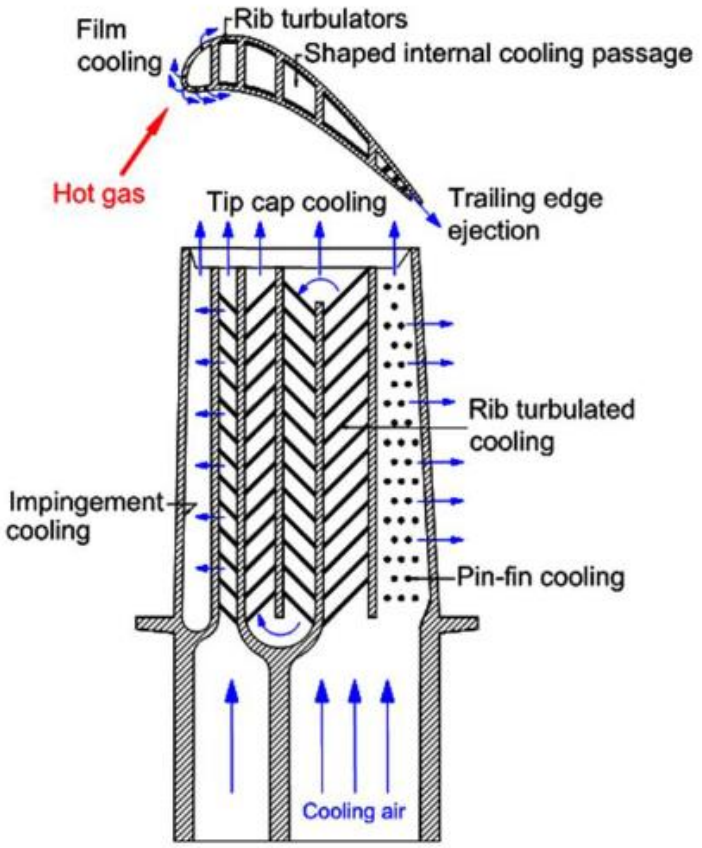

Figure 1.2 Cooling technologies implemented in a gas turbine airfoil [7]

1.1.1 Internal Cooling of Gas Turbine Components using Extended Surfaces

Internal cooling technologies are implemented in the form of channels that are embedded inside the airfoil. The cooling air is passed through these channels in order to pick up heat from their walls and provide the necessary cooling. The thermal load on a modern gas turbine airfoil is significant, as discussed in [4,8,9], and simple channel geometry could seldom meet the cooling needs since the heat transfer in such channels is limited. The heat transfer within these channels is augmented by adding special geometries, such as those reviewed in [6,8–10]. Among them, pin fin type extended surface geometries have been one of the most widely used due to their

multifunctional capability of providing simultaneous cooling and structural strengthening. Two important parameters associated with the performance of these geometries are fin effectiveness, ϵ_{fin}, and fin efficiency, η_{fin}. The effectiveness, ϵ_{fin}, can be defined as the ratio of the fin heat transfer rate to the heat transfer rate that would exist without the fin. On the other hand, fin efficiency, η_{fin}, is the ratio of fin heat transfer rate to the maximum possible heat transfer rate when the entire pin is at the same temperature as the base. These are given as [11],

$$\epsilon_{fin} = \frac{q_{fin}}{q_{smooth}} = \frac{M\, tanh\, mL}{hA(T_{wall} - T_{mean})} = \sqrt{\frac{4k}{hD}}\, tanh\, mL \qquad (1.1)$$

$$\eta_{fin} = \frac{q_{fin}}{q_{max}} = \frac{\tanh mL}{mL} \qquad (1.2)$$

where, q_{fin} is the heat transfer rate from the pin, q_{smooth} is heat transfer rate from wall without pin, T_{wall} is the average temperature of the channel wall, T_{mean} is the mean temperature of the bulk flow, L is the length of the pin, A is the surface area of the pin, h is the heat transfer coefficient, D is the pin diameter, and M and m are given as

$$M = \sqrt{hPkA}(T_{wall} - T_{mean}) \qquad (1.3)$$

$$m = \sqrt{\frac{hP}{kA}} = \sqrt{\frac{4h}{kD}} \qquad (1.4)$$

Here, k = thermal conductivity of the material, and P is the perimeter of the extended surface. As mentioned before, these geometries show the highest heat transfer when their surface is at a uniform temperature equal to the temperature at their base. The cylindrical body of the pins protrudes within the bulk flow and promotes turbulence and mixing in the coolant though flow separation and vortex shedding in the wake. At the same time, the near end wall flow interacts with the foot of the pins and forms what is known as a horse-shoe vortex, as reported in the literature [12–14]. These horse-shoe vortices near the end wall help in eroding away the boundary

layer and promote convective heat transfer on the end wall. The extended cylindrical body of the pin also provides additional surface area for heat transfer into the bulk coolant flow [11]. In addition to these heat transfer enhancement benefits, pin fins also play a role of structural load-bearing members and can be implemented in thinner sections of the airfoils, such as the trailing edge, to maintain desired levels of structural strength [6]. A lot of studies have been conducted to understand the heat transfer behavior in the pin fin geometries, and the impact of various parameters and geometries have been investigated [12,14–20]. The pin fins typically show a heat transfer enhancement of up to 5 times that of a smooth channel. One of the main reasons behind the popularity of these geometries is their compatibility with the investment casting process, which is one of the primary manufacturing processes for gas turbine airfoils [21]. However, in recent decades, the advancements in metal additive manufacturing processes have enabled the design and fabrication of much more complex geometries using traditional and new high-temperature superalloys. From a cooling perspective, this has opened up a larger design space that was previously inaccessible due to limitations of the investment casting and other traditional manufacturing processes. One of the outcomes of such new design freedom has been lattice-type geometries.

Lattices have typically been studied primarily as structural elements and as a means to improve strength to weight ratio in AM manufactured components [22–26]. However, in recent times, lattice-type geometries have garnered significant attention for application in internal cooling channels. Due to the complexity of their topology, these geometries have a very high surface area packed within a relatively small volume; thus, they provide high compactness, which is better than the current state-of-the-art pin fins. In addition, due to the presence of inclined ligaments, lattices can promote much higher mixing and turbulence within the bulk flow of the channel and achieve

favorable redistribution of the coolant through a complex network of open flow area. However, limited studies have focused on the characterization of heat transfer and pressure drop performance of such geometries, especially in the turbulent flow regime existing within the internal cooling channels of airfoils.

Kim et al. [27] studied an ultralight-weight lattice material. The authors showed through both experiments and numerical simulations that the formation of vortex structures, such as the horse-shoe vortex, and flow separation on the struts were the major factors for the observed thermal fluid characteristics. Gao et al. [28] used numerical simulations to show heat transfer enhancement due to the formation of multiform cortical structures within regular tetrahedral unit cells fabricated from carbon-fiber reinforced resin. Shen et al. [29] studied single layer Kagome and wire woven bulk Kagome lattices and showed the importance of topology in these lattices. Parbat et al. [30] studied two types of a single layer Kagome lattices fabricated using IN718 and DMLS process. They also concluded that complex vortical flows existed in such structures, which led to a high but asymmetrical heat transfer on the end walls. Liang et al. [31] experimentally compared the heat transfer in pin fins, BCC, and Kagome lattices embedded inside a rectangular channel. They showed that for a given porosity, the lattice structures provided 17% - 41% higher averaged Nusselt number on the end wall compared to the staggered pin fin arrays.

More recently, Liang et al. [32] have also performed conjugate heat transfer tests on the body center cubic (BCC), face centered cubic (FCC), X type lattice, and pin fin arrays. These were additively manufactured using selective laser melting (SLM) process. They concluded that for a given porosity, the BCC lattice provided the best alternative to the pin fin arrays. Xi et al. [33] studied the heat transfer performance in X-type lattices, and concluded that increasing the Reynolds number (Re) based on channel height, augmented the heat transfer while the friction

factor remained unaffected. Dixit et al. [34] numerically investigated 3D printed lattices comprising of simple-cubic, body-centered and face centered cubic trusses, and Kelvin and Octet lattices at a fixed porosity. They concluded that the thermal performance of body-centered cubic trusses, along with the simple-cubic and Kelvin Octet lattice-cells, was better than some traditional geometries. Yang et al. [35] numerically investigated the heat transfer in BCC lattice under super critical CO_2 environment. It was concluded that several types of vortices were induced in the flow domain, which increased local turbulence intensity and energy transport. These studies also showed that the enhanced heat transfer in such geometries was typically closely followed by an increase in the pressure drop across the cooling channel.

Despite the growing number of studies for AM lattice structure for internal heat transfer applications, there has been a lack of systematic study on the effects of the diameter of the ligament and the orientation of the unit cell with respect to the flow for a given unit cell topology. However, there have been several studies on the effects of these parameters for cylindrical geometries [36–42]. These studies have shown that the flow around such cylinders consists of complex secondary flows and wake shedding behavior. The strength and nature of these flow features, and in turn, the thermal-flow behavior, are intricately dependent on the diameter and the orientation of the cylinders with respect to the bulk flow or crossflow. Typically, the lattice unit cells also comprise of a complex arrangement of cylindrical ligaments akin to cylinders in a crossflow in the above studies. Thus, it is expected that the thermal-flow behavior of lattices will also depend on these geometrical parameters, and a systematic investigation is warranted. This is especially true for single layer lattices where the impact of each ligament becomes more prominent on both the overall averaged as well as the local heat transfer on the end walls. The presented research aims at filling this knowledge gap.

1.1.2 External Cooling

The external cooling of the gas turbine airfoil is primarily done through film cooling holes located on its outer surface. This cooling technology has been extensively studied and implemented for gas turbine cooling applications [43–46]. The film cooling holes are generally fabricated as a post-processing step after the airfoil has been manufactured by using advanced machining such as laser drilling and electro-discharge machining [47–49]. Film cooling works by injecting cooling air from the internal passages into the boundary layer present on the outside of the airfoil. This relatively cooler air forms a protective blanket and prevents the hot external gases from coming in contact with the metal surface of the airfoil. In addition, the local heat flux is also diminished because the film temperature becomes the driving factor for the heat transfer into the airfoil [8,9]. Various design improvements have been suggested in the literature to improve the film cooling effectiveness, such as [50,51]. However, the film cooling holes cannot provide a complete coverage of the external surface, and the cooling has the highest effectiveness only in the vicinity and downstream of the film holes. An alternative to film cooling is the so-called effusion cooling or full coverage film cooling [52–54]. In this architecture, a large part of the external surface is covered with an array of discrete film cooling holes such that the whole surface is protected. In order to pack these holes as closely as possible, the diameter of these holes is made smaller than the typical film cooling holes and can be as small as 0.2 mm [55]. Effusion cooling is mostly used for hot gas path components facing the highest thermal loads, such as the vanes and walls of the combustion chamber. The heat transfer in such geometries is highly conjugate, and the cooling performance for such architecture is defined in terms of overall cooling effectiveness, φ, as

$$\varphi = \frac{T_g - T_w}{T_g - T_c} \quad (1.5)$$

where, T_g is the main gas temperature, T_w is the external wall temperature on the hot side, and T_c is the reference coolant temperature. The next advanced external cooling concept beyond effusion is known as transpiration cooling. Transpiration cooling designs consist of a porous wall and the coolant is leaked into the external boundary layer through pores in this wall, instead of the discrete film cooling holes. Thus, transpiration architecture can provide continuous coolant coverage on the external surface. Moreover, the high internal surface area in the porous wall leads to additional cooling within the wall itself, further reducing the metal temperature and causing very high overall cooling effectiveness. In the past, studies on transpiration cooling have been conducted using porous walls fabricated by sintering metal particles together, such as in [56–58], or by using sintered wire mesh structures, as used in [59,60]. On the other hand, in recent times, AM has been used to fabricate transpiration architectures with tailored openings, made possible due to the micrometer scale printing resolution of laser-based AM processes. Studies such as [61–63] have shown that such AM-based designs exhibit high overall cooling effectiveness (greater than 0.7) and also display mechanical strength comparable to walls with film cooling holes.

For high-performance airfoils, one of the aims of gas turbine cooling research has been to combine together multiple cooling technologies to achieve the desired overall cooling performance. An example of an advanced integrated cooling architecture is the impingement-effusion cooling, where jet impingement provides internal cooling while the external cooling is achieved through full-coverage film holes [64–71]. In such integrated geometries, the overall performance is linked with the flow direction of the coolant and the strength of crossflow in the internal channel, as shown in [72–75]. In a more advanced design, pin fins are also added on the backend to further promote mixing and turbulence in the channel bulk flow and provide additional

heat transfer surface area. Several studies have investigated the effect of geometric parameters and flow configurations for such geometries [76–78] and have highlighted the benefits of such a marriage between the internal and external technologies.

However, virtually none of the studies have investigated the effects of combining lattice-based internal cooling and transpiration-based external cooling together. The present study proposes an integrated lattice-transpiration architecture that leverages the flexibility afforded by AM in fabricating advanced geometries. Lattices present a unique opportunity for such an integrated architecture compared to the pin fins used in the effusion architecture. The lattice geometries exhibit a very high surface-area to footprint-area ratio compared to pin fins. As a result, they have a much lower impact on the external cooling holes compared to the pin fins. In addition, the lattices are known structural elements and have a high strength-to-weight ratio, making them an ideal geometry to strengthen the porous external wall in an integrated configuration. This research proposes four integrated lattice-transpiration architectures and studies their overall cooling performance under conjugate heat transfer tests.

1.2 Topology Optimization

In the case of the internal cooling of airfoils, an enhancement in heat transfer by using advanced cooling features is accompanied by an increase in the pressure drop within the channel. This is especially true for the extended surface type geometries such as pin fins discussed above. The larger surface area, combined with the development of strong secondary flows, and greater flow blockage in the channel, all lead to this increase in the pressure drop. The relative increase in the magnitude of the heat transfer and the friction factor is an important consideration for

optimizing the performance of a cooling design. A method of optimizing the overall performance of heat transfer geometries is through topology optimization (TO) by maximizing or minimizing given objective functions. There are multiple approaches to TO, as summarized in [79], and in recent times, its application has increased multi-folds. This increase in interest is due to two factors: 1) the advent of AM technologies which can reliably fabricate intricate geometries resulting from topology optimization, and 2) access to greater computation power for solving relevant mathematical models for 3-D domains. The focus of topology optimization has mostly been on the optimization of structural problems, while flow problems have been relatively more restricted, specifically with respect to high Reynolds number flow [80]. The current TO methods are iterative in nature and reach the optimal geometry through various intermediate design stages. This presents a big challenge for their application to thermal flow systems due to the need for regenerating meshed domains for each of the intermediate geometries. The governing equations of fluid dynamics are highly nonlinear in nature, and the success of a given CFD model depends on its ability to capture the details of the flow at various length scales. As a result, unlike the meshing of a solid domain, meshing a fluid domain involves careful treatment of the elements near high shear regions where the flow properties could drastically change over a small region. This makes the CFD results very sensitive to the defects in meshes, which is not the case for solid domains, a typical use case for the TO methods. Thus, the automatic generation of meshes is quite challenging for turbulent thermal-flow systems, severely limiting the application of traditional TO approaches. Additionally, the CFD numerical solutions take a relatively long time to converge, which is especially true for transient simulation. Therefore, it is challenging to evaluate multiple intermediate design stages during a conventional TO process. Nevertheless, several research works have been performed to generate optimum channel geometry for convective heat transfer problems

[81,82]. However, the application of TO for complex cooling inernal cooling of gas turbine airfoil using turbulent flow remains scarce.

Alternatively, second law based analysis could provide another pathway to perform optimization of thermal-flow systems. As discussed in Bejan [83], Herwig and Kock [84], Herwig and Schmandt [85], the analysis of entropy generation rates within the flow field can provide a deeper understanding of the mechanism and location of the losses which result in the overall increased pressure drop. These losses taking place within a thermal-fluid system can be estimated based on the irreversibilities present in the system. The second law of thermodynamics provides a way to estimate these losses in terms of entropy generated during the irreversible processes taking place within the system. In general, for a thermal-fluid system, two mechanisms of entropy generation are present at each location within the flow field [83,84,86]. These are 1) entropy generation due to the transfer of heat along finite temperature gradient, and 2) entropy generation due to viscous losses. These studies emphasized that the unique benefit of utilizing entropy-based analysis is the ability to directly compare the relative magnitudes of the heat transfer and viscous loss effects at any point within the flow field.

Herwig and Kock [84] showed that the Reynolds averaged Navier Stokes (RANS) [87] computational fluid dynamics (CFD) simulations of turbulent flows could be used to obtain the entropy generation rates within heat transfer problems during the post processing step. The volumetric rate of entropy generation for a control volume may be written as [86]:

$$\dot{s}'''_{tot} = \dot{s}'''_{h} + \dot{s}'''_{f} \qquad (1.6)$$

where, $\dot{s}'''_{tot}$ stands for total entropy generation rate, $\dot{s}'''_{h}$ represents the entropy generation rate due to heat transfer, and $\dot{s}'''_{f}$ is the entropy generation rate due to viscous losses, all per unit volume.

The total entropy generated, thus, can be obtained by performing a volume integration of the components over the 3D region of interest, as

$$S_h = \iiint \dot{s}_h''' \, dV \tag{1.7}$$

$$S_f = \iiint \dot{s}_f''' \, dV \tag{1.8}$$

$$S_{tot} = S_h + S_f \tag{1.9}$$

Each of the terms mentioned above can be further expanded in terms of flow field variables calculated during a CFD simulation. Also, for a turbulent flow, each terms has both a time mean as well as fluctuating component [84,86], as shown below,

$$\dot{s}_{tot}''' = \left(\dot{s}_{\bar{h}}''' + \dot{s}_{h'}''' \right) + \left(\dot{s}_{\bar{f}}''' + \dot{s}_{f'}''' \right) \tag{1.10}$$

The time mean components in the above equation can be given as,

$$\dot{s}_{\bar{f}}''' = \frac{\mu}{\bar{T}} \left[2 \left\{ \left(\frac{\partial \bar{u}}{\partial x} \right)^2 + \left(\frac{\partial \bar{v}}{\partial y} \right)^2 + \left(\frac{\partial \bar{w}}{\partial z} \right)^2 \right\} + \left(\frac{\partial \bar{u}}{\partial y} + \frac{\partial \bar{v}}{\partial x} \right)^2 + \left(\frac{\partial \bar{u}}{\partial z} + \frac{\partial \bar{w}}{\partial x} \right)^2 + \left(\frac{\partial \bar{v}}{\partial z} + \frac{\partial \bar{w}}{\partial y} \right)^2 \right] \tag{1.11}$$

$$\dot{s}_{\bar{h}}''' = \frac{k}{\bar{T}^2} \left[\left(\frac{\partial \bar{T}}{\partial x} \right)^2 + \left(\frac{\partial \bar{T}}{\partial y} \right)^2 + \left(\frac{\partial \bar{T}}{\partial z} \right)^2 \right] \tag{1.12}$$

where, μ is the dynamic viscosity, u, v, w are the velocity components, x, y, z are the cartesian coordinates, k is the thermal conductivity, and T is the temperature. While these quantities are directly obtained from the CFD results, the fluctuating components of the entropy generation rates have to be modeled, and has been proposed to be [86],

$$\dot{s}_{f'}''' = \frac{\rho \epsilon}{\bar{T}} \tag{1.13}$$

$$\dot{s}_{h'}''' = \frac{\alpha_t}{\alpha} \dot{s}_{\bar{h}}''' \tag{1.14}$$

where the turbulent dissipation, ϵ, is calculated using a k-ϵ turbulence model [87], ρ is the density, and α_t and α are turbulent and molecular thermal diffusivities, respectively. All the above terms can be readily calculated by creating a custom post processing script once the CFD simulation results are available. Using these relations, the relative magnitude of the two types of entropy production rates at any point in the numerical domain can be expressed in terms of Bejan number, Be, defined as [88],

$$Be = \frac{\dot{S}'''_h}{\dot{S}'''_{tot}} \tag{1.15}$$

The minimization of total entropy production within a thermal flow system has been shown to be a viable pathway to achieve performance optimization by several studies for heat transfer enhancement devices [85,88–94]. However, despite the advantages of this approach, entropy-based performance analysis has not been applied for single-layer lattice type heat transfer geometries for gas turbine applications. This research proposes new approach and shows the immense advantage that second law analysis could provide in breaking down the contribution of flow field structures to the aerothermal performance in lattice-type internal cooling geometries. In addition, the research shows that the second law analysis offers a powerful alternative tool for executing TO for heat transfer geometries in turbulent flow. This method presented several advantages: 1) the method can be implemented as a post process script, thus eliminating the need for a custom solver, 2) optimization can be performed on prespecified geometries in a high Reynolds number flow, and 3) it provided a powerful quantitative insight into the best operating point for a given lattice geometry in terms of inlet flow conditions.

1.3 Statement of Research

The overall aim of this research is to propose lattice cooling geometries for gas turbine airfoil applications and fill the gap in the understanding of their aerothermal performance. In addition, second law analysis is introduced to such geometries, and a topology optimization scheme has been proposed. There are four main objectives of the present research work:

1.3.1 Study of Conjugate Aerothermal Performance

Lattice geometries were developed and proposed as an alternative to the traditionally used pin fin geometries for the internal cooling of gas turbine airfoils. The effect of three parameters: 1) unit cell topology, 2) ligament diameter, and 3) orientation with respect to the incoming flow, on the overall heat transfer and pressure drop characteristics were investigated. For this, four different unit cell topologies: body centered (BC), face centered (FC), octahedral (OCTA), and Kagome, were designed. In order to study the effect of the diameter, three cases were prepared for each of the lattices. Two of these cases consisted of unit cells with uniform diameters of 0.5 mm and 0.75 mm, while the third case consisted of unit cells with all vertical ligaments of 0.75 mm and inclined ligaments of 0.5 mm diameter. The orientation with respect to flow for these cases was kept constant at 0°. Similarly, three values of θ were used for each lattice to understand the impact of the orientation on the aerothermal performance while keeping $d = 0.75$ mm. The first two cases consisted of $\theta = 0°$ and 45°, while the third case consisted of an orientation that presented the maximum unit cell projected area for the cubic lattices, and the minimum projected area for the Kagome lattice. Steady state conjugate tests were conducted to obtain the heat transfer and pressure drop values for these geometries using a custom-made test rig. It was shown that these

lattices could be successfully fabricated using DMLS AM process and IN718 superalloy, which are used by the gas turbine OEMs. In addition, two standard pin fin configurations were also fabricated and tested alongside and served as baselines for comparison of the performance of the lattices. These results form the basis of Chapter 2.

1.3.2 Investigation of Local Heat Transfer Coefficient on End Wall

The conjugate heat transfer tests only provided an overall cooling performance of the lattice geometries. However, in order to obtain a complete picture, it was very important to obtain the local heat transfer coefficient, h, on the end wall of the channel. For this, scaled-up lattices were fabricated using SLA AM process and were subjected to transient liquid crystal thermometry. These experiments provided a high-resolution distribution of the local heat transfer coefficient on the channel end wall for a range of Re. The diameter was kept constant while two θ values of 0° and 45° were tested. Once again, a standard pin fin configuration was also tested to serve as a baseline to compare the end wall h and highlight the advantages of lattice geometries. In order to further gain a deeper understanding of the observed h distribution, steady state numerical simulations were performed for each of the tested lattices. The results from these studies have been discussed in Chapter 3.

1.3.3 Propose Novel Integrated Lattice-Transpiration Cooling Architecture

In this part of the research, a novel architecture was proposed that combined the lattice and transpiration cooling designs together. This architecture was created with three objectives in mind. Firstly, this architecture was capable of providing both internal and external cooling

simultaneously, thereby maximizing the overall coolant utilization. Secondly, it reduced the risk of loss of cooling due to blockage of pores in transpiration design by using high heat transfer lattice geometries on the backend. Finally, it alleviated the issues related to mechanical strength in porous transpiration walls because lattices are well-known structural elements. Four integrated lattice-transpiration cooling designs were developed and tested under two different coolant flow conditions. The transpiration design consisted of cylindrical holes with 0.3 mm hole diameter, d, and a 3d pitch. The backend lattice cooling was achieved by using the four lattices developed above with $\theta = 0°$ and a uniform ligament diameter of 0.75 mm. These test coupons were also fabricated using the DMLS AM process and IN718 superalloy. The overall cooling effectiveness was experimentally obtained using steady state infrared thermometry, and the performance was compared against a standard transpiration cooling baseline design. The effect of the blockage on transpiration cooling was also investigated, and the benefit of backend lattices for alleviating these issues was demonstrated. The results from this work have been discussed in Chapter 4.

1.3.4 Propose Second Law Analysis of Lattice Geometries and Perform Topology Optimization

In the final part of the presented research, second law analysis has been introduced to complex lattice geometries, and a scheme of topology optimization using entropy generation rates has been proposed. Within this method, the relative strength of heat transfer and dissipative losses was calculated based on local entropy generation rates and Bejan number (Be). Steady state conjugate numerical simulations were carried out using BC lattice as the base case. A set of criteria was defined to filter out fluid regions and replace them with thermally active solid domain to

suppress form-losses and improve local heat transfer, yielding the optimized topology. The results from this section form the basis for Chapter 5.

2.0 Conjugate Heat Transfer in Additively Manufactured Lattices: Effect of Topology, Diameter, and Orientation

In the research work presented in this chapter, steady state conjugate heat transfer and pressure drop experiments were designed and conducted for four types of lattice geometries. Each of these lattices was developed using a unique unit cell topology, as described in the following sections. These geometries were designed and fabricated to be true-scale, i.e., their size was suitable for application in an actual internal cooling channel of a gas turbine airfoil. The test coupons for this study were fabricated using state-of-the-art DMLS AM process on an EOS M290 [95] system using commercial IN718 superalloy powder. As a result, the effects of fabrication tolerances and, more importantly, that of roughness due to additive manufacturing were preserved. These experiments provided the overall averaged Nusselt number, Nu, and friction factor, f, for the lattice geometries. The effect of the unit cell topology, ligament diameter, and orientation of the lattice on both Nu and f were investigated for a range of channel Re.

2.1 Unit Cell and Lattice Geometries

The lattice geometries developed in this research comprised of unit cells which were designed using cylindrical ligaments. These ligaments were either vertically oriented or inclined, with some of them intersecting at defined points. These intersection points were called nodes and formed an important basis for the nomenclature of the given unit cell. Four types of unit cells were used for this study: 1) body centered (BC), 2) face centered (FC), 3) octahedral (OCTA), and 4)

Kagome. Fig. 2.1 shows the geometric details of these unit cells. The BC, FC and OCTA unit cells consisted of four vertical ligaments, each located along the edge of the unit cell which was parallel to the z-axis, and a number of additional inclined ligaments. In case of BC, the inclined ligaments were present along the body diagonals of the unit cell and intersected at its centroid. These were named as BD. In FC, the inclined ligaments were located along each of the face diagonals present on the yz and zx facets of the unit cell and were referred to as FD. The OCTA unit cells were derived from the FC unit cells by adding short, inclined ligaments, named OD, from each of the four face center nodes to the center of the xy facets. The structure created by these short ligaments resembled an octahedron geometry, hence the given name. These three unit cells were cuboid in shape and resembled the cubic unit cell encountered in naturally occurring crystals. On the other hand, the Kagome unit cell was constructed using three cylindrical ligaments of constant diameter which intersected at a central node. The ends of the ligaments on each side of the node formed an isosceles triangle, with the top and bottom triangles being 60^{o} rotated with respect to each other. This unit cell resembled two pyramids stacked on top of each while sharing a common vertex.

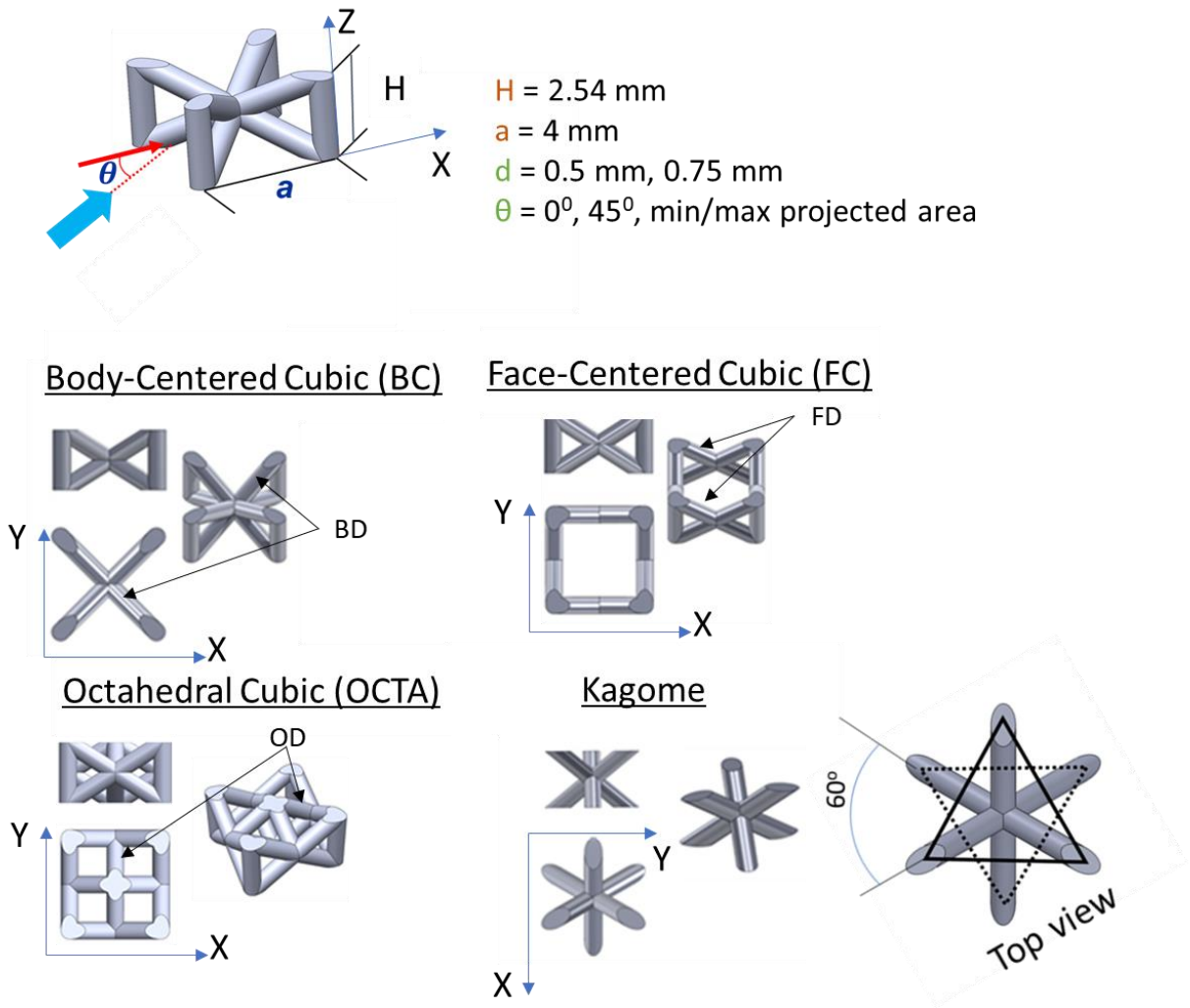

Figure 2.1 Overview of the unit cell geometries and important parameters

There was a range of geometrical parameters associated with each unit cell and the key parameters as listed in the above figure. Apart from these, a parameter θ represented the orientation of the incoming flow w.r.t. the face normal of upstream yz facet of the unit cell. With a change in θ from 0° to 45°, the projected area of the unit cell seen by the incoming flow also changed. An area ratio was defined as

$$A_r = \frac{A_{blocked}}{A_{total}} = \frac{projected\ area\ of\ the\ ligaments}{total\ projected\ area\ of\ the\ unit\ cell\ cuboid} \qquad (2.1)$$

The variation in A_r for all the unit cells having a fixed d = 0.75 mm is shown in Fig. 2.2. With rotation, the A_r in BC, FC, and OCTA unit cells reached a maximum value at 11°, 22.5°, and 16°, respectively. These angles were referred to as $\theta_{max\text{-}close}$ as they represented the maximum projected area, hence, the maximum flow-blockage configuration for the unit cell. On the other hand, for the Kagome unit cell, the projected area already had a maximum value at the 0° orientation, and instead reached a minimum at θ = 30°. This orientation was referred to as $\theta_{max\text{-}open}$.

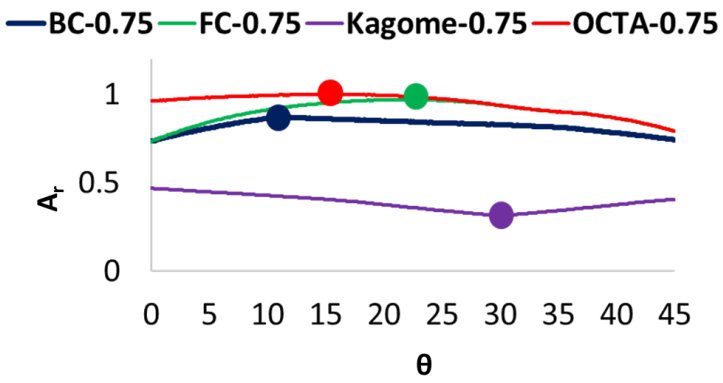

Figure 2.2 Effect of rotation on the projected area of the unit cell

Two sets of designs were generated for each of the unit cells. The first set consisted of unit cells with θ = 0° and uniform ligament diameter, where two values of d were used: 0.5 mm and 0.75 mm. Additionally, unit cells with mixed diameters were also produced for BC, FC, and OCTA by fixing the z-ligaments at d = 0.75 mm and varying the BD, FD, and OD ligaments from 0.5 mm to 0.75 mm. The second set of designs consisted of a fixed uniform ligament diameter of 0.75 mm, and two additional orientations, θ = 45° and $\theta_{max\text{-}close}$, for the cubic unit cells, and $\theta_{max\text{-}open}$ for the Kagome unit cell. The lattices were generated by repeating the corresponding unit cell in an inline array such that each of the z-ligaments was shared between four adjacent unit cells (Fig. 2.3).

Multiple rows and columns were included in order to reduce the impact of the side walls on the overall results. For all the 0° lattices, there were 9 × 9 rows, while for the rotated cases, the total number of rows varied slightly based on the geometry. This was because some of the unit cells had to be made partial in order to adequately accommodate the lattice within the rectangular cooling channel. The diameter and the orientation were indicated in the name of the lattice, as listed in Tables 2.1 and 2.2, to facilitate discussion of the results. In addition to these lattices, two pin fin geometries were also generated in order to serve as a baseline for comparing the aerothermal performance. These pin fin configurations were: (i) PFSD2HD2, with $H/D = S_x/D = S_y/D = 2$, and (ii) PFSD2.5HD2.5, having $H/D = S_x/D = S_y/D = 2.5$, where H is pin height, D is pin diameter, and S is pin to pin spacing in both streamwise and spanwise direction, as shown in Fig. 2.4.

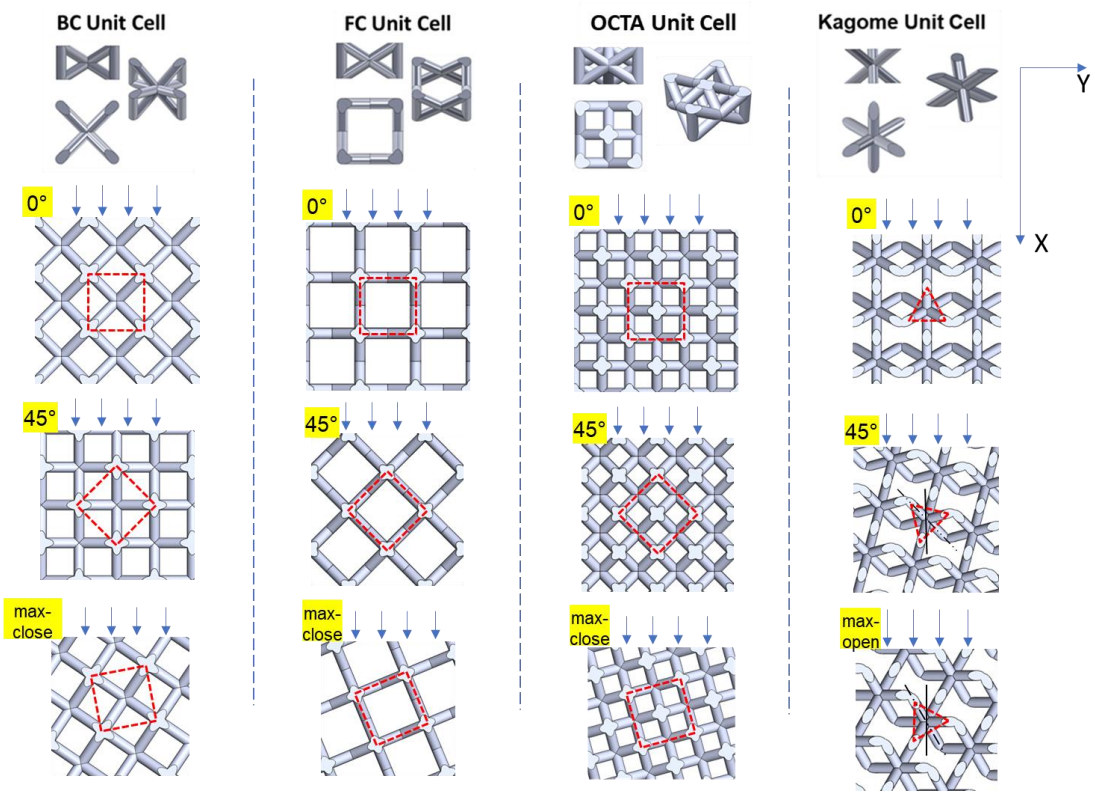

Figure 2.3 Overview of the lattices generated using the four types of unit cells and the three orientations used (shown here for d = 0.75 mm)

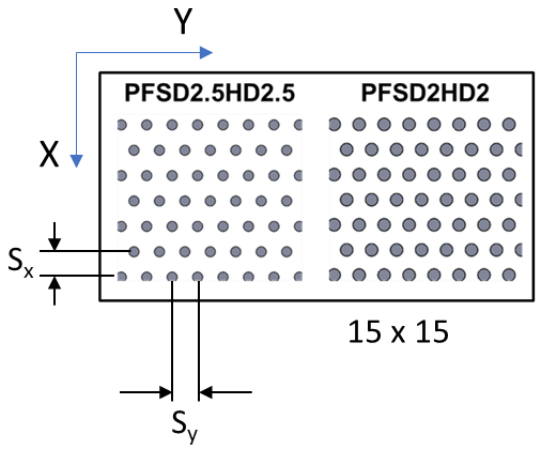

Figure 2.4 The layout of the two baseline pin fins (staggered array of 15 × 15 pins)

The generated lattices and pin fin banks were embedded inside a coupon having a rectangular cooling channel of dimensions H = 2.54 mm, w = 38.1 mm, and l = 38.1 mm (Fig. 2.5). The top and bottom walls of each coupon consisted of holes to insert thermocouples for measuring the temperature at several locations on their mid-plane. The side walls were assumed to be at the same temperature as these walls, so no thermocouples were used there.

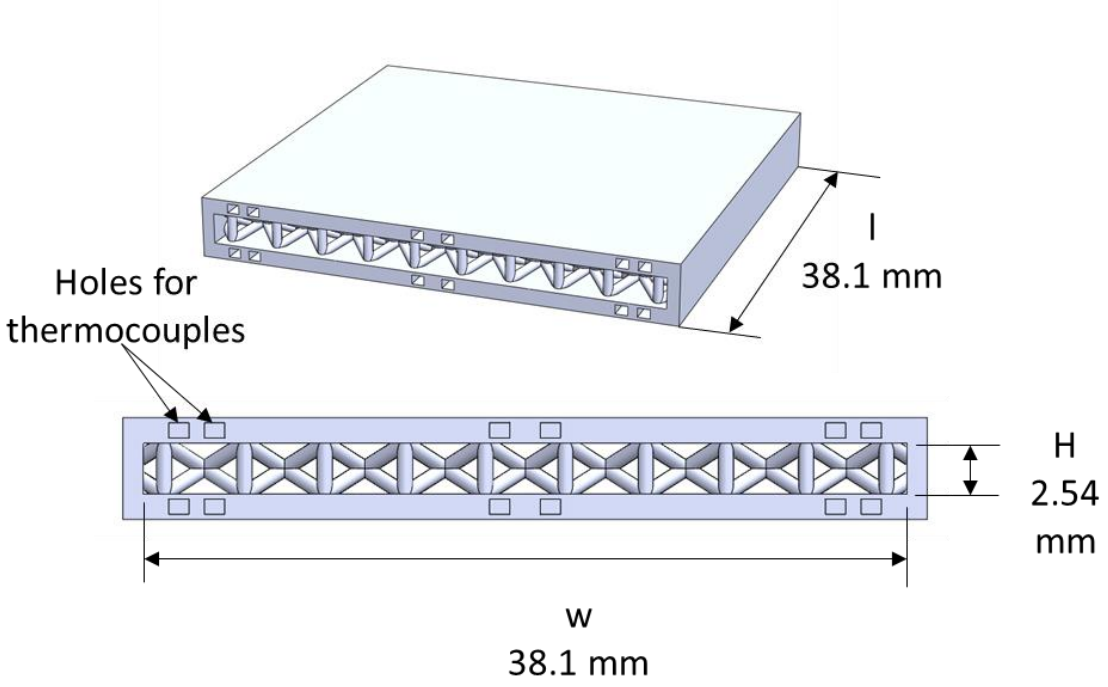

Figure 2.5 Details of the test coupon with embedded lattice geometry (shown for BC0-0.75 lattice)

The main effects of the variation of d were on the overall lattice surface area, $A_{lattice}$, as well as the lattice porosity, ρ, while the relative arrangement of the ligaments remained the same. The porosity was given in terms of the volume of solid, vol_{solid}, and total volume of the smooth channel, vol_{tot}, as,

$$\rho = 1 - \frac{\mathrm{vol}_{\mathrm{solid}}}{\mathrm{vol}_{\mathrm{tot}}} \qquad (2.2)$$

When all other geometric parameters were fixed, the OCTA lattice had the lowest and the Kagome lattice had the highest porosity. On the other hand, the important consequence of the change in θ from 0° to 45° was that the z-ligaments became increasingly staggered compared to an inline pattern at θ = 0°. Similarly, the diagonal ligaments also underwent a significant change in orientation w.r.t. the bulk flow. As a result, the flow field within the cooling channels with

embedded lattice was expected to be significantly affected by unit cell orientation, which emphasized the need to test the effect of θ.

In addition to the above parameters, two area parameters were defined, as shown in following equations, to compare the distribution of heat transfer surface area within test coupon with a given lattice or pin fin geometry. The first one was A_{open} which represented the area of the channel wall that was uncovered by the lattice footprint. Thus,

$$A_{open} = A_0 - A_{footprint} \quad (2.3)$$

where, A_0 = smooth coupon wetted area, and $A_{footprint}$ = area on end walls (including the side walls) occupied by extended surface geometries. Similarly, the total wetted area was given as,

$$A_{wetted} = A_{lattice} + A_{open} \quad (2.4)$$

where, $A_{lattice}$ = area of the extended surface geometries.

As shown in Fig. 2.6., for a similar range of porosities, the lattices showed up to 30% higher wetted area, while the pin fins dominated the footprint area. When comparing the compactness of these geometries, defined as,

$$compactness = \frac{A_{wetted}}{vol_{tot}} \quad (2.5)$$

It was observed that the lattices provide up to 1.6 times higher surface area per unit volume for similar porosity. In addition, the footprint of the unit cells on the end walls also differed with respect to each other, with the greatest coverage for the OCTA geometries, closely followed by Kagome, and then followed by similar coverage for the BC and FC lattices (Fig. 2.6). When compared with pin fins, the lattices provided up to 4.7 times greater surface area to footprint ratio. This parameter was significantly important for the proposed integrated architecture discussed in Chapter 4.

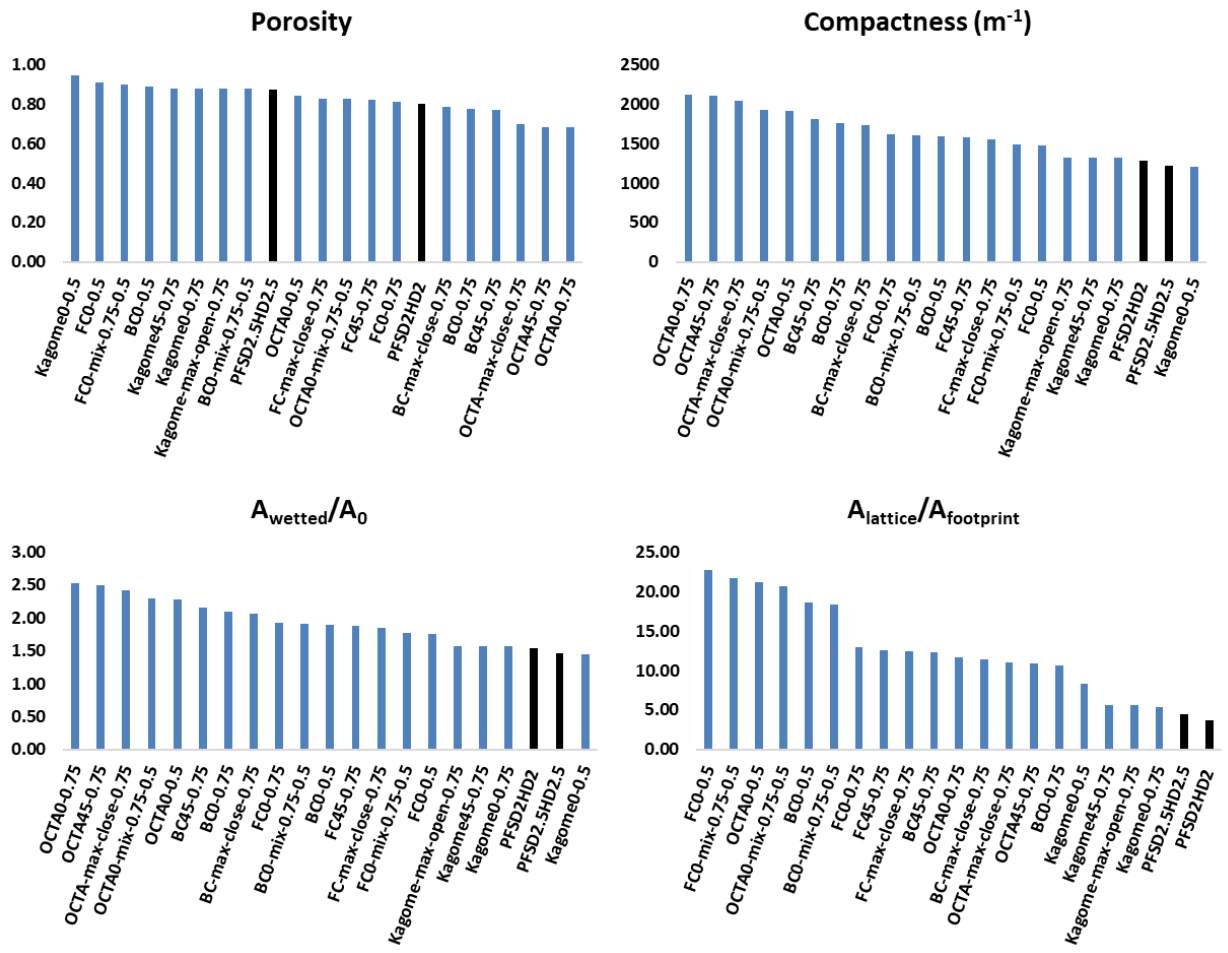

Figure 2.6 Comparison of important geometrical parameters between lattices and baseline pin fins (black bars)

Table 2.1 Geometric details for baseline pin fins

Coupon Name	Channel Dimensions (m)				H/D	S_x/D	S_y/D	Pin Dia. mm	Array		Porosity ρ
	Height H	Width w	Length l	D_{ch}					Rows	Columns	
PFSD2HD2	0.00254	0.03807	0.03810	0.00476	2	2	2	1.27	15	15	0.80
PFSD2.5HD2.5	0.00254	0.03807	0.03810	0.00476	2.5	2.5	2.5	1.02	15	15	0.87

Table 2.2 Geometric details of lattices

Coupon Name	Θ	d (mm)	Porosity	Compactness	A_{wetted}/A_0	$A_{lattice}/A_{footprint}$
BC0-0.5	0°	0.5	0.89	1589	1.89	18.68
BC0-mix-0.75-0.5	0°	0.75, 0.5	0.88	1610	1.92	18.42
BC0-0.75	0°	0.75	0.78	1765	2.10	10.70
BC45-0.75	45°	0.75	0.77	1812	2.16	12.34
BC0-max-close-0.75	11°	0.75	0.79	1730	2.06	11.36
FC0-0.5	0°	0.5	0.91	1473	1.75	22.75
FC0-mix-0.75-0.5	0°	0.75, 0.5	0.90	1485	1.77	21.73
FC0-0.75	0°	0.75	0.81	1621	1.93	12.93
FC45-0.75	45°	0.75	0.82	1580	1.88	12.55
FC-max-close-0.75	22.5°	0.75	0.83	1553	1.85	12.41
OCTA0-0.5	0°	0.5	0.84	1920	2.29	21.20
OCTA0-mix-0.75-0.5	0°	0.75, 0.5	0.83	1933	2.30	20.69
OCTA0-0.75	0°	0.75	0.68	2124	2.53	11.67
OCTA45-0.75	45°	0.75	0.68	2103	2.50	10.85
OCTA-max-close-0.75	16°	0.75	0.70	2040	2.43	11.02
Kagome0-0.5	0°	0.5	0.95	1211	1.44	8.29
Kagome0-0.75	0°	0.75	0.88	1321	1.57	5.41
Kagome45-0.75	45°	0.75	0.88	1325	1.58	5.65
Kagome-max-open-0.75	30°	0.75	0.88	1326	1.58	5.62

2.2 Fabrication of Test Coupons Using DMLS AM Process

The lattice and pin fin test samples were fabricated using IN718 superalloy powder and the DMLS AM process, both being popular among the gas turbine OEMs. DMLS is an additive manufacturing process that fabricates a given part in layer by layer manner with the help of laser [96]. The test coupons were designed using Solidworks [97] computer aided design (CAD) software, were exported as .STL file format, and then sliced into thin layers using a slicing software. Thus, each thin slice represented a cross-section of the actual part to be fabricated. A file containing the details of the slices was processed by the DMLS equipment, EOS M290 [95] located

in the Additive Manufacturing Research Laboratory (AMRL) at the University of Pittsburgh. In this process, a powder bed was initially prepared with the required temperature and an inert environment using argon gas. First, a single layer of powder was deposited on top of the bed with the help of a recoater blade. This was followed by high-speed scan of the top surface of this powder bed using a high-power laser to sinter selected regions in the shape of one of the thin slices of the geometry prepared earlier. A fresh coat of powder was applied, and the process was repeated until the completion of the part. The IN718 superalloy powder was selected as the raw material for the fabrication of the test coupons because it was similar in composition to superalloys that are used in actual gas turbine airfoils and hot gas path components. Fig. 2.7 shows a simplified schematic of the DMLS process and the EOS M290 system used for this work.

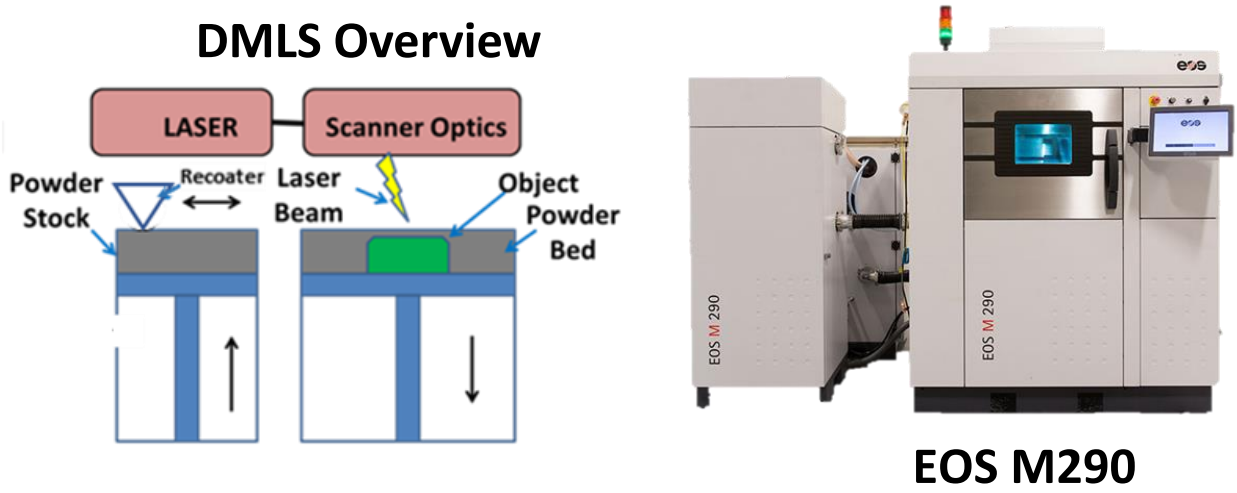

Figure 2.7 Overview of DMLS process and the EOS M290 system used in this research

2.3 Build Quality and Roughness Characterization

For complex geometries, the build quality could be very sensitive to the orientation of the part while printing. This is especially true for lattice-type geometries. The main reason for this sensitivity was the presence of thin ligaments, possible unsupported overhangs, as well as the angle of inclination for these ligaments. The primary concern in deciding the correct build orientation was to minimize the number of unsupported overhangs in the coupons. Fig. 2.8 highlights the impact of build orientation and the ligament diameter on the lattice build quality. Three ligament diameters of 0.5 mm, 0.75 mm, and 1 mm, and two build orientations of 0° and 45° w.r.t. build plate were used for each type of unit cell. The thinner 0.5 mm ligaments were observed to have a higher failure rate and faced quality issues for both build orientations. On the other hand, flat printing had poor quality of the top wall due to large overhangs (~4 mm). When the recoater blade was changed from a stainless steel one to one with carbon brush [98], the quality of the 0.5 mm ligament also greatly improved. Thus, 45^{o} build orientation and a diameter of $d \geq 0.5$ mm for the ligaments were deemed as suitable for printing using the DMLS process. Fig. 2.9 shows the orientation and a batch of printed IN718 coupons still attached to the build plate.

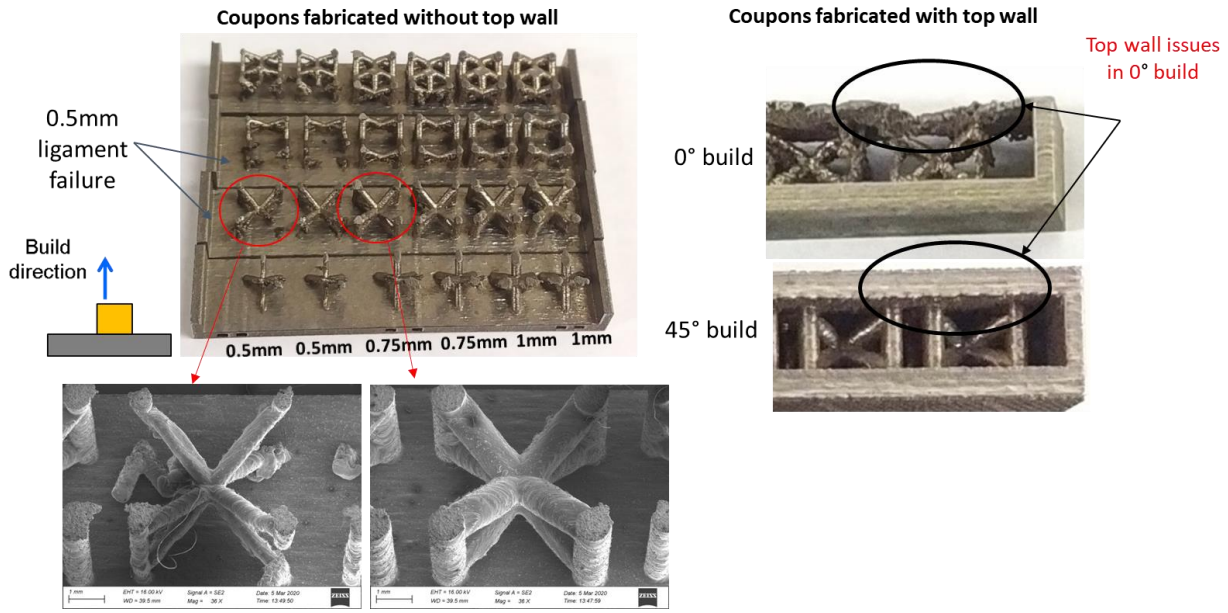

(a)

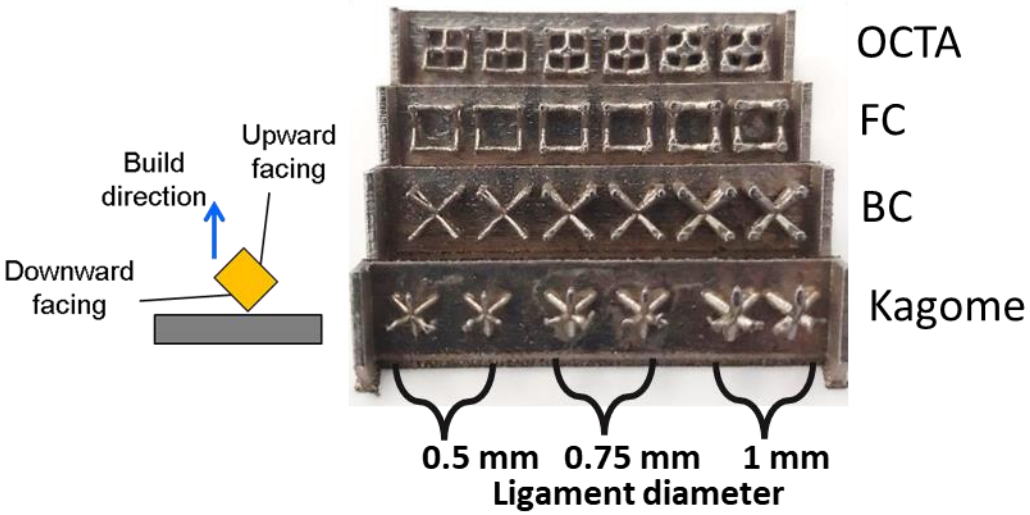

(b)

Figure 2.8 (a) Sample unit cells fabricated to assess the impact of ligament diameter and build orientation on the quality, (b) successful build with 45° tilt and softer recoater blade

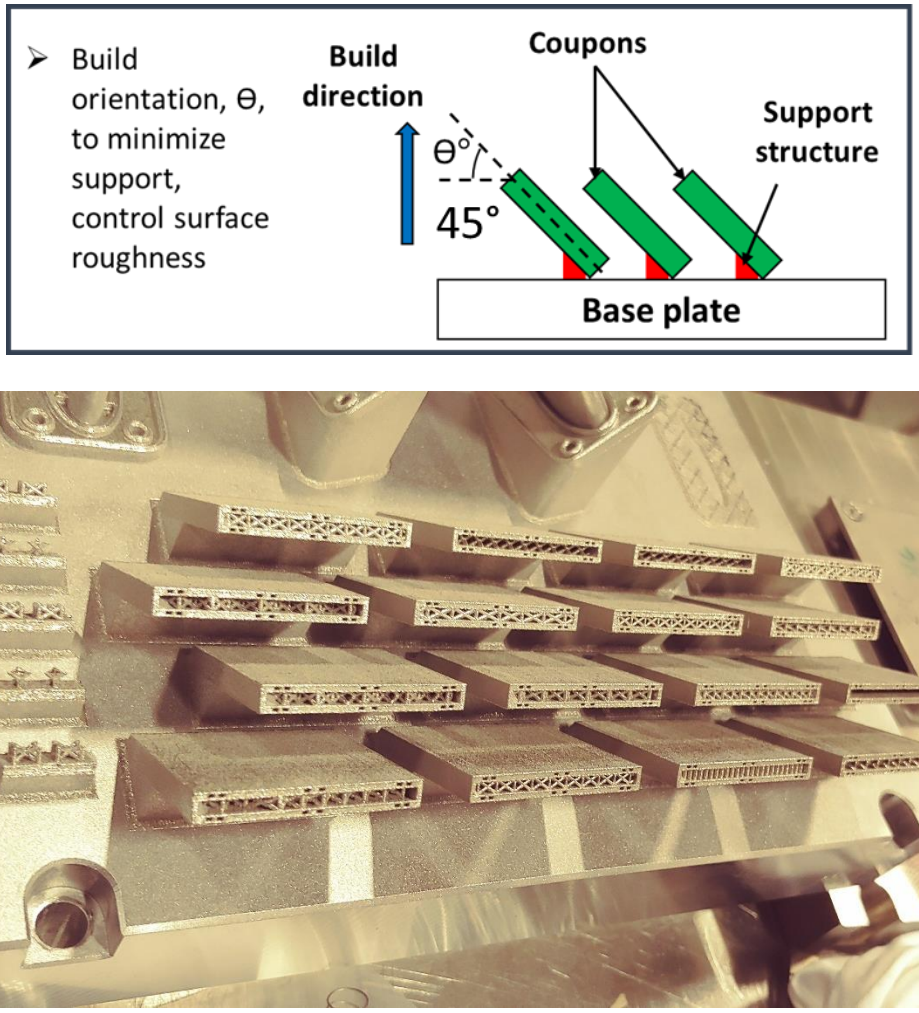

Figure 2.9 (Top) Cartoon depicting the 45° orientation, and (bottom) AM fabricated IN718 coupons on the build plate

One of the characteristic features of parts manufactured using DMLS is the associated surface roughness. The roughness in AM parts mainly arises from the layer by layer fabrication, as well as from satellite powder particles being sintered or melted to the surface [99–102]. A stylus based profilometer, KLA-Tencor Alpha Step IQ Profilometer, was used to characterize roughness of the AM coupons in a way similar to that used in [101]. Two-dimensional linescans of the surface were obtained and further analyzed so that the roughness could be quantified. Fig. 2.10 shows a close-up of a printed surface and sample-section of the measured surface profile. The

measurements were performed at multiple locations, and each measurement was repeated twice. The average roughness, Ra, was calculated for each scanned profile using Eq. 2.6.

$$Ra = \frac{1}{n}\sum_{i=1}^{i=n} |z_i - \mu_{\mathrm{m}}| \qquad (2.6)$$

where, n is the number of samples, z_i is the height of the n^{th} sample, and μ_m is the mean. The Ra and Ra/D_{ch} ratio for the tested coupon is listed in Table 2.3. These values agreed well with those in literature for similar material and print direction [100].

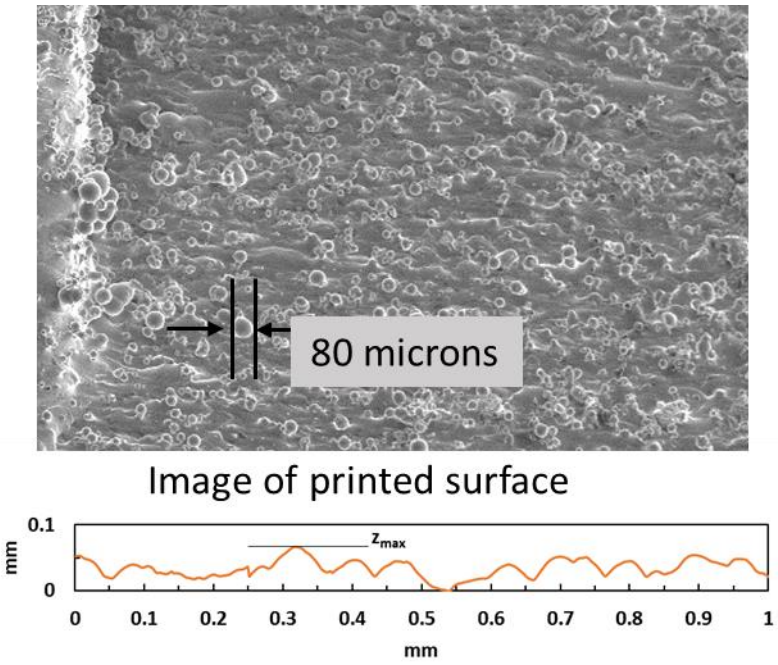

Figure 2.10 Closeup of surface and sample of the measured surface profile for IN718 coupon fabricated using DMLS

Table 2.3 Average roughness (Ra) values on different surfaces of DMLS coupons

Surface	Ra(μm)	Ra/D_{ch}
Upward	11.9	0.0047
Downward	22.2	0.0088
Vertical	12.7	0.005

2.4 Experimental Technique and Methodology

Steady state conjugate heat transfer experiments were conducted to determine the overall heat transfer from the fabricated test coupons. The conjugate tests accounted for heat transfer from both the extended surface geometries in the channel as well as the end walls of the channel. The tests consisted of heating the walls of the test coupons using joule heaters while the cooling air flowed through the channel until a steady state was achieved under well-defined wall heat transfer and flow boundary conditions [103]. For convective heat transfer tests, the average heat transfer coefficient in the channel can be given in terms of Newton's law as,

$$q = hA_{wetted}(T_{wall} - T_r) \quad (2.7)$$

where, h is the overall heat transfer coefficient, q is the heat rate supplied to the wall, T_{wall} is the average wall temperature, and T_r is the reference temperature. In the present tests, the channel walls were heated by a copper block while air flowed inside the channel to provide cooling. This setup can be considered as a parallel-flow heat exchanger with the hot copper block serving as the hot-side fluid and the air serving as the cold-side fluid. Since the copper block was actively heated with a joule heater, the channel wall showed very little temperature gradient along the flow direction, while the air gained heat and its temperature increased between the inlet and outlet. Such

a system resembled a parallel-flow heat exchanger with hot-side fluid having large heat capacity [11,103]. The heat exchange rate in this case is given as,

$$q = UA_{wetted}\frac{\left(T_{w,\,i} - T_{c,i}\right) - \left(T_{w,\ o} - T_{c,o}\right)}{ln\frac{\left(T_{w,\,i} - T_{c,i}\right)}{\left(T_{w,o} - T_{c,o}\right)}} \qquad (2.8)$$

where A_{wetted} = wetted area and U is the overall conductance, $T_{h,i}$ and $T_{h,o}$ refer to the hot wall temperature at inlet and outlet, respectively, while $T_{c,i}$ and $T_{c,o}$ refer to the coolant air temperature at the inlet and outlet, respectively. Comparing this with Eq. 2.7, the temperature difference driving the heat transfer is

$$LMTD = \frac{\left(T_{w,\,i} - T_{c,i}\right) - \left(T_{w,\,o} - T_{c,o}\right)}{ln\frac{\left(T_{w,\,i} - T_{c,i}\right)}{\left(T_{w,o} - T_{c,o}\right)}} \qquad (2.9)$$

and is known as the mean temperature difference (LMTD). Now, in a parallel-flow heat exchanger, the overall conductance on the cold side, U_c, can be written as,

$$\frac{1}{U_c\,A_c} = \frac{1}{h_c A_c} + R_w + \frac{1}{h_h A_h} \qquad (2.10)$$

where, A_c and A_h are the cold side and hot side wetted area, respectively, h_h and h_c are the hot and cold side heat transfer coefficient, respectively, and R_w is the thermal resistance of the wall separating hot and cold flow. However, in the present test configuration, the hot side temperature was represented by the temperature of the wall surface directly in contact with the coolant air. Thus, the conductance and overall heat transfer rate becomes

$$\frac{1}{U_c\,A_c} = \frac{1}{h_c A_c} \qquad (2.11)$$

Therefore,

$$q = \mathrm{h_c A_c} \frac{\left(T_{w,\,i} - T_{c,i}\right) - \left(T_{w,\,o} - T_{c,o}\right)}{ln \frac{\left(T_{w,\,i} - T_{c,\mathrm{i}}\right)}{\left(T_{w,o} - T_{c,\mathrm{o}}\right)}} \quad (2.12)$$

$$= hA_{wetted} \frac{\left(T_{w,\,i} - T_{c,\mathrm{i}}\right) - \left(T_{w,\,o} - T_{c,\mathrm{o}}\right)}{ln \frac{\left(T_{w,\,i} - T_{c,\mathrm{i}}\right)}{\left(T_{w,o} - T_{c,\mathrm{o}}\right)}} \quad (2.13)$$

This formulation can be used to obtain h for cooling channels with a temperature gradient within the channel wall. The input heat flux, $q"$, was obtained from the voltage, V, and current, I, used for the joule heater and the total wetted area of the coupon by using Eq. 2.14

$$q" = V.\frac{I}{A_{wetted}} \quad (2.14)$$

Since perfect insulation is unachievable, the conduction losses, $q"_{loss}$, from the test setup must be estimated to correct the heat added to the air. Such losses were estimated using 1-D thermal resistance network analysis [11]. The overall average h and the corresponding average Nu could then be calculated using Eq. 2.15 and 2.16, respectively.

$$h = \frac{q" - q"_{loss}}{LMTD} \quad (2.15)$$

$$Nu = \frac{hD_{ch}}{k} \quad (2.16)$$

The Re was calculated using the coolant density, ρ_c, and velocity, U_{mean}, channel hydraulic diameter, D_h, and dynamic viscosity, μ, as,

$$Re = \frac{\rho_c U_{mean} D_{ch}}{\mu} \quad (2.17)$$

$$D_{ch} = \frac{4Hw}{2(H + w)} \quad (2.18)$$

The Gnielinski correlation for smooth channels was used to obtain the reference values to compare and assess the augmentation in the heat transfer of the tested coupons. This correlation is given as [104],

$$Nu_0 = \frac{\frac{f_0}{8}(Re - 1000)Pr}{1 + 12.7\left(\frac{f_0}{8}\right)^{\frac{1}{2}}\left(Pr^{\frac{2}{3}} - 1\right)} \quad (2.19)$$

The pressure loss for each test was obtained by measuring the static pressure in the plenum using a handheld manometer. The comparison between the pressure drops of each geometry was then done by calculating the Darcy friction factor [103], f, given by

$$f = \frac{\left(\frac{\Delta p}{\Delta x}\right) D_{ch}}{\frac{\rho U_{mean}^2}{2}} \quad (2.20)$$

This friction factor was then compared with Petukhov correlation [104] which provided friction factor for smooth channel, denoted as f_o.

$$f_o = (0.790 \ln Re - 1.64)^{-2} \quad 3000 \leq Re \leq 5\,x10^6 \quad (2.21)$$

For all the calculations, the air properties were considered based on the mean inlet and outlet temperatures. The uncertainties for these tests were evaluated based on the method proposed by Kline and McClintock [105]. These included uncertainties associated with the measurements in temperature, flow rate, and pressure drop. In LMTD, the uncertainty ranged from 3%-11% resulting in 5%-10% uncertainty in the evaluation of Nu. The uncertainty in the mass flow rate measurement led to 5%-10% uncertainty in the evaluation of Re. Similarly, there was 2%-8% uncertainty in the measurement of the pressure.

The test rig consisted of cylindrical copper block which had a rectangular slot to house the test coupon [101]. A direct current powered strip heater was attached on the outer surface of this copper block to provide the necessary heating, followed by a layer of high-density insulating foam.

The sub-assembly prepared in this way was secured between two C-clamps fabricated using polyvinyl chloride (PVC). Finally, this C-clamp subassembly was sandwiched between a pair of PVC flanges which contained the inlet and outlet pipes. These pipes housed a flow transition units which were necessary for smooth flow transition between the round pipes and rectangular inlet and outlet at the coupons. Fig. 2.11 shows an assembled test rig and its cross-sectional details. A simplified schematic of the complete experimental setup is also shown in Fig. 2.11. Compressed air from an in-house supply line served as the coolant. Several K-type thermocouples were connected to the test section to monitor and record temperatures of the inlet and outlet air, copper blocks, walls of the AM coupon, surface of strip heater, and the heater-foam and foam-PVC interfaces. These thermocouples were interfaced with a National Instruments data acquisition system [106] connected to a desktop computer for real time monitoring and recording. The pressure drop in the test coupon was obtained using handheld digital differential manometer that was connected at the inlet and outlet of the test section.

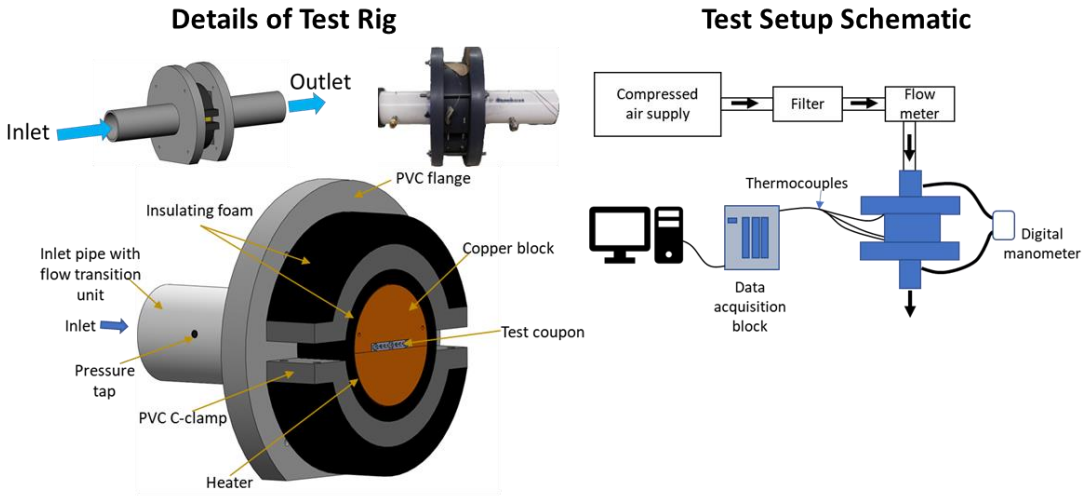

Figure 2.11 Details of the test rig and the schematic of the test facility established for this research. (Left) cross-sectional view of the assembled test rig and external view of the rig, and (right) schematic of the test facility.

At the beginning of the test, cooling air was allowed to flow through the test rig at a set flow rate that resulted in the desired channel Re. The heaters were then switched on with a set power and the setup was left to reach a steady state. Once a steady state was achieved, readings for the temperature and pressure were recorded and the above procedure was repeated for each different Re.

2.5 Results and Discussions

2.5.1 Effect of AM Roughness on Heat Transfer

In order to establish a baseline and to validate the test rig, a smooth coupon was subjected to a steady state heat transfer test. Fig. 2.12 (a) shows the heat transfer enhancement for the coupon as compared with Gnielinski correlation for smooth channels. Even in the absence of any cooling geometry, the coupon showed ~1.7 times higher heat transfer than a standard smooth channel. This heat transfer enhancement can be attributed to the roughness present on the coupon walls due to the AM process. A correlation for AM coupons, as proposed by Stimpson et al. [100], was used to further validate this result. The correlation is given as

$$Nu = \frac{\left(Re^{0.5} - 29\right) Pr \sqrt{\frac{f}{8}}}{0.6\left(1 - Pr^{\frac{2}{3}}\right)} \qquad (2.22)$$

Fig. 2.12 (b) compares the Nu predicted using Eq. 2.22 and the Nu obtained through experiments for the DMLS smooth channel coupons. Most of the data agreed very well with the prediction from the correlation, with $\pm$12% variation for the worst cases.

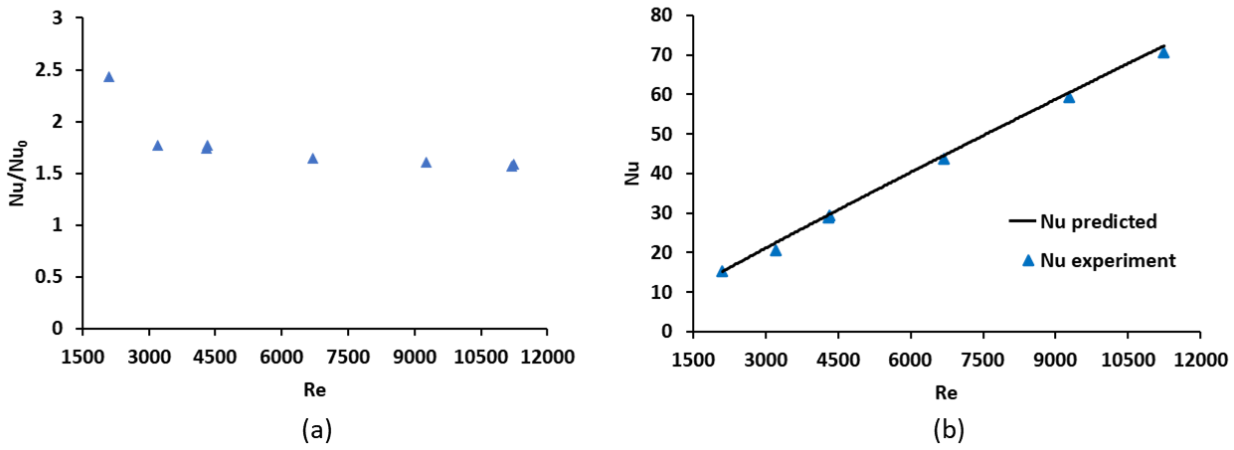

Figure 2.12 (a) Nu augmentation in DMLS fabricated smooth channels, and (b) validation of experiment based on correlation from [100]

2.5.2 Heat Transfer in Lattice Geometries

The heat transfer within the lattice geometries was characterized in terms of dimensionless Nu, as discussed above. This Nu represented the overall averaged heat transfer rate from the coupons. The effect of the variation in diameter on the overall averaged Nu for the tested lattices is shown in Fig. 2.13. The Nu increased with an increase in the ligament diameter, as well as with an increase in the Re. The increase in the diameter was performed in two steps. In the first step, only the ligaments located along the z-axis, i.e., the z-ligaments, were increased from 0.5 mm to 0.75 mm. In the second step, the diameter of the remaining ligaments was also increased from 0.5 mm to 0.75 mm. This increase in d was accompanied with a corresponding increase in the A_{wetted}. as shown in Fig. 2.6 (based on the CAD files).

On an average, the Nu increased by 5%-6% from BC0-0.5 to BC0-mix-0.75-0.5, and by 7% - 15% from BC0-mix-0.75-0.5 to BC0-0.75. In case of FC lattices, Nu remained virtually the

same between FC0-0.5 and FC0-mix-0.75-0.5, while on moving from FC0-mix-0.75-0.5 to FC0-0.75, the Nu further increased by 17% - 20%. Similarly, for the OCTA lattices, the Nu increased by approx. 4% to 8% from OCTA0-0.5 to OCTA0-mix-0.75-0.5, by approx. 22 % to 24% from OCTA0-mix-0.75-0.5 and OCTA0-0.75. In case of the Kagome, the Nu increased by 16% to 20% from Kagome0-0.5 to Kagome0-0.75. This trend was similar to that observed in A_{wetted} which also increased with an increase in the diameter. However, in general, the change in Nu was much larger than the change in the A_{wetted}. Thicker ligaments led to a stronger wake shedding and secondary flows which promoted greater bulk mixing. In addition, ligaments with larger diameter offered lower thermal resistance and thus, had greater fin efficiency. These factors together led to the observed increase in Nu with d.

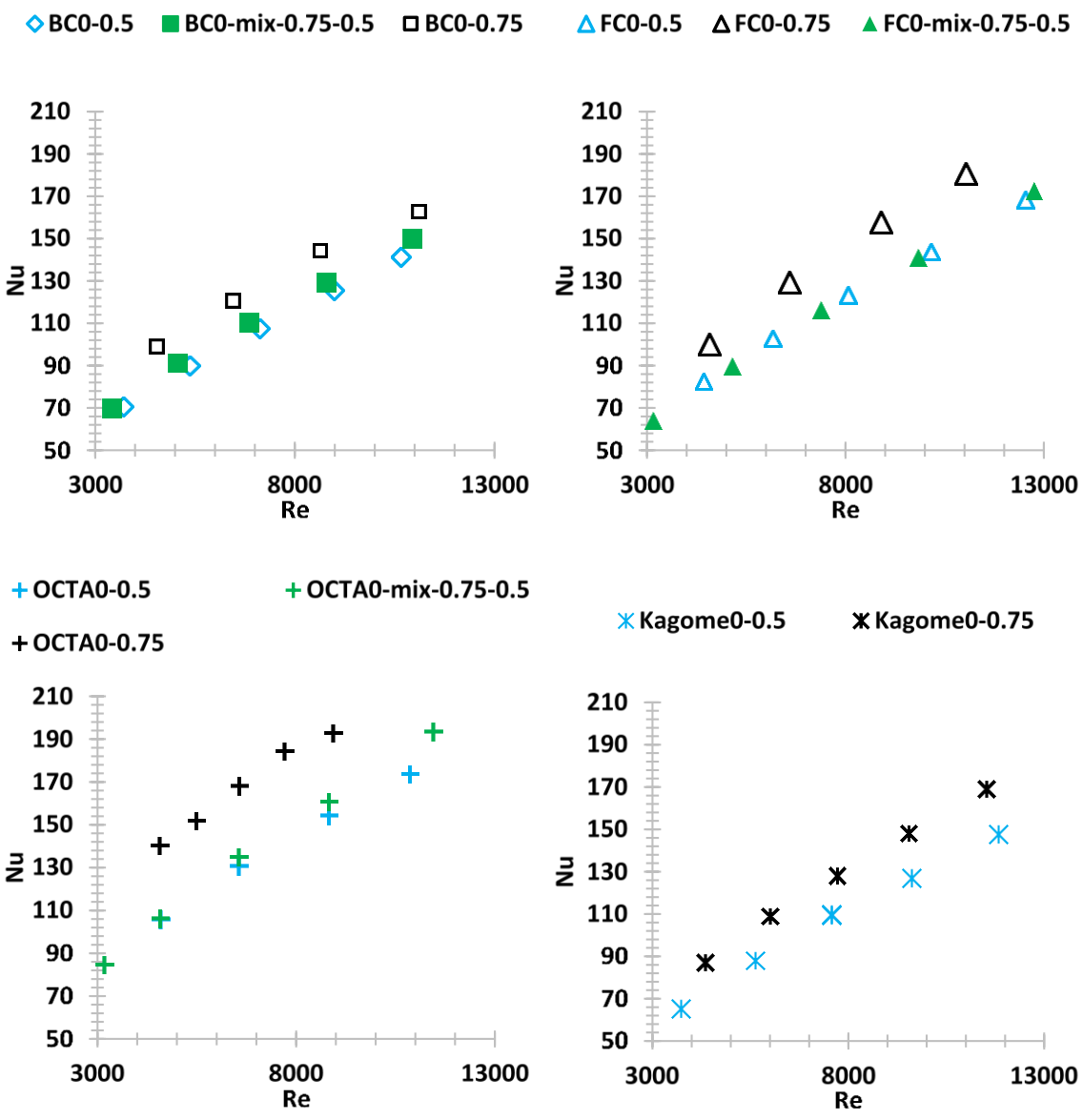

Figure 2.13 Effect of the diameter on Nu for the tested lattice geometries

The impact of θ on the heat transfer was more complex compared to that of d. In case of both BC and FC lattices, the Nu increased when θ changed from 0° to 45°. The change was greater in case of FC (15%-24%) compared to BC (6%-14%). When θ was changed from 0° to the max-close orientation, the FC lattice once again showed a greater improvement in Nu by 17%-19%

while there was 6%-14% gain in Nu of BC lattice. The FC-max-close-0.75 and FC45-0.75 performed very close to each other, while BC-max-close-0.75 showed an improvement of 7%-8% over BC45-0.75. In contrast to the BC and FC lattices, the Nu in OCTA lattice decreased by up to 10% when θ changed from 0° to 45°. On the other hand, when θ was changed from 0° to 16° (max-close orientation), a 3% increase in Nu was observed. In case of the Kagome lattice, on changing θ from 0° to 45°, *Nu* increased by up to 8% at higher Re, and by 6% - 13% from Kagome0-0.75 to Kagome-max-open-0.75.

One of the major effects of rotation on the BC, FC, and OCTA lattices was that the relative arrangement of the ligaments changed greatly with respect to the incoming flow. For example, the z-ligaments became staggered with respect to the bulk coolant flow direction when lattices rotated from 0° to 45°. As a result, the openings available within the lattices for the coolant to flow through also varied. In addition, the secondary flow generated by the inclined ligaments was also greatly modified due to the changed orientations, as has been observed in case of inclined cylindrical geometries under crossflow in [14].

Fig. 2.14 compares the Nu for all the tested geometries, including the two baseline pin fin banks. An important observation from these results was that the pin fin baselines provided a very comparable heat transfer enhancement to that of the lattices. The PFSD2HD2 showed an increase in heat transfer very close to the FC45-0.75. The pin fin baselines were staggered in nature, and thus, the downstream pins were located outside of the wakes from the upstream pins, therefore increasing the pin surface exposed to the coolant. This helped the pin fins achieve a high heat transfer rate. In case of the lattices, as mentioned before, the rotation did cause the vertical ligaments to move from an inline to a staggered configuration, however, due to the presence of additional inclined ligaments within the unit cells, the flow was diverted in a much more complex

flow pattern than in case of the pin fins. Overall, OCTA lattices depicted the highest heat transfer, while the Kagome lattices showed the lowest heat transfer.

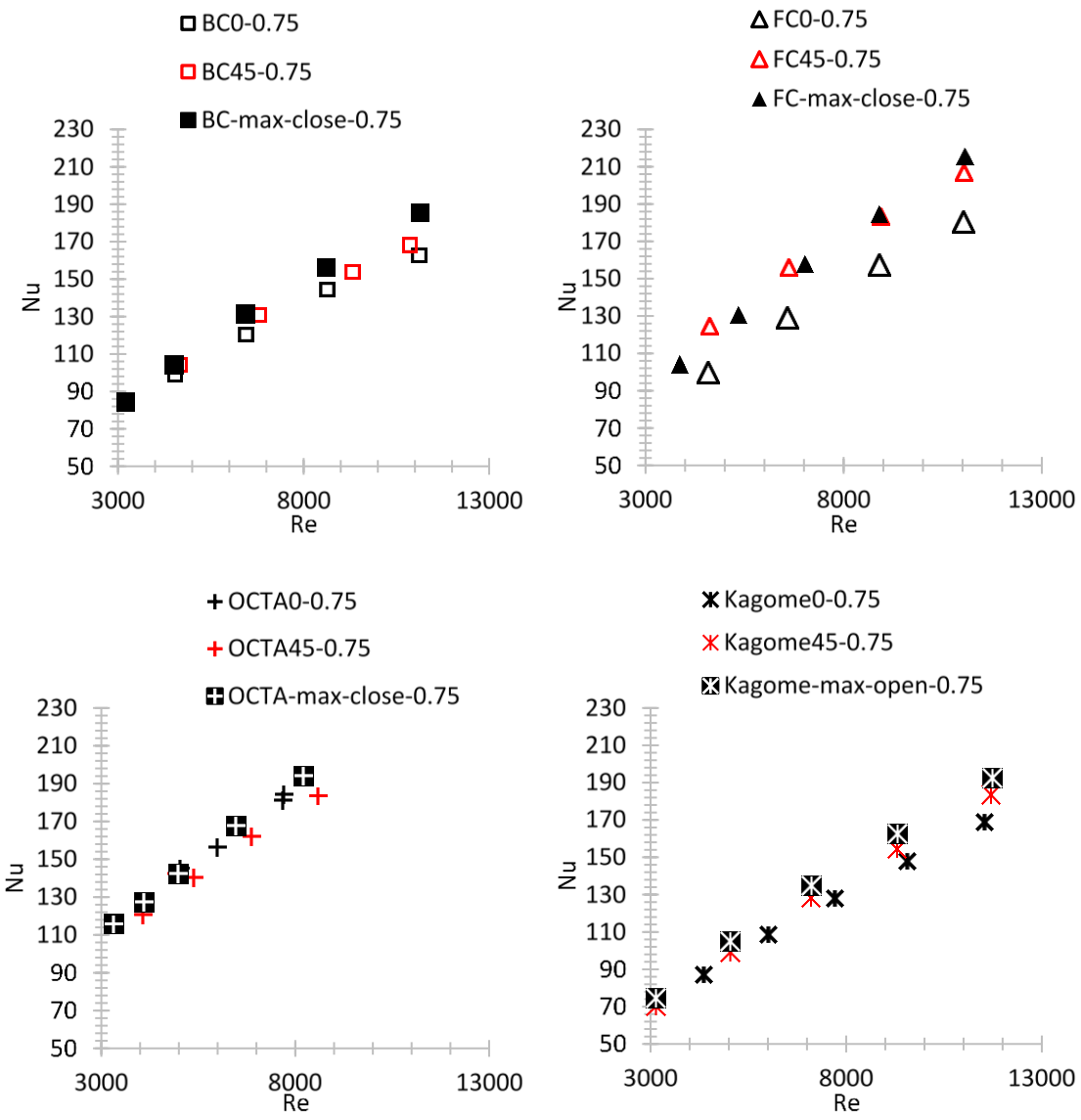

Figure 2.14 Effect of the orientation on Nu for the four lattice geometries

2.5.3 Pressure Drop in Lattice Geometries

The pressure drop is reported in terms of the friction factor that was defined based on the channel Re at inlet flow conditions. The results are discussed in terms of the variation in the diameter, followed by the variation in the orientation, similar to the heat transfer results. Fig. 2.15 show a comparison between f against Re for the lattices with 0° orientation and varying d. In all cases, the pressure drop first increased until Re of ~6000 – 7000, and then decreased, indicating that the flow had become fully turbulent. When d was increased from 0.5 mm to 0.75 mm, there was an increase in the value of f for all the tested lattice geometries. The extent of this increase was highly dependent on the lattice geometry, as discussed further.

The average value of f first increased by 22% from BC0-0.5 to BC0-mix-0.75-0.5, and then by ~80% when d became 0.75 mm in BC0-0.75 lattice. In case of the FC lattices, the average f value first increased by ~11.4% from FC0-0.5 to FC0-mix-0.75-0.5. On further change of diameter to 0.75 mm, average f became ~46.6% higher than FC0-mix-0.75-0.5 lattice. Thus, among the BC and FC lattices, the BC lattice showed a greater increase in pressure drop when moving from the lower to higher diameter values. For OCTA0 lattices, the average f for OCTA0-0.5 and OCTA0-mix-0.75-0.5 were very close with a value of ~10.3 and ~10.11, respectively. On the other hand, OCTA0-0.75 had a very high pressure drop with an average f of 23.29, which was ~2.3 times higher than the other two configurations. Finally, for the Kagome lattices, an increase in d from 0.5 to 0.75 resulted in a corresponding increase in f from ~1.37 to ~2.58, an ~88.3% increase.

Overall, the increase in the f values with an increase in the diameter could be attributed to the increase in the surface area, larger wakes structures behind the thicker ligaments, and the increase in the flow blockage due to decreased porosity.

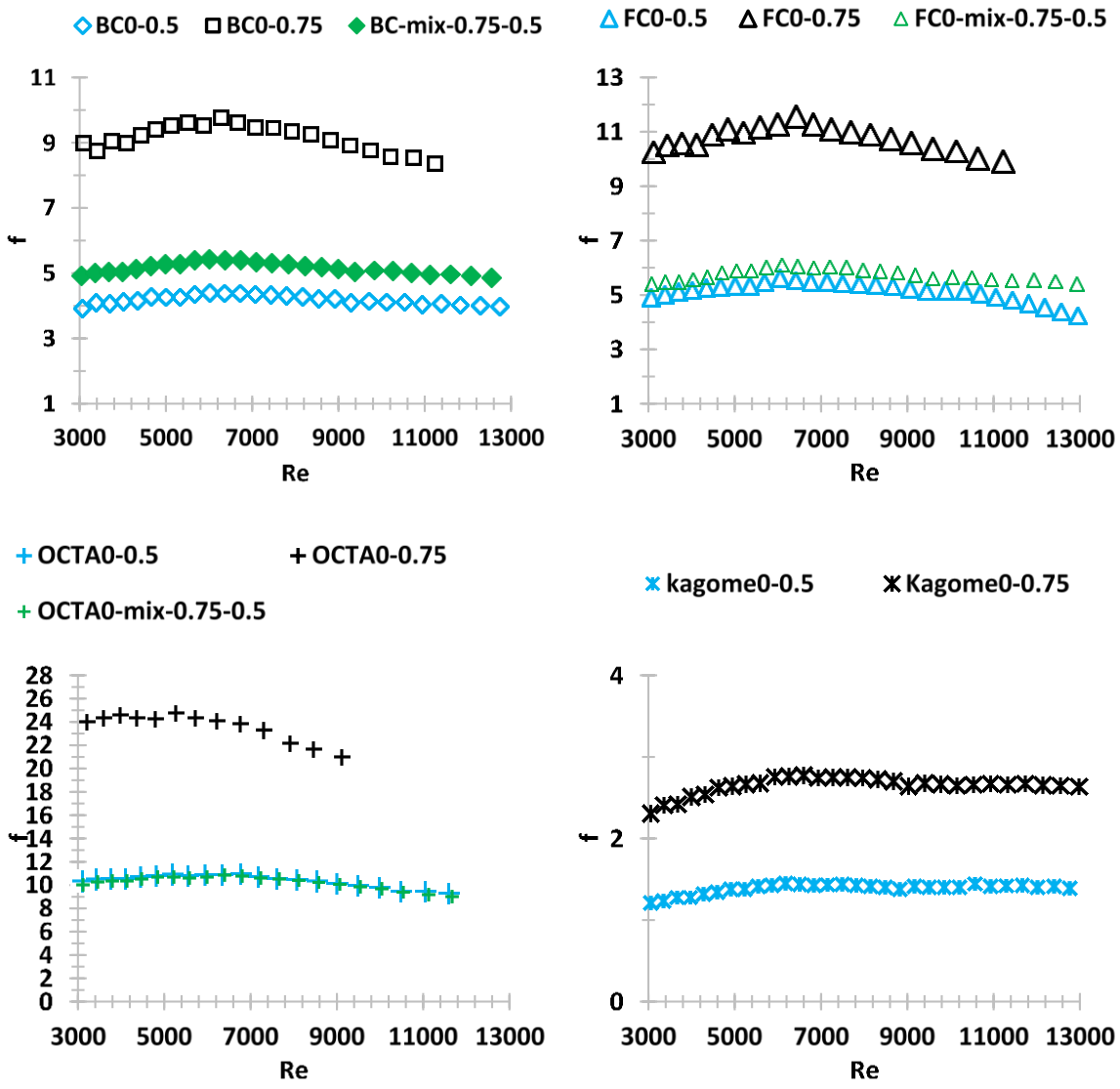

Figure 2.15 Effect of the diameter on f for the four lattice geometries

The effect of θ on the pressure drop was somewhat different than the trend observed in the case of heat transfer (Fig. 2.16). In case of the BC lattices, the average f increased from ~9.03 for BC0-0.75 to ~13.08 for BC45-0.75, and then reduced back to ~9.35 for BC-max-close-0.75. Thus, the rotation to 45° caused a 44.9% increase in the pressure drop, while the maximum blockage

orientation resulted in basically no change in the pressure drop. This highlighted the fact that when the porosities are similar, the orientation plays an important role in deciding the overall pressure drop and heat transfer performance.

Another interesting trend was observed for the FC lattices where the change in orientation did not result in any significant change in the pressure drop. On the other hand, a rotation of 45° in OCTA lattice led to a decrease in the average f from 23.29 to 20.08, ~14% change, while the pressure drop changed very little for the OCTA-max-close-0.75. Finally, in case of the Kagome lattices, the f increased from 2.58 to 3.01 for Kagome45-0.75, and slightly increased further to 3.18 for Kagome-max-open-0.75. Interestingly, the orientation corresponding to maximum-open unit cell area resulted in the highest pressure drop, while the 0° orientation, which was the maximum-close orientation, resulted in the lowest.

In case of the baseline pin fins, the pressure drop values were higher than the Kagome lattices while lower than the other cubic lattices. The pin fins showed a lower pressure drop even for the higher porosity values. The flow filed within the lattices was significantly more complex than that in the pin fins because of the way the open flow area was distributed in the channel, causing the coolant to flow in a complex path. In addition, the inclined ligaments led to stronger secondary flows and the wetted area was higher than the pin fins, both factors adding to the pressure loss in lattices.

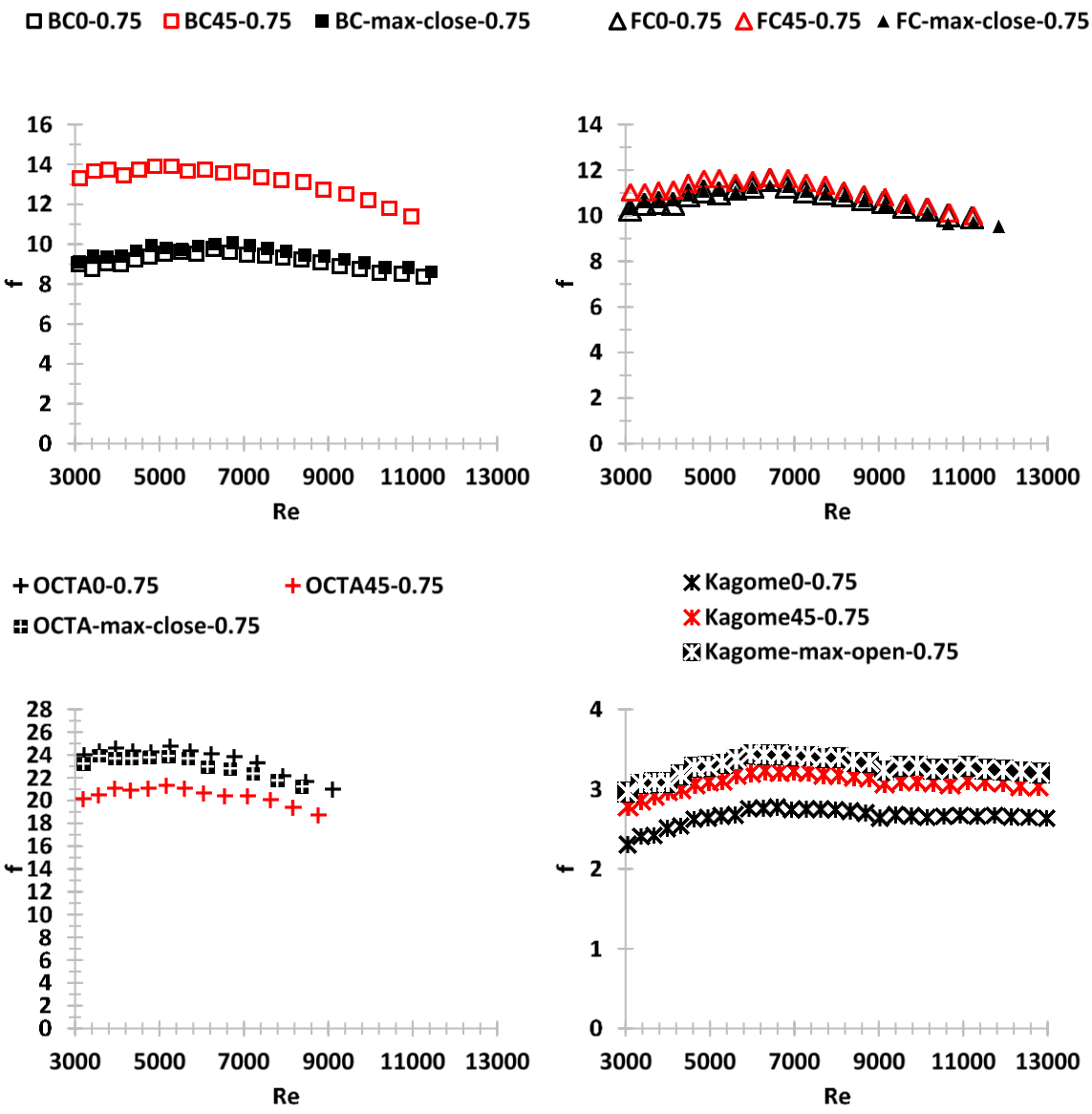

Figure 2.16 Effect of the orientation on f for the four lattice geometries

2.5.4 Augmentation in Heat Transfer and Pressure Drop

Fig. 2.17 and Fig. 2.18 compare the augmentation in Nu and f values, respectively, compared to that of a smooth channel for all the tested geometries. In general, for a given ligament

diameter, the heat transfer followed the trend OCTA > FC > BC > Kagome. Thus, OCTA showed the highest Nu augmentation of > 7 times that of the smooth channel for OCTA0-0.75 and OCTA-max-close-0.75 at higher Re. This was followed by the OCTA45-075, FC45-0.75, and FC-max-close-0.75 lattices showing > 6 times better heat transfer than the smooth channel. Thus, these were the highest heat transfer lattice configurations in the tested range of d, θ, and Re. For the remaining lattices with d = 0.75 mm, $5 < Nu/Nu_0 < 5.7$ for the highest tested Re values. The lowest heat transfer was shown by the lattices with d = 0.5 mm, especially Kagome0-0.5, however, the Nu/Nu_0 was still > 4 times.

The augmentation in the heat transfer was followed by an increase in the friction factor for the lattice geometries. The trend in f/f_0 has been shown in Fig. 2.18, and was somewhat similar to that observed in Nu/Nu_0. For d = 0.75 mm, OCTA lattices showed the greatest increase in f, with OCTA0-0.75 reaching greater than 640 times the smooth channel value at higher Re. The BC and FC lattices formed the second highest group with f/f_0 ranging between 200 – 400, followed by the pin fins and Kagome lattices with f/f_0 under 150. Thus, three groups could be defined in terms of the pressure loss. These were: the high-loss group containing OCTA lattices, followed by intermediate-loss group consisting of FC and BC lattices, and finally, the low-loss group comprising of pin fins and Kagome lattices. A similar trend existed among the lattices with thinner and mixed diameters.

The performance of the baseline pin fin PFSD2HD2 matched closely to that of FC-max-close-0.75 and FC45-0.75, showing up to 6.7 times augmentation in heat transfer. Similarly, the second pin fin PFSD2.5HD2.5 also performed better than most of the lattice configurations, with a $Nu/Nu_0 > 6.7$ in the tested Re range. Most of the tested lattices had a much better compactness

and wetted surface area than the baseline pin fins, which indicated towards a better heat transfer performance in lattices. However, the observed relatively higher heat transfer in pin fins could be explained in terms of fin efficiency.

Each of the ligament can be assumed to be a straight cylinder with constant heat transfer coefficient, h, diameter, d, and thermal conductivity, k, protruding into the coolant crossflow. If h was assumed to be uniformly distributed over the surface of the cylinder, Figures 2.19 and 2.20 show the results for the efficiency and effectiveness, respectively, for both z and diagonal ligaments of some of the tested lattices. The ligaments in lattices had at least 25% higher ϵ_{fin} compared to pin fins, due to their slender geometry. On the other hand, the η_{fin} showed two trends. The z-ligaments matched the pin fins very closely, while the diagonal ligaments showed varying degree of decreases η_{fin}. This was due to the low thermal conductivity of the IN718 superalloy, which meant that the slender ligaments presented larger thermal resistance and higher temperature gradient along their length. This reduced the overall heat transfer from these elements. An important conclusion from these results is that the performance of the lattice geometries could be further pushed by increasing the conductivity of the fabrication material.

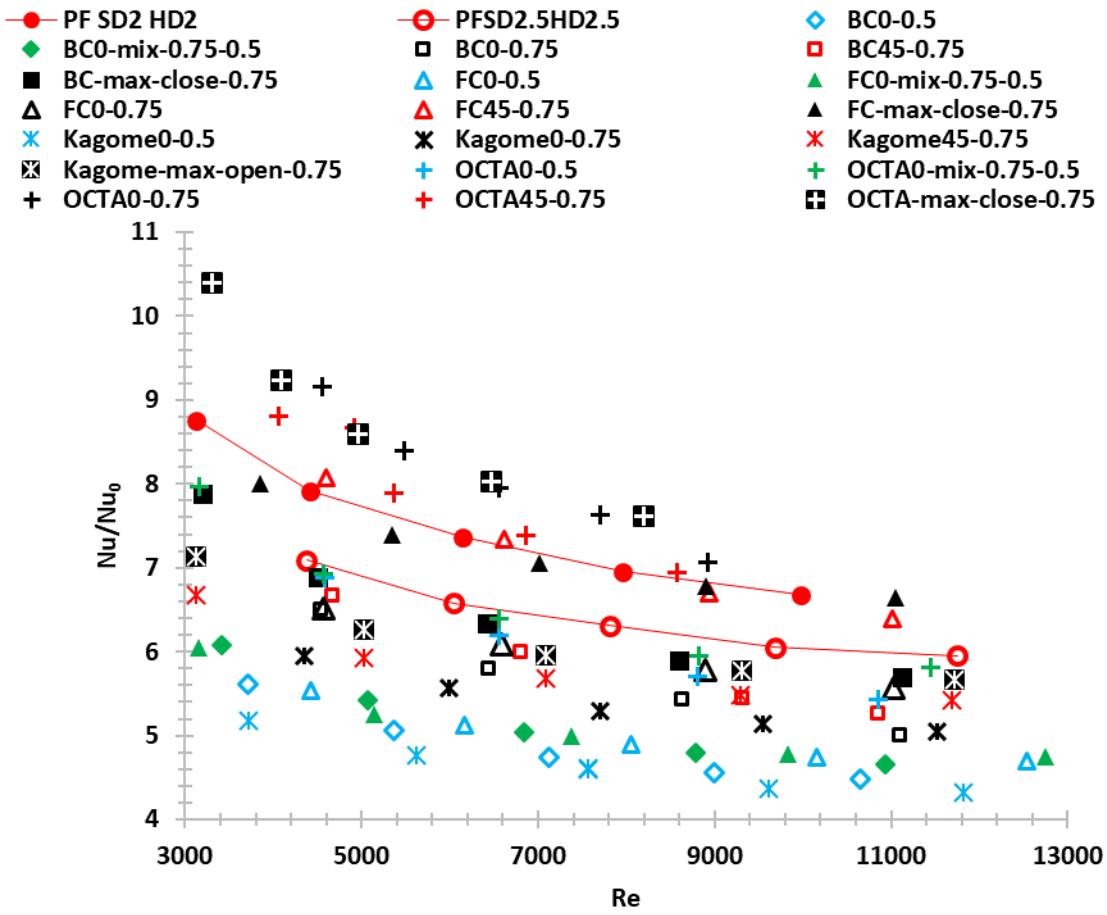

Figure 2.17 Augmentation in Nu for the tested lattices and baseline pin fins compared to the smooth channel correlation

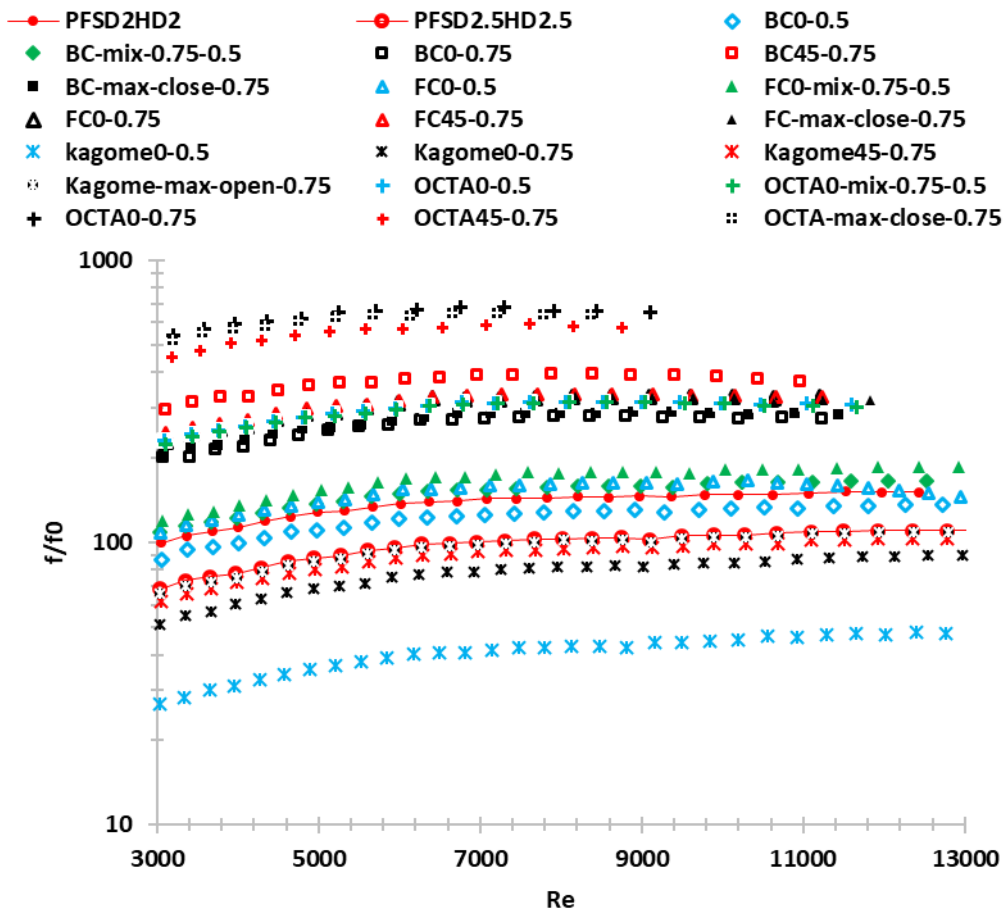

Figure 2.18 Increase in f for the tested lattices and baseline pin fins compared to the smooth channel correlation

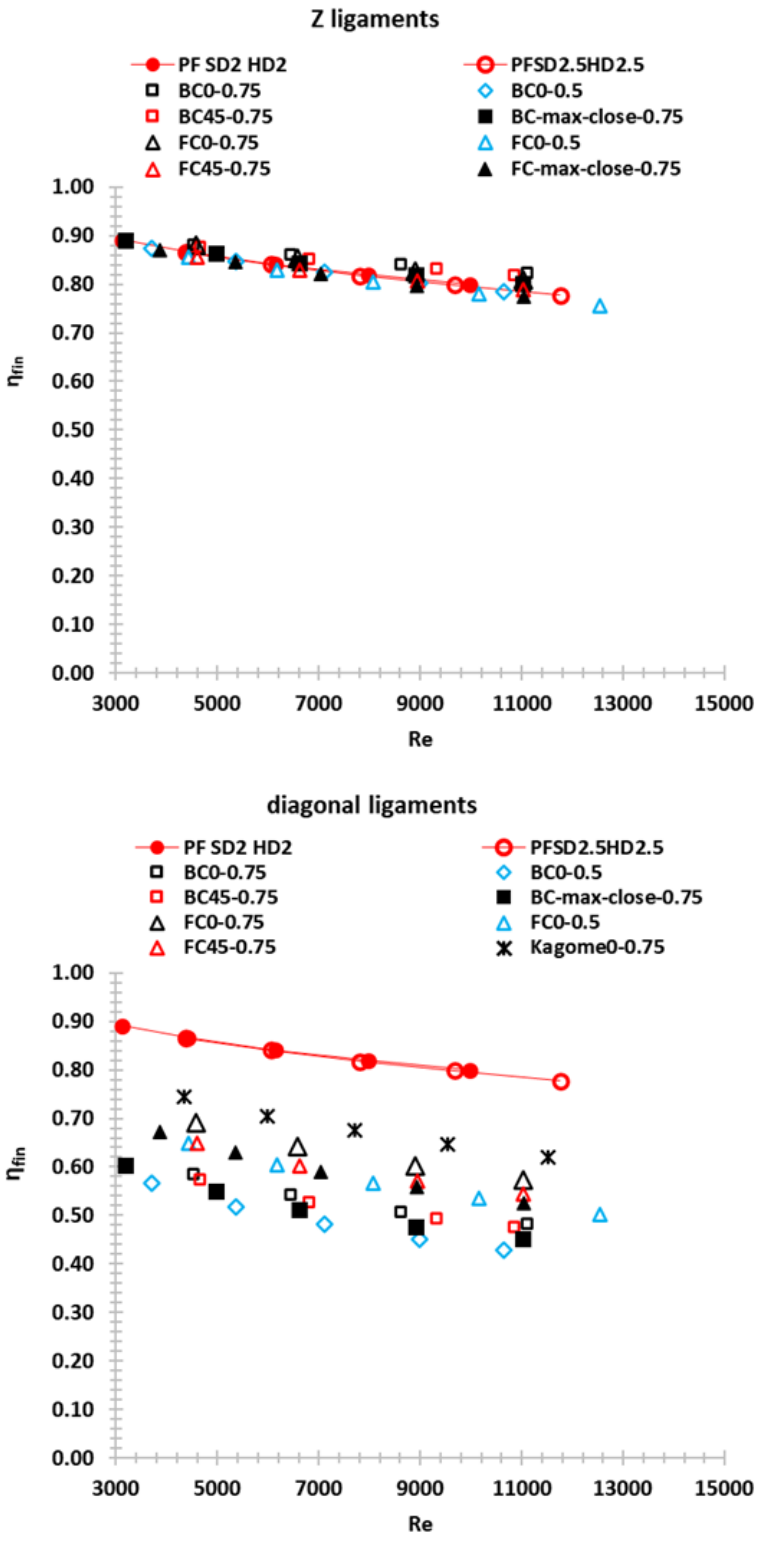

Figure 2.19 Plots depicting fin efficiency for the analyzed BC, FC, and Kagome geometries

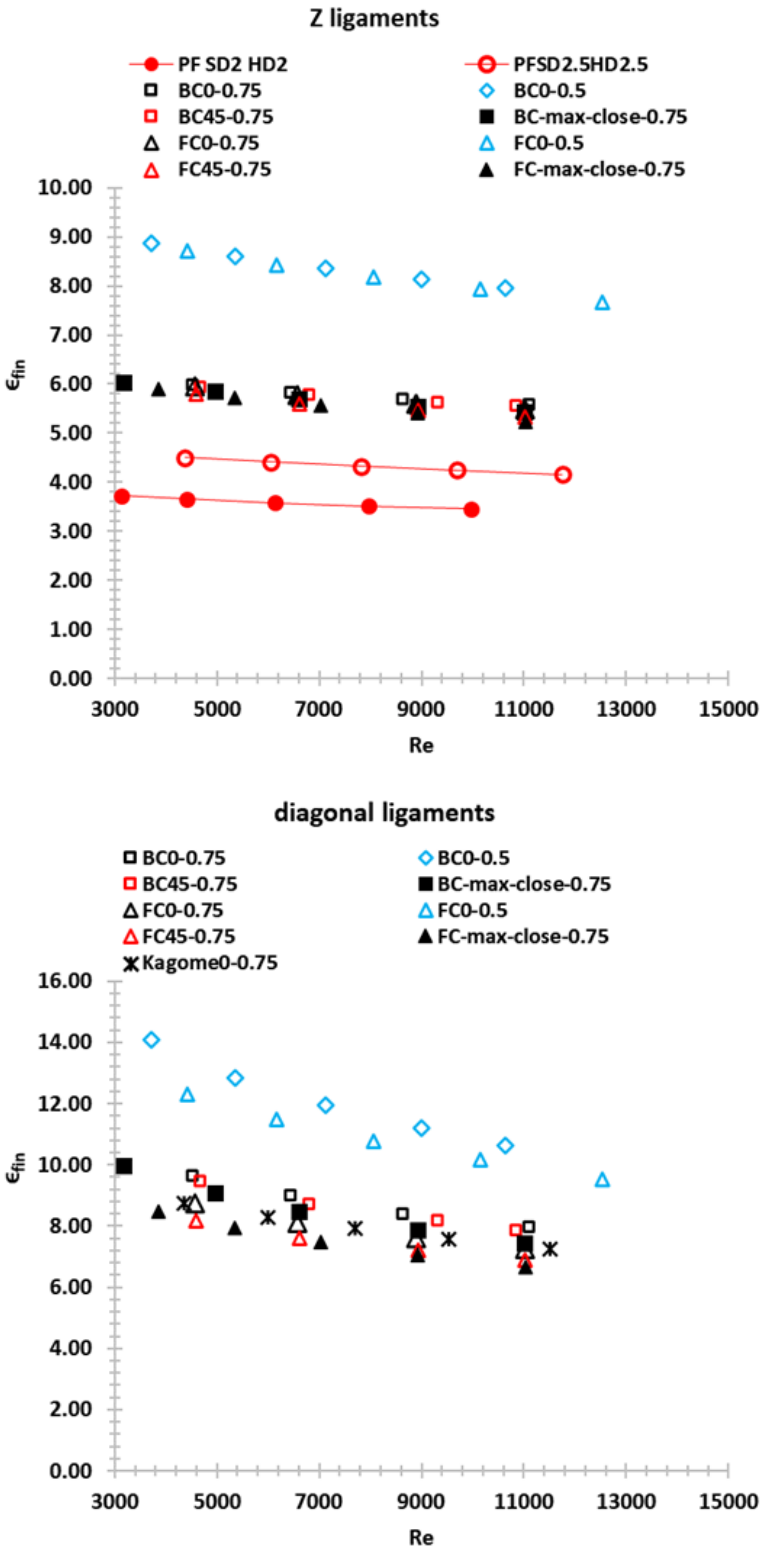

Figure 2.20 Plots depicting fin effectiveness for the analyzed BC, FC, and Kagome geometries

In order to compare the overall performance of these geometries, a performance index was defined as,

$$I_{per} = \frac{\left(\frac{Nu}{Nu_0}\right)}{\left(\frac{f}{f_0}\right)^{\frac{1}{3}}} \qquad (2.23)$$

The value of I_{per} has been plotted for all the tested geometries in Fig. 2.21. The trend in I_{per} was very different to the trends observed above for heat transfer and pressure drop individually. The Kagome lattices and maximum-blockage FC and BC lattices showed the best performance with I_{per} ranging between 1.1 and 1.2 at higher Re values. The I_{per} for the remaining lattices ranged between 0.7 – 1 near the higher end of Re range. Overall, the pin fins had the highest performance for the reasons discussed above.

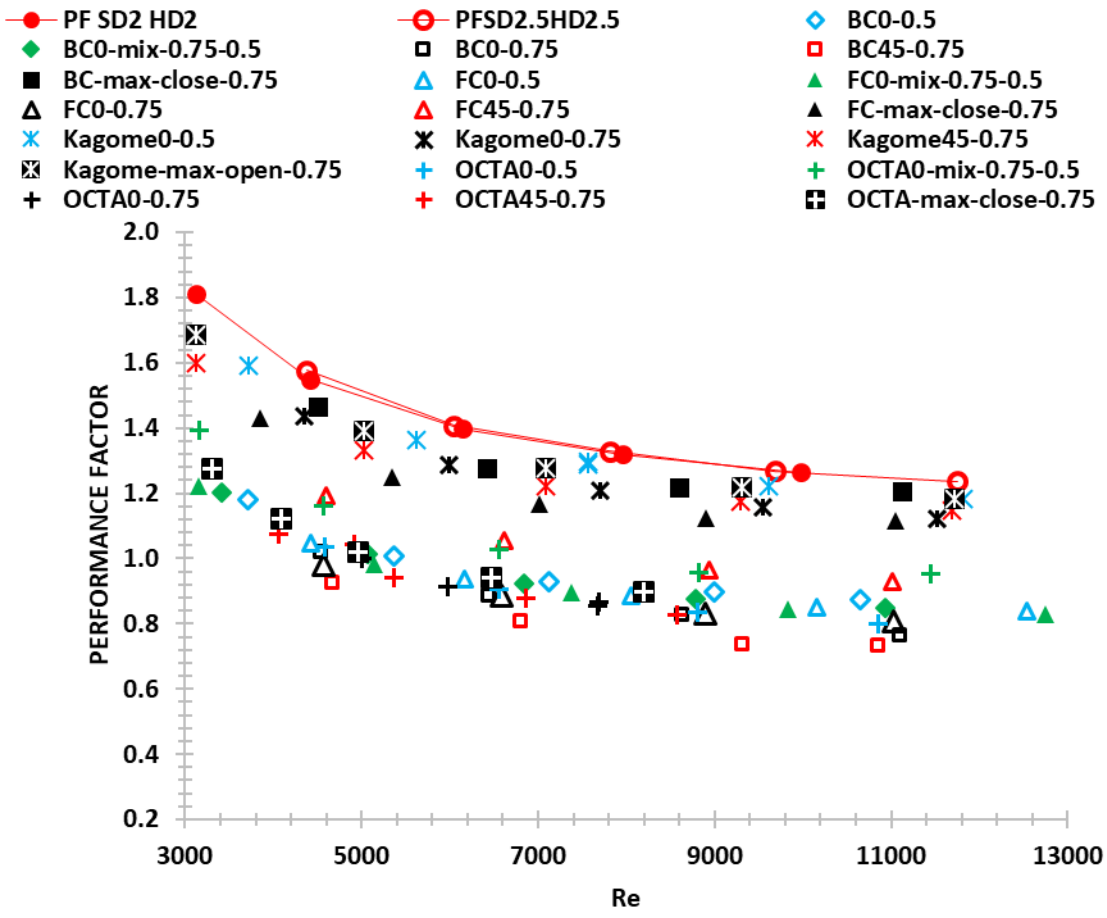

Figure 2.21 Comparison between the overall performance of the lattices and baseline pin fin geometries

In summary, it was shown that the complex lattice geometries could be successfully fabricated using the DMLS AM process and IN718 superalloy powder. A self-supporting 45° orientation w.r.t. the build plate was shown to be suitable to print the BC, FC, OCTA, and Kagome lattices with ligament diameter ranging from 0.5 mm to 0.75 mm. The aerothermal characterization of these lattices showed that these geometries achieved several times higher heat transfer compared to a smooth channel and provided an alternative technology for internal cooling of gas turbine airfoils. However, this augmentation was also accompanied by high pressure drop. It was shown that the aerothermal characteristics of lattices not only depended on the topology of the unit cell,

but also on the ligament diameter and orientation of the lattices w.r.t. the incoming flow. The dependency on these two parameters was observed to be somewhat complex in nature and highly dependent on the lattice type. Overall, the OCTA lattices provided the highest heat transfer among the tested lattices, and Kagome provided the lowest. However, the Kagome, and max-close configuration of FC and BC lattices showed the best overall performance when considering both f and Nu together.

3.0 Investigation of End Wall Heat Transfer Coefficient in Lattice Geometries: Effect of Topology and Orientation

In the previous chapter, the overall averaged heat transfer and pressure drop within the BC, FC, OCTA, and Kagome lattice geometries were obtained. These overall averaged Nu values included the heat transfer from both the lattices as well as the end walls. Given the complexity of the lattice geometries, it was expected that the distribution of heat transfer coefficient on the end wall would vary from one lattice type to another. The airfoils present in the gas turbine engine are exposed to high temperature combustion gases which flows on the external side of these components. The extended surface geometries help in cooling these airfoils primarily by conducting away the heat from the end wall and into the internal coolant stream. As a result, the footprint and adjacent areas on the end wall are better cooled than the end wall regions which are located further away from these cooling structures. The cooling of these farther regions depend mainly on the strength of local convection. Thus, it was very important to quantify the distribution of the local heat transfer coefficient on the entire end wall region of lattice-embedded cooling channels. For this, transient liquid crystal (TLC) thermometry experiments [15,16,45,107–110] were conducted. These lattices were made thermally inactive so that only the end wall heat transfer could be isolated. The diameter was maintained constant while two orientations, $\theta = 0°$ and 45°, were tested at a range of channel Re. This research provided an insight into the effect of both topology and orientation on the end wall h. Such a data is lacking in the literature. In addition, steady state numerical simulations were performed to obtain an understanding of the prevalent flow field and its impact on the observed distribution of end wall h in the tested lattices.

3.1 Scaled-up Lattice Geometries

The lattice geometries for these tests were also generated using the BC, FC, OCTA, and Kagome unit cells, similar to the previous chapter. The base of the unit cells was maintained as a square of side a = 4 mm, and the height of the unit cells, H, was fixed at 2.54 mm. Only one value of the ligament diameter, d = 0.75 mm, was used for all the lattices during these tests. On the other hand, two values of orientation, $\theta = 0^o$ and $\theta = 45^o$, were considered for the cubic BC, FC, and OCTA lattices, while the Kagome lattices were tested only for the 0^o flow. The nomenclature defined in Chapter 2 was preserved and the lattices with 0^o orientation were named as BC0, FC0, OCTA0, Kagome0, while those with 45^o orientation were referred to as BC45, FC45, and OCTA45. The suffix indicating the diameter was dropped from the names here for simplification since a constant diameter was used for all the ligaments across all the lattices. The lattices were uniformly scaled up by 5 times because the original dimension was deemed too small to conduct these tests and would have required optical magnification to adequately resolve distribution of h on the end walls. Since the lattices consisted of repeated structure in the spanwise direction, data from a single array of unit cells at the center of the channel was sufficient to characterize the end wall h. However, to eliminate the effects from the side walls of the channel and maintain the spanwise periodicity of the flow, an additional buffer array was included on both sides of the central unit cell array. Thus, the BC0, FC0, OCTA0, and Kagome0 lattices consisted of 3 × 6 inline array of unit cells. The BC45, FC45, and OCTA45 lattices consisted of 2 × 6 inline array of unit cells where half unit cells were present on both sides of the central array.

In addition to the lattices, a standard pin fin configuration, PFSD2.5HD2, was also fabricated with H/D = 2 and S/D = 2.5. The pins were arranged in a staggered array with 8 rows such that each alternating row consisted of 4 and 3 pins, respectively. The pin fins served two

purposes: 1) to establish the validity of the test setup, and 2) to serve as a baseline extended surface geometry to compare the lattices. These geometries are shown in Fig. 3.1, and the key details for each configuration are summarized in Table 3.1.

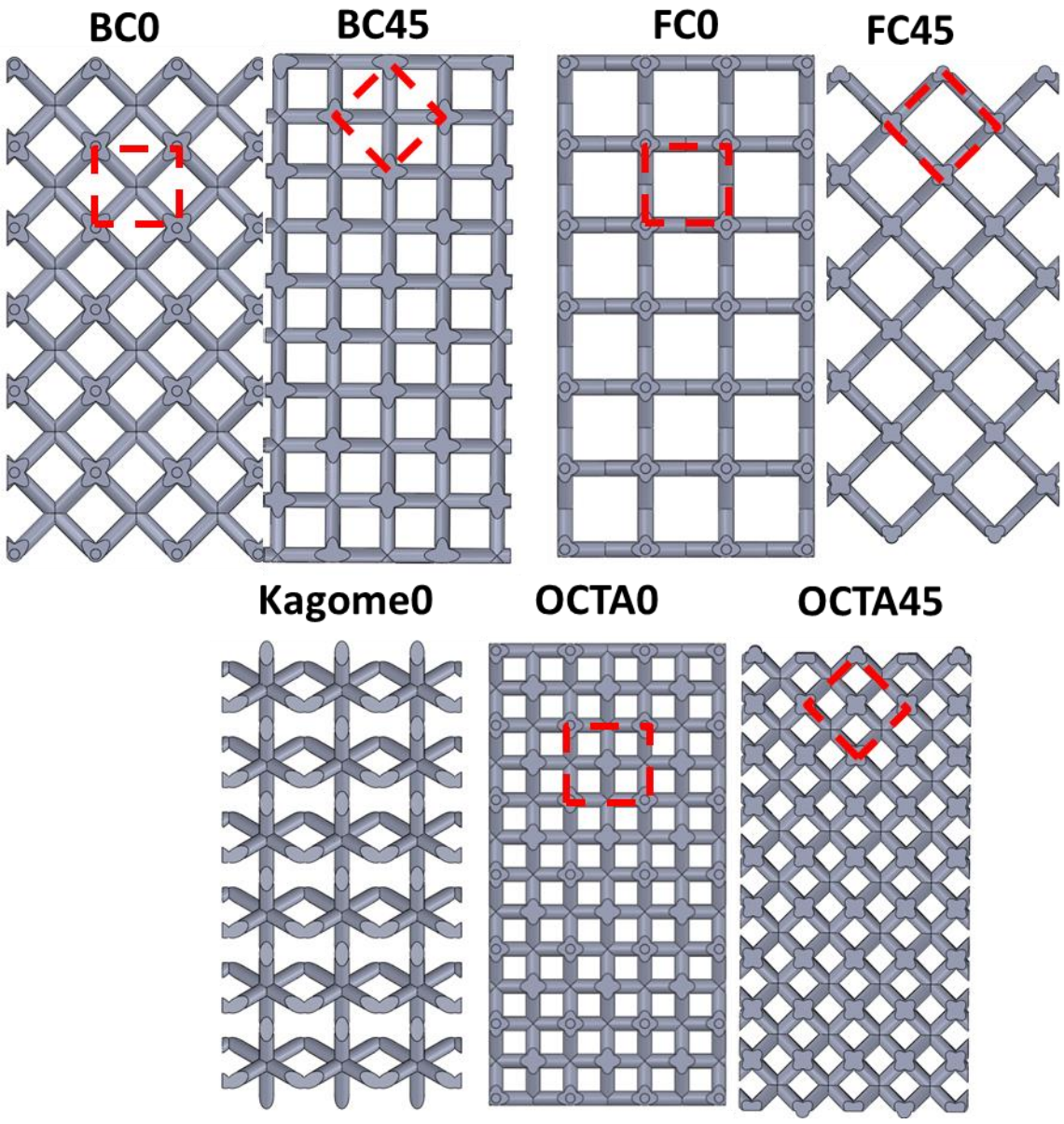

Figure 3.1 Lattices generated from the above unit cells for both 0º and 45º flow orientations. The unit cells are highlighted in red.

Table 3.1 Key geometric parameters

Lattice name	Θ	d (mm)
BC0	0°	3.75
BC45	45°	3.75
FC0	0°	3.75
FC45	45°	3.75
OCTA0	0°	3.75
OCTA45	45°	3.75
Kagome0	0°	3.75

3.2 Fabrication of Lattice Samples using Stereolithography (SLA) AM Process

For the TLC tests, the lattices needed to be thermally inactive so that their effect on end wall heat transfer could be minimized. Therefore, the lattices were fabricated using SLA additive manufacturing process [111]. This process utilized a low conducting polymer to print the geometries in a layer-by-layer fashion. In contrast to the DMLS AM process, this process utilized a photosensitive polymer. First, a layer of the polymer was applied on the build platform. An ultraviolet laser was used to scan the surface of this polymer layer, curing and solidifying a cross-section of the geometry. The build platform was then moved down by a layer thickness, followed by application of a fresh layer of liquid resin. The process of scanning was repeated, and in this way, each of the lattice part was fabricated. Finally, the part was retrieved, and the remaining polymer and support structures were removed. Some sample lattices fabricated using this process are shown in Fig. 3.2. This process has high precision, and thus, the surface roughness on the fabricated lattices were very low and were assumed to have negligible effect on the aerothermal performance. The pin fins, on the other hand, were fabricated using Nylon which had the same thermal conductivity as the resin used for fabricating the lattices ($k \sim 0.25\ Wm^{-1}K^{-1}$).

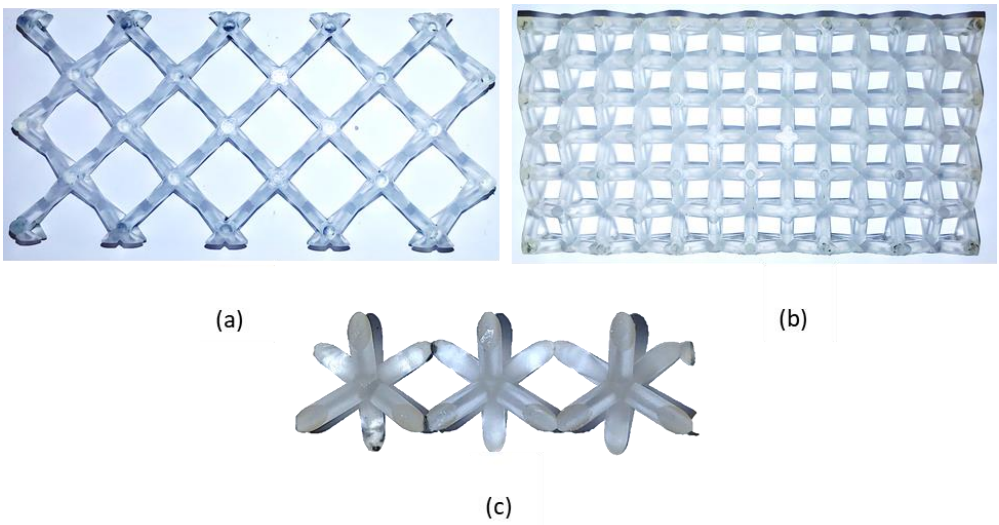

Figure 3.2 Sample of parts printed using the stereolithography method (a) FC45, (b) OCTA0, and (c) Kagome unit cells

3.3 Experimental Technique and Methodology

Transient liquid crystals are optically active organic chemicals consisting of chiral molecular structures [112]. These chemicals are temperature sensitive and change color from red to blue on an increase in their temperature within a specified temperature range and each color within the visible light spectrum appears at a particular temperature. Thus, the instantaneous temperature distribution of any surface painted with TLC can be identified by monitoring the color of TLC at different locations and matching it with a calibration chart. This calibration chart is generated a-priori for either temperature vs. hue or temperature vs. color intensity. Typically, for transient tests, the latter is preferable [113] since only one color (typically green) is tracked.

In order to obtain the heat transfer coefficient from this temperature data, the following procedure was implemented based on the assumption of transient conduction in a semi-infinite solid. The conduction heat transfer within a solid can be give as [103],

$$k\frac{\partial^2 T}{\partial^2 z} = \rho C_p \frac{\partial T}{\partial t} \qquad 0 < y < \infty, t > 0 \tag{3.1}$$

Where, C_p is the heat capacity of the wall. When a sudden change in the temperature is introduced on the TLC surface, the heat transfer problem resembles that of transient conduction in a semi-infinite solid. The boundary conditions for the TLC tests can thus be given as,

$$-k\frac{\partial y}{\partial x}\Big|_{z=0} = h(T_{wall} - T_r) \tag{3.2}$$

$$T\ (z\ =\ \infty) =\ T_i \tag{3.3}$$

$$T\ (t = 0) =\ T_i \tag{3.4}$$

where, T_{wall} and T_r refer to the wall and reference temperature, respectively. The exact solution to this transient problem is obtained in the following form,

$$\frac{T_{wall} -\ T_i}{T_r - T_i} = 1 - \exp\left[\frac{h^2\alpha t}{k^2}\right] erfc\left[\frac{h\sqrt{\alpha t}}{k}\right] \tag{3.5}$$

The wall temperature, T_{wall}, as well as the corresponding time, τ, can be obtained from tracking the color change of the liquid crystal layer. As already noted, this solution is based on the assumption that a sudden temperature change has been imposed on the TLC coated wall. In practice, it is difficult to obtain a step change in the inlet temperature during the experiments. As a result, the reference temperature, T_r, also becomes a function of time. This time dependency is accounted for by using Dulhamel's superposition theorem [114] and the solution becomes

$$T_{wall} - T_i = \sum_{i=1}^{N} W(\tau - \tau_i)\Delta T_r \tag{3.6}$$

where,

$$W(\tau - \tau_i) = 1 - \exp\left[\frac{h^2}{k^2}\alpha(\tau - \tau_i)\right] erfc\left[\frac{h}{k}\sqrt{\alpha(\tau - \tau_i)}\right] \quad (3.7)$$

Since the above solution is based on the assumption of conduction in semi-infinite plate, the thickness of the actual plate must be sufficient to validate the assumption [109]. In addition, the thickness of both the TLC and black paint layers needs to be maintained sufficiently thin, typically under 30 μm, so that their thermal resistance is low and doesn't affect the TLC readings [115].

As mentioned above, time, τ, and wall temperature, T_{wall}, were needed to obtain the h within the test domain. For this, each video frame from the experiment was processed to obtain the time taken by each pixel to reach the maximum green intensity. The time was calculated from the start of the experiment when the hot air was suddenly introduced and the pixels were black. A time history for variation in intensity for each pixel was monitored. From this history, the frame where the maximum intensity in the green channel occurred, was obtained. This information was then used to calculate time, τ. A custom MATLAB [116] script was developed to perform these calculations. Fig. 3.3 shows a sample of frame vs a pixel's green channel intensity during a TLC experiment. It was observed that the intensity of the pixel had some fluctuation due to noise in the camera sensor. This noise was minimized by fitting a curve through the intensity data. The curve fitting method selected here was the Savitzky-Golay [117,118] filter. This data, in conjunction with the temperature measurement, was used in an inhouse program to obtain the heat transfer coefficient, h, at each pixel location, as described above.

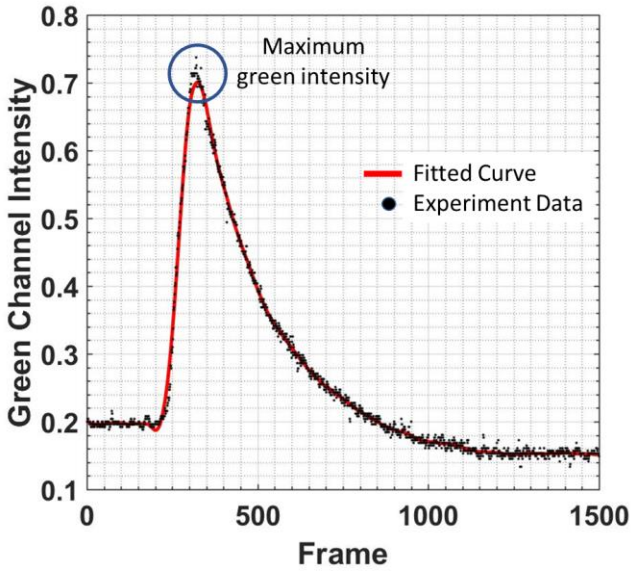

Figure 3.3 Variation of green channel intensity with video frame. Savitzky-Golay filtering has been applied to minimize the effect of noise on determination of the frame number at peak intensity.

The lattices were embedded inside a rectangular channel which was 12.7 mm high, 63.5 mm wide, and 150 mm long. All the walls of the channel were fabricated using 12.7 mm thick acrylic sheets, which allowed optical access to the internal TLC paint coating and also minimized conduction losses. The walls of the channel contained ports to allow instrumentation using thermocouples and pressure sensors. In addition, a flow development section was used upstream of the test channel to ensure that the flow was fully developed, large flow structures were broken down, and that the flow was straightened before entering the test section. A sample channel is shown in Fig. 3.4. The inside surface of the channel wall where the *h* value was needed, was coated with a thin layer of liquid crystal paint. A narrow band TLC paint, SPN100R36C2W [119], was used for these tests which had a temperature range of 36° - 38° C. Multiple coats were applied based on the direction of the manufacturer, followed by a few layers of water-soluble black paint to help improve the contrast of TLC color. Since the BC, FC, OCTA, and pin fins were symmetric

about the channel midplane, only one of the end walls was prepared with the TLC paint and monitored during the tests for color changes. In case of the Kagome lattice, both end walls had to be coated with TLC paint and monitored individually using two separate digital cameras.

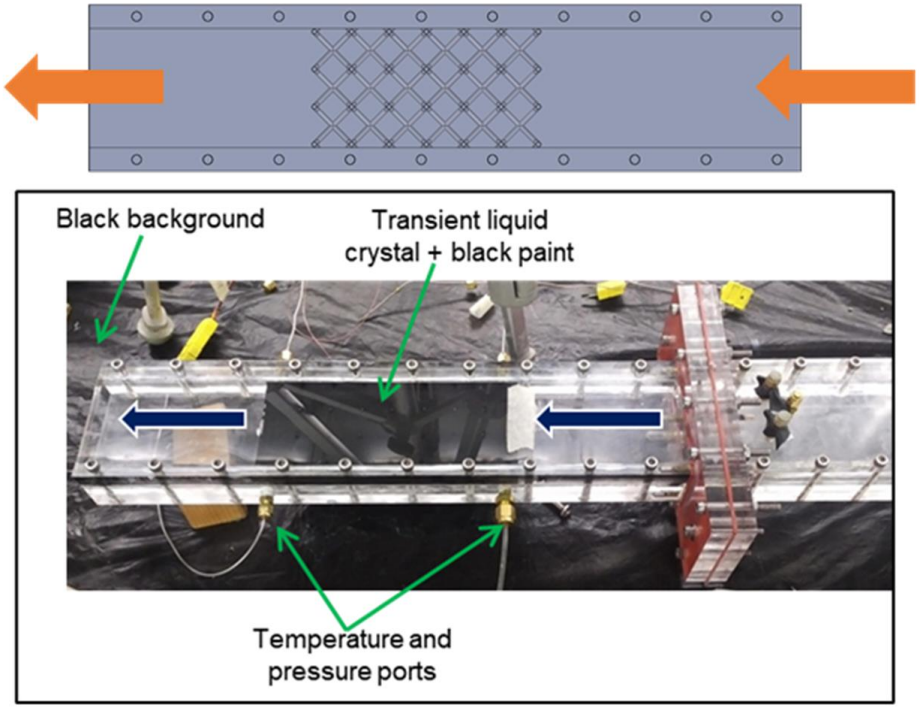

Figure 3.4 Sample test channel with embedded lattice

Figure 3.5 shows the overview of the experimental facility used for the TLC tests. The facility consisted of a compressed air supply from which room temperature air was tapped and passed through a filter to remove any debris. This filtered air was then passed through a rotameter and pressure regulator to set the desired flow rate. The metered air then flowed through an inline heater which was connected to a variable voltage transformer to adjust the heating power and achieve desired air temperature for the tests. The assembled test section was connected downstream from the inline heater. To start the test, first, air was supplied from an in-house

compressed air reservoir. Five Reynolds numbers, ranging from ~5600 to ~18800, were used which were based on the channel hydraulic diameter.

The flow was first setup for the required Re by metering through the upstream rotameter. Once the required flow rate was obtained, the temperature and pressure readings were taken for the channel and the rotameter. The flow was then diverted away from the channel inlet through a by-pass valve and an inline heater was switched on to heat the incoming compressed air to about 70^{o} C. Once this temperature was reached, the by-pass valve was closed to introduce the air into the test channel, creating a step change in temperature as required by the TLC method. The temperature readings were recorded in the channel using K-type thermocouples with a 30 Hz frequency at upstream and downstream locations of the test geometries. The change in the color of the liquid crystal layer was captured using a digital camera located perpendicular to the lit test surface.

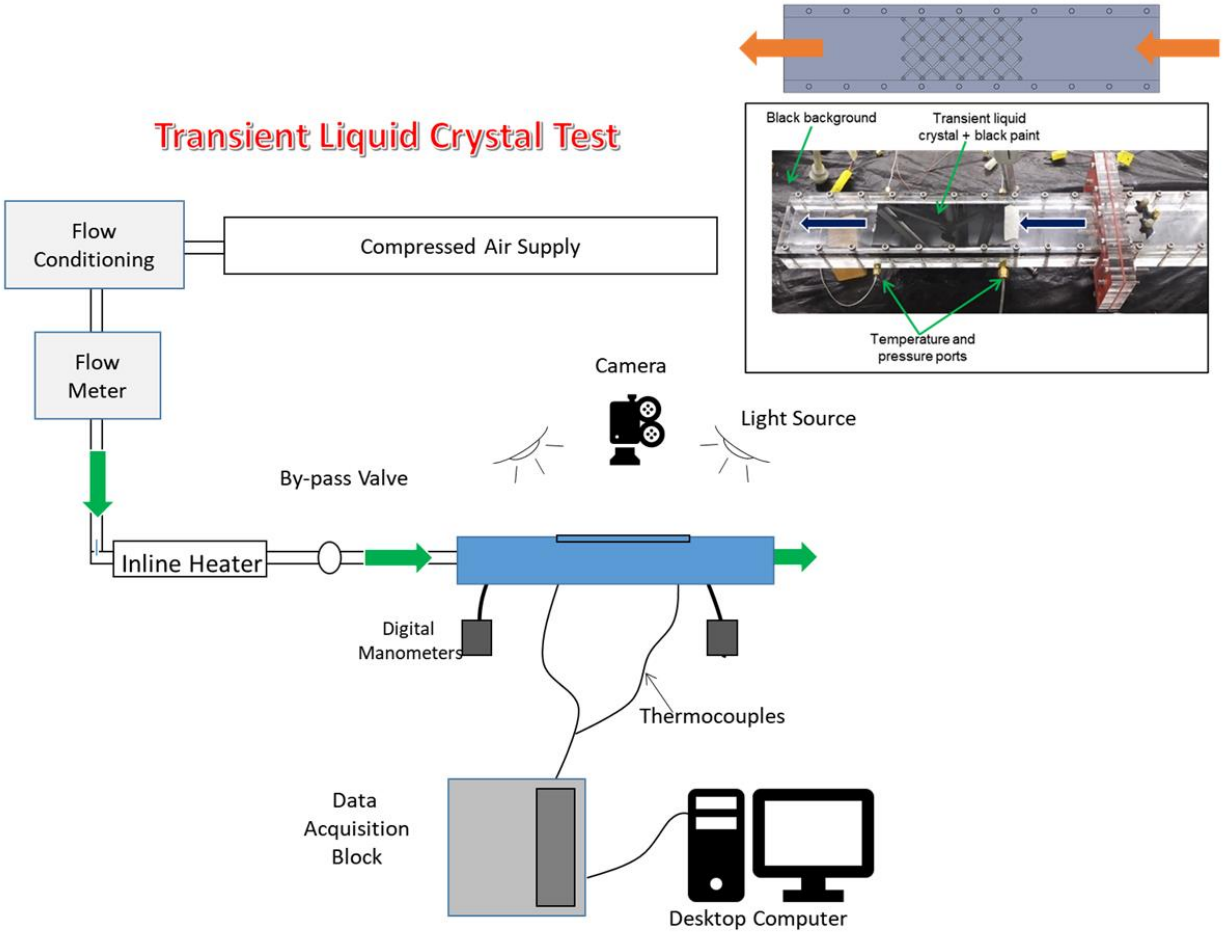

Figure 3.5 Test setup schematic for transient liquid crystal technique

3.4 Experiment Results and Discussions

3.4.1 Heat Transfer in Baseline Pin Fins

In this section, the results of the pin fin geometry have been compared with that from the literature. This was done in order to validate the newly established TLC test rig. Both the Reynolds number and the Nusselt number for the pin fin banks were defined using the pin diameter as the

reference length. Additionally, the maximum flow velocity, U_{max}, within the bank was used for the Reynolds number, which is a common practice in pin fin literature [120]. Thus,

$$Re_{D,max} = \frac{\rho U_{max} D}{\mu} \quad (3.8)$$

$$Nu_D = \frac{hD}{k} \quad (3.9)$$

This pin fin configuration was similar to that used in [18] and thus, the results of the present pin fin experiments have been compared with their results (Fig. 3.6). The overall averaged heat transfer values, represented as $Nu_{D,ave}$, compared within 5% of the $Nu_{D,ave}$ values in [18]. In addition, the ratio of row wise averaged Nu, Nu_{row}, to $Nu_{D,ave}$ is also plotted against the $Re_{D,max}$ both for the present experiment and that in [18] for two $Re_{D,Max}$ values. The data agreed very closely and validated the established liquid crystal experiment rig.

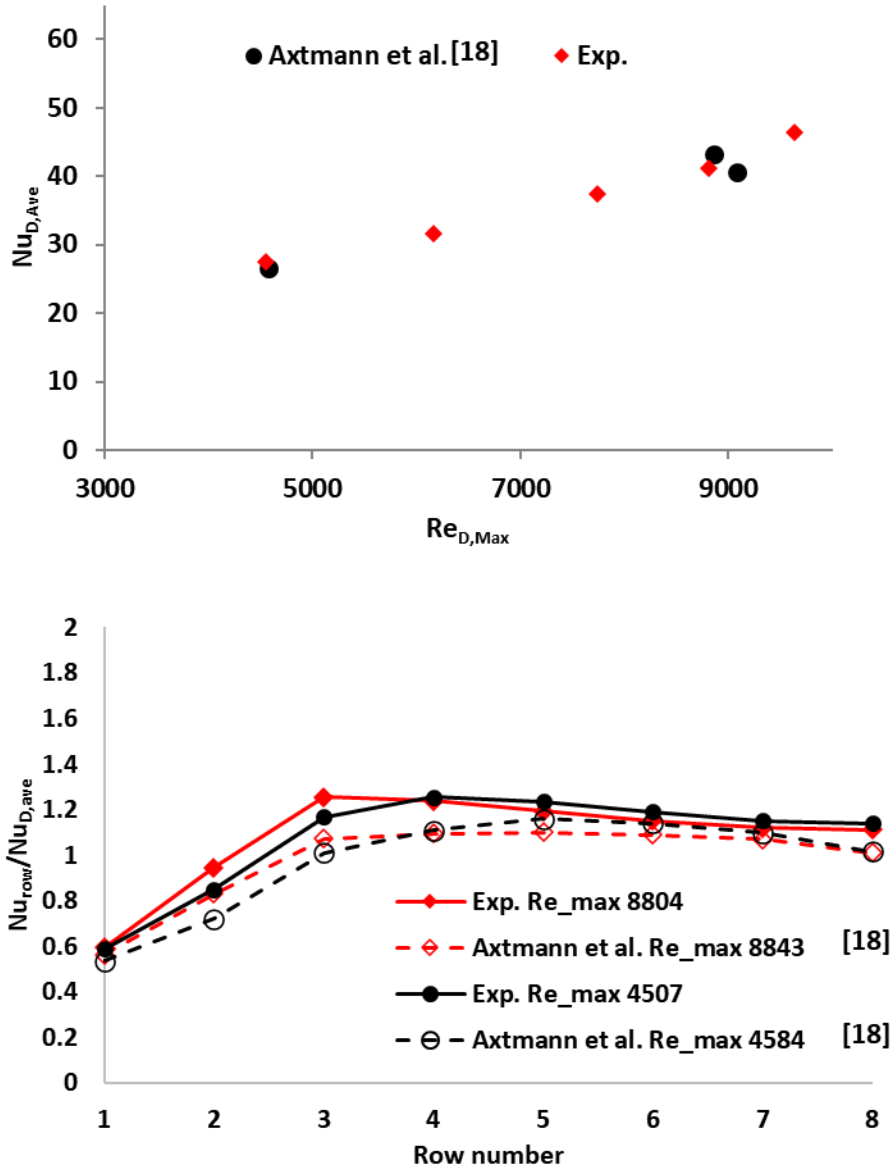

Figure 3.6 Comparison of the overall $Nu_{D,ave}$ between the current experiment and literature data (top); comparison of row-wise averaged Nusselt number ratio between the experiments and literature data (bottom)

3.4.2 Local Distribution of Heat Transfer Coefficient on End Walls of Lattice Channels

The distribution of the local h on the end wall of channels with lattice cooling geometries has been shown in Fig. 3.7 for *Re* ~ 11,600. This distribution has been shown only for the central

unit cell array to eliminate effects from the channel side wall. As discussed previously, given the spanwise periodicity in these geometries, the result from a single middle row was sufficient to characterize the distribution of heat transfer coefficient. The result from the pin fin geometries has also been shown in the figure in order to highlight the differences between the two types of geometries.

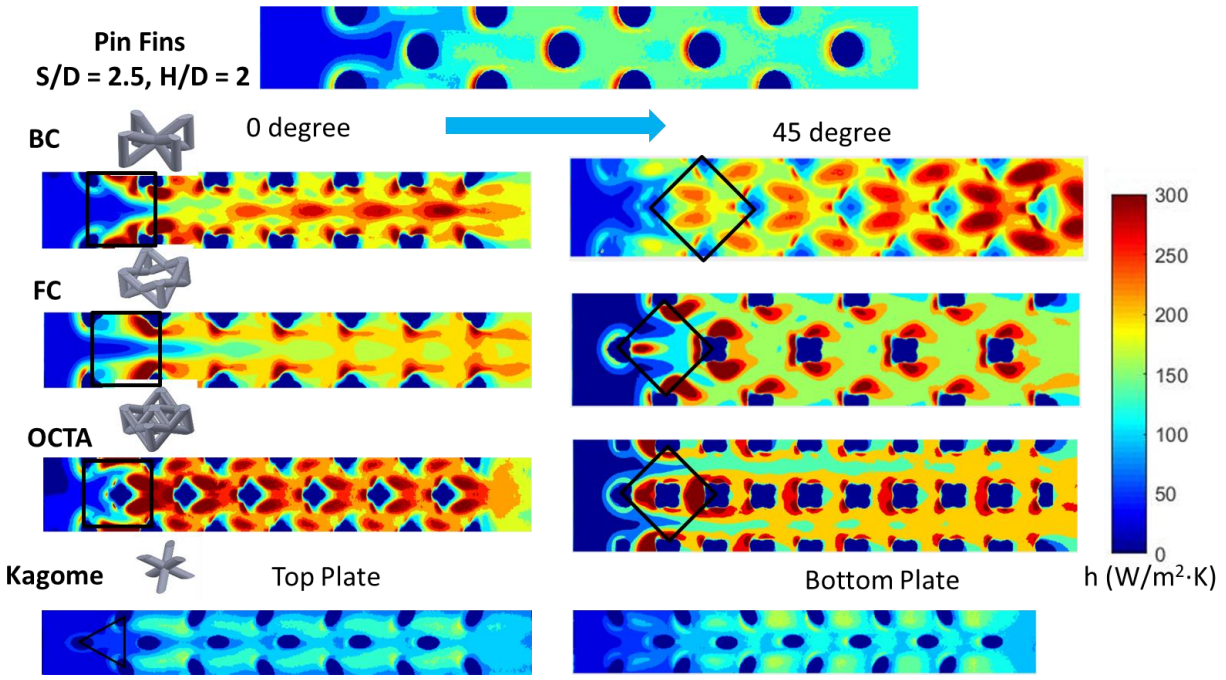

Figure 3.7 Local distribution of h on the end wall for lattice and baseline pin fin channel at Re ~ 11,600

Each of the lattice geometries depicted a unique distribution of h on the end wall. In case of BC0, two distinct regions of high heat transfer were present. The first region was located near the vertices, including the wake behind the vertices, while the second region was located along the center of the unit cell array. Two mechanisms were responsible for the high h in the first region. In this region, the incoming flow impinged on the first row of ligaments and rolled up, creating a relatively high heat transfer region around the leading vertices akin to the horse-shoe vortex

observed in pin fins [16–18,120,121]. Additionally, a large wake region developed behind these leading ligaments and high turbulence and mixing led to local high h there. This wake flow interacted with the downstream ligaments and created two peaks near each of the downstream vertices from the 2nd row onwards. Within the second high heat transfer region, the periodicity and location of peaks coincided with that of the body center nodes. The upstream ligaments diverted the flow towards the center of the array where a relatively larger open area was available for the flow. This diverted flow was further pushed towards the end walls by the body center node of each unit cell in the array, creating periodic peaks in h near the middle of channel. Thus, for a given BC0 unit cell in a lattice array, there were three distinct regions of high heat transfer: two regions near the vertices, and one at the center, shown in Fig. 3.8. While in BC0, the footprints of the ligaments were in an inline arrangement, in case of BC45, the footprints were staggered. When comparing distribution of h in the 1st row, BC45 depicted lower h in the wake of the 1st row of ligaments, compared to BC0. For BC45, a z-ligament appeared between two consecutive body center nodes. As a result, the relatively open flow area present at the center of the BC0 unit cell array was absent. This led to interaction of the bulk flow with these z-ligaments in the center of the array, creating peaks of h just upstream of these ligaments followed by bean shaped high h regions in the wakes. The BC45 unit cell had four high heat transfer regions, as highlighted in Fig. 3.8.

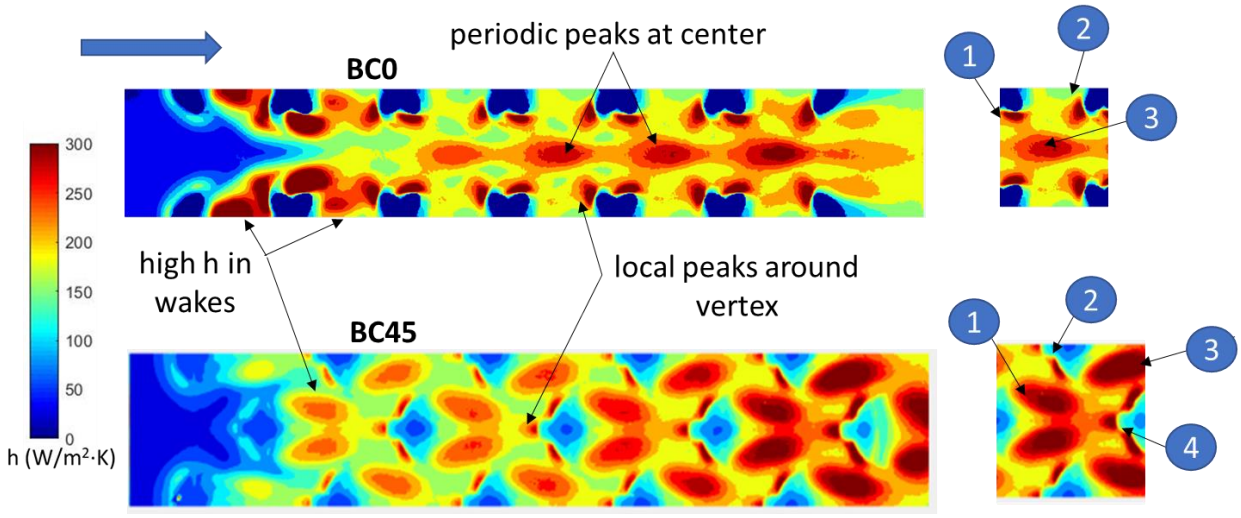

Figure 3.8 Key features in the local h on end wall and for a single unit cell in fully developed region for BC lattices

A similar heat transfer trend was observed in FC0 lattice. A prominent low heat transfer regions was observed in center of the first unit cell and extended into the second row. A high heat transfer region appeared in the upstream of the leading vertices due to the formation of horse-shoe like vortices. Similarly, peaks in h appeared near each of the downstream vertices, but instead of two distinct peaks as in case of BC0, only a single peak was present in case of FC0 due to difference in shape of the vertices. Also, there was no high h region immediately downstream of these vertices, in contrast to BC0. The FD ligaments created a node at the center of the channel and restricted the flow owing to the relatively small opening compared to the body center node in BC0. At the same time, the center of the FC unit cells did not contain any additional ligaments, creating a large unrestricted flow area which led to lower flow velocities. Thus, the h was also observed to be lower near the middle of the array and periodic dips in h were observed in the immediate wake of these nodes. This indicated that the face-center node did not enhance heat transfer, in contrast

to the body center nodes in BC0. Once again, after rotation, the ligaments in the FC45 lattice formed a staggered arrangement compared to the more inline arrangement in FC0. The staggered arrangement of the ligaments led to a markedly different h distribution compared to FC0. In FC45, all the vertices from the 2nd row onwards showed peaks in h located on their immediate upstream and on their sides. The location of these peaks and dips are highlighted in Fig. 3.9. In the downstream row with fully developed flow, FC0 unit cell showed two distinct regions of high h while FC45 unit cells showed three.

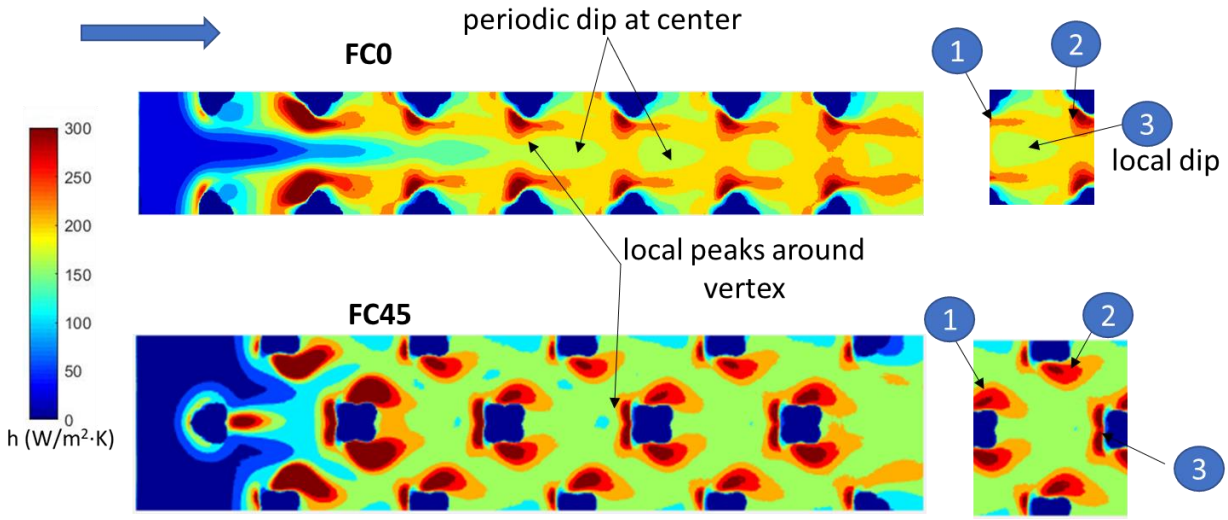

Figure 3.9 Key features in the local h on end wall and for a single unit cell in fully developed region for FC lattices

Similar to the above cases, peaks in h was also observed upstream of the 1st row ligaments in OCTA0 lattice, as well as the low heat transfer region in the middle of the 1st unit cell. However, the wake region of the upstream ligaments showed an elongated high heat transfer region, which was very different from both BC0 and FC0 lattices. High h was also observed in the upstream and downstream regions of each of the central vertices. The upstream peaks in these central vertices

increased in magnitude from 1st to the 2nd row of unit cell and then decreased for the downstream vertices. On the other hand, the magnitude of the two bean-shaped high h regions present in the wake of these central vertices decreased from the 1st row to the 2nd row while remained somewhat constant in the downstream regions. Interestingly, this pattern in h resembled that present at the middle of the BC45 lattice. While for the BC and FC lattices, rotation changed the arrangement of the vertices from inline to staggered pattern, for OCTA lattice it was an opposite case. In OCTA45, the vertices located on the sides showed peaks in h similar to vertices in BC0, however, the peaks in h near the central vertices showed an alternating higher and lower magnitude from first to last row. The peaks around the vertices corresponding to the z-ligaments had greater magnitude than those near the vertices formed by the OD ligaments. Also, the peak in upstream of each vertex was higher compared to the peaks located on their sides. Overall, in the fully developed region, the unit cells in both OCTA0 and OCTA45 lattice showed four distinct regions of high h. Fig. 3.10 highlights these regions.

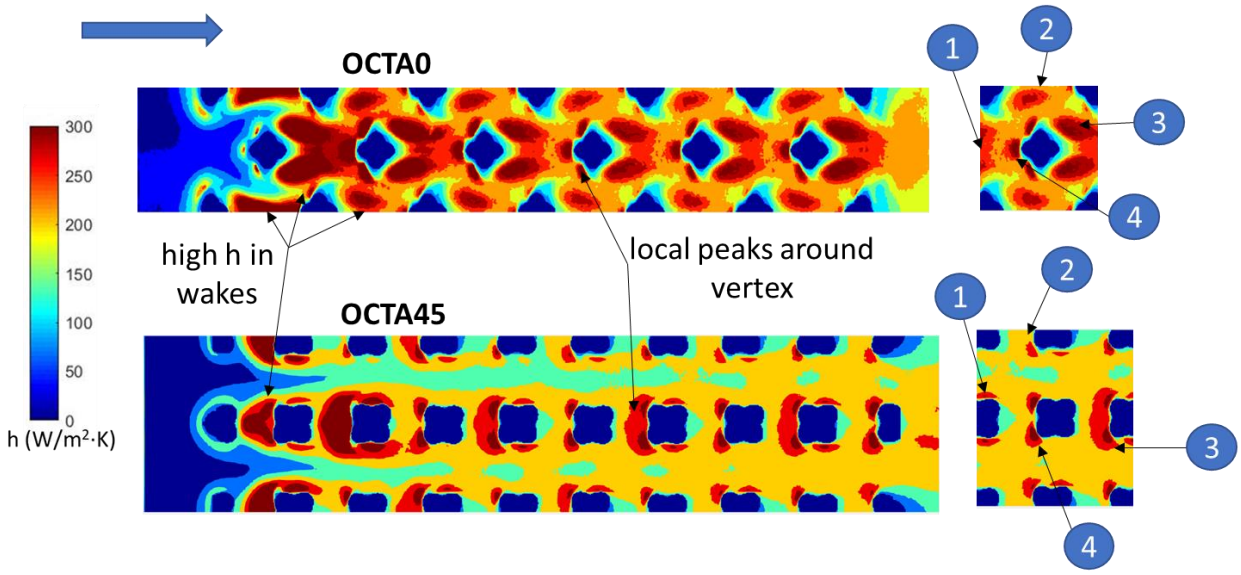

Figure 3.10 Key features in the local h on end wall and for a single unit cell in fully developed region for OCTA lattices

The above lattices with cubic unit cells showed a symmetrical heat transfer on the top and bottom end walls. On the other hand, the local distribution of h varied between the top and the bottom end walls for the Kagome lattice (Fig. 3.11). In the top half of the channel, the two downstream ligaments of each unit cell were inclined in the streamwise direction while the third ligament was inclined in the anti-streamwise direction. The case was opposite for the bottom half of the channel. In case of the top plate, the overall heat transfer was observed to be lower compared to the bottom plate. The high h regions were elongated in shape and located behind the streamwise inclined ligaments. Such a pattern was created because the streamwise inclined ligaments directed secondary vortex flows towards the top plate [14,30,37], resulting in a markedly different flow field in the two halves of the channel. For the bottom plate, the distribution in h was observed to be more uniform and consisting of a wide high heat transfer region in the wake of the anti-

streamwise inclined ligaments. Once again, the upstream of each vertex also depicted high heat transfer which resembled the heat transfer enhancement due to horse-shoe vortices in pin fins.

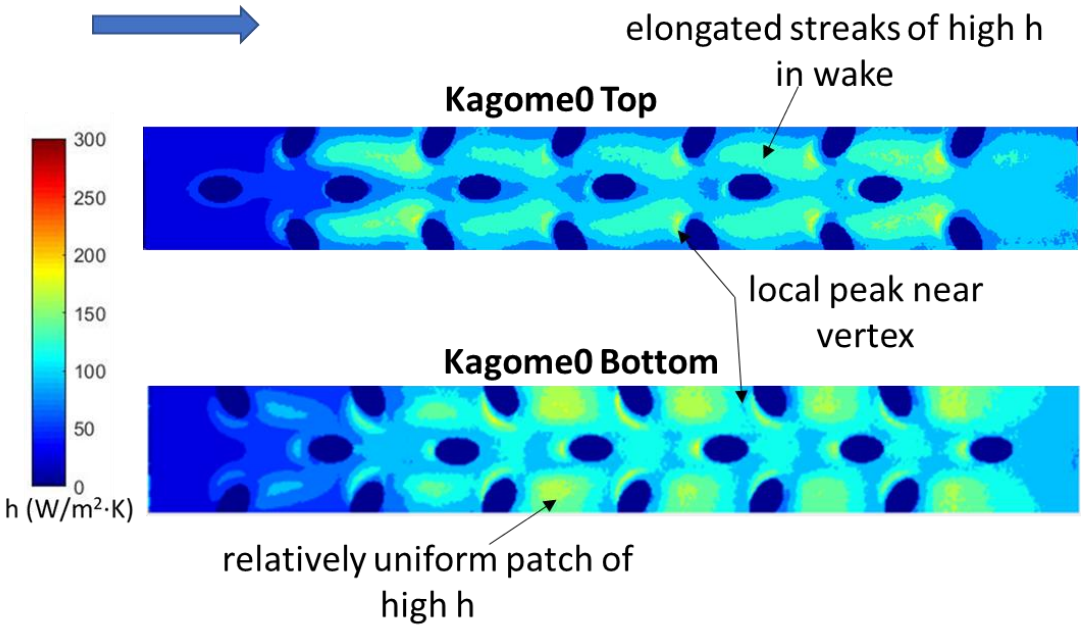

Figure 3.11 Key features in the local h on end walls for Kagome lattice

3.4.3 Overall Averaged Heat Transfer Coefficient for Fully Developed Region

Fig. 3.12 shows the overall averaged end wall Nu and Fig. 3.13 shows its enhancement in lattice geometries compared with a smooth channel. Both these plots showed that the highest heat transfer occurred in the OCTA0 lattice, specially at high Re, and lowest for the Kagome. In all cases, the augmentation in end wall Nu was very similar between the non-rotated and rotated lattices. An important conclusion drawn from these results was that the difference in the performance due to change in orientation, as observed in conjugate heat transfer tests, could be attributed to the extended surface effect of the lattices. All the tested lattice geometries performed better than the baseline pin fin case.

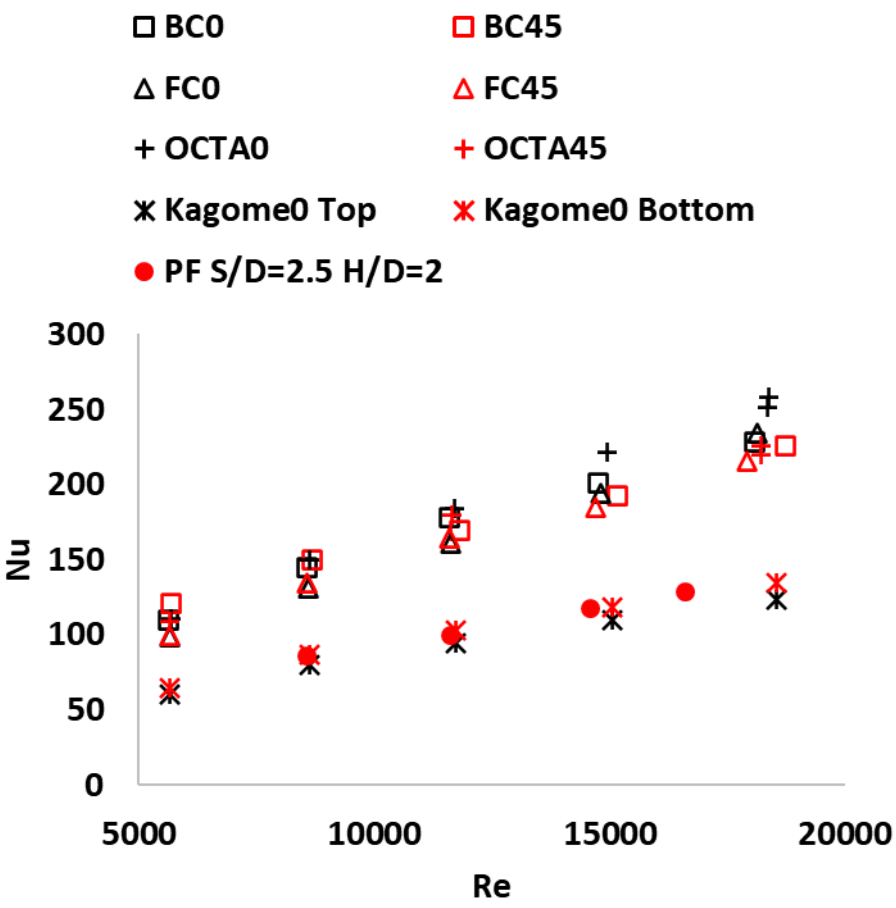

Figure 3.12 Overall averaged Nu on the end wall for the tested lattices

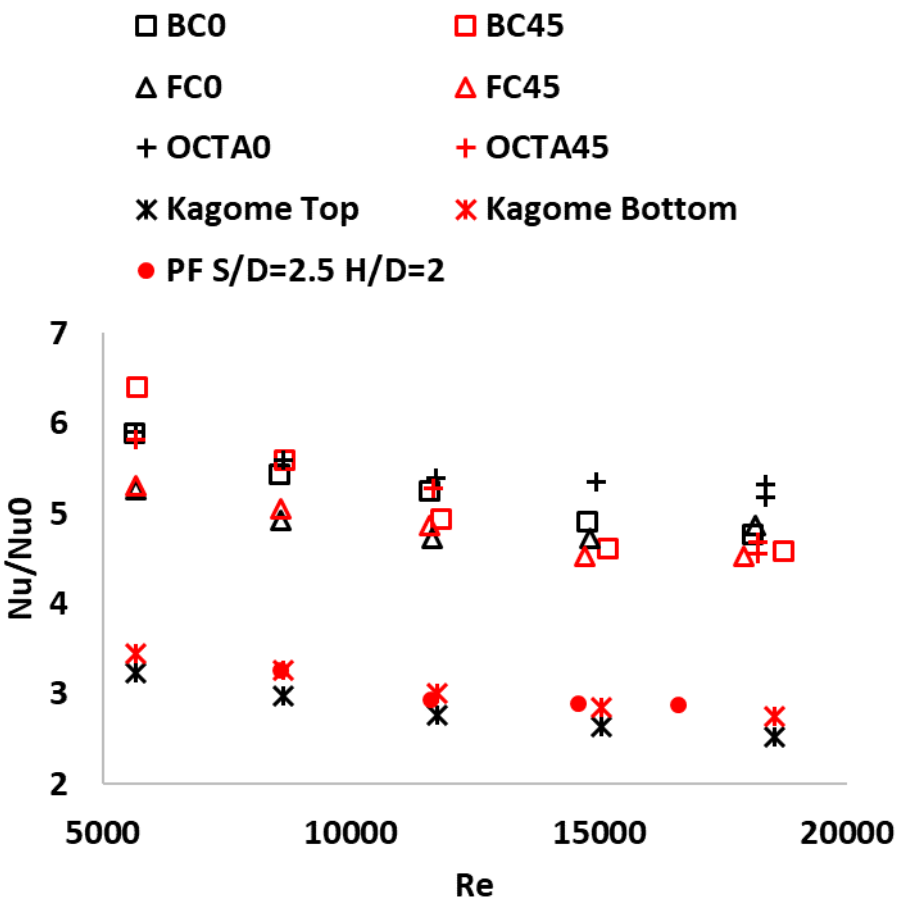

Figure 3.13 Heat transfer enhancement compared with smooth channel correlation

3.5 Numerical Analysis of Flow Field in Cooling Channels with Lattice Geometries

The complexity of the lattice geometries led to unique distribution of the local heat transfer coefficient on the channel end wall. The distribution was not only affected by the unit cell topology but also by their relative orientation with respect to the flow. Thus, this part of the research provided an insight into the underlying flow field in these geometries and bring a deeper

understanding to the observed thermal-flow characteristics. A numerical study was conducted in order to achieve this insight and is presented in the following section.

The numerical setup for these studies consisted of the fluid domain of the cooling channel with the corresponding lattice geometry embedded inside it. Similar to the TLC experiments, only a single array of the lattice with six inline unit cells was considered. Furthermore, for the BC, FC, and OCTA lattices, only a quarter of the geometry was used to prepare the corresponding numerical domain due to the presence of two planes of symmetry, as shown in Fig. 3.14 . The first symmetry plane was the xz plane at the middle of the array. The other symmetry plane was parallel to the xy plane and was located at H/2. Such partial geometry was deemed sufficient for characterizing the thermal and fluid performance of the whole lattice when appropriate boundary conditions are implemented. On the other hand, one plane of symmetry was present in the Kagome lattice and thus, half of the Kagome channel was used for the simulations. In addition, the numerical domain consisted of three regions: the inlet extension, the channel with the lattice geometry, and the outlet extension. The inlet extension allowed for the flow to develop before entering into the channel while the outlet extension allowed for the flow to settle down to help with the convergence. The solid domain was not included in any of the numerical models because the analysis was performed to match the TLC test conditions in which the lattices were assumed to have negligible contribution to the overall heat transfer.

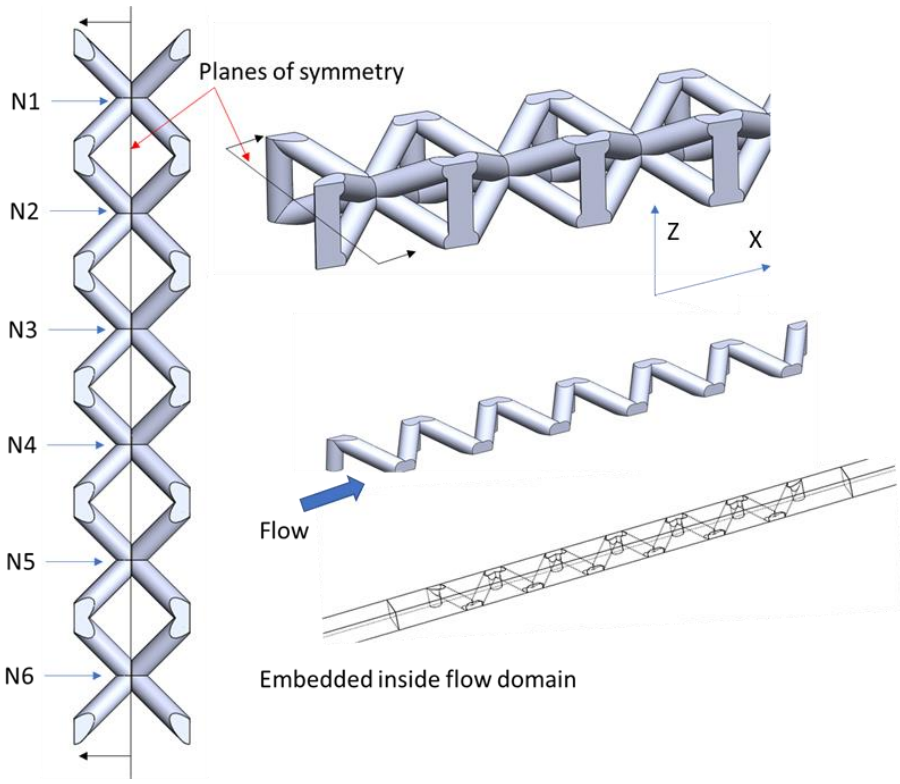

Figure 3.14 BC0 lattice highlighting the planes of symmetry and the coordinate system for CFD

The complex nature of these geometries made it very difficult to form a structured mesh. Hence, unstructured mesh, dominated by tetrahedral elements, was generated for each of fluid domain using ANSYS ICEM [122] meshing tool. Element size and element growth rate was defined individually for all the surfaces in the fluid domain to obtain a good control on the mesh quality. In addition, inflation layers were used on all the walls so that the boundary layer could be appropriately captured in the near wall regions. The inflation layers consisted of 13 layers, with the first layer height defined to ensure that the y+ value remained below 1. This restriction on y+ value was a prerequisite for the usage of SST-kω turbulence model used in these simulations [30–32]. The numerical analysis was conducted using steady state thermal analysis in ANSYS CFX solver [123] . Test conditions from the TLC experiments with Re = 11,600 were implemented as the boundary condition for each of the run. A sample of the meshed domain and the overview of

key boundary conditions has been shown in Fig. 3.15. The air temperature at the inlet was fixed at 60° C and a velocity of 8.72 m/s, while the channel wall was maintained at 23.5° C. The walls of both the inlet and exit extensions were defined as adiabatic because they were mainly introduced for conditioning the flow and did not take part in the heat transfer. The walls of the lattice were also adiabatic since they were assumed thermally inactive during the experiments. Finally, at the outlet, a constant static pressure of 0 Pa was defined. The fluid domain consisted of air and the flow was modeled as incompressible. In order to judge the convergence, the RMS values of the residuals for the mass, momentum, and energy equations were ensured to reach under 10^{-4}. Since the problem was inherently transient, the value of key flow variables in terms of inlet pressure, outlet velocity, and outlet temperature were also monitored to ensure that the fluctuation in their values was under 0.5%. Finally, the domain imbalances of mass, momentum, and energy were ensured to be lower than 0.01%.

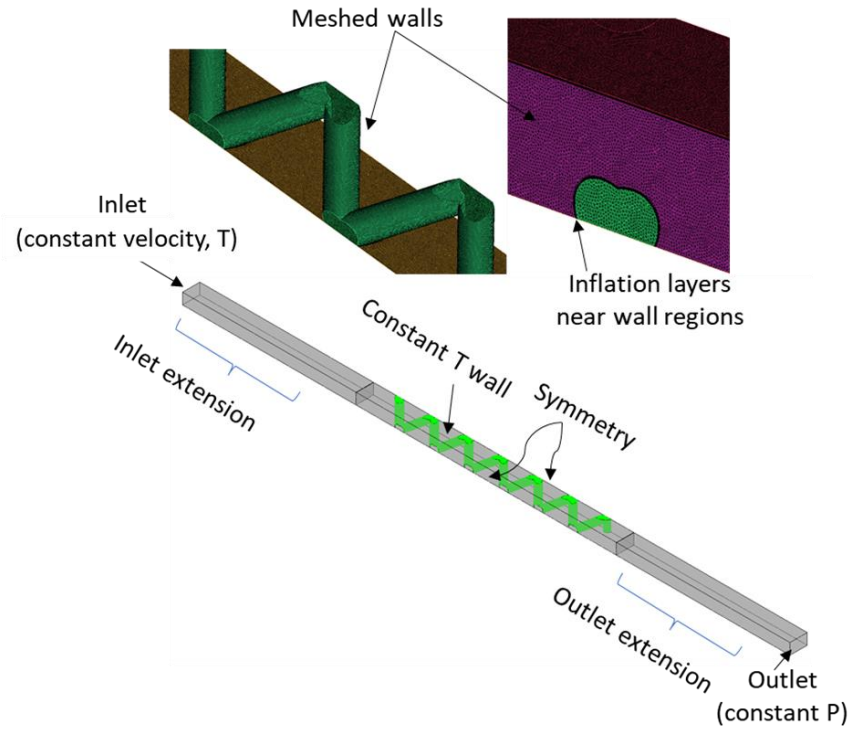

Figure 3.15 Meshed BC domain highlighting the different types of elements, domains, boundary conditions

A grid independence study was conducted first to ensure that the numerical results were not affected by the mesh density. The BC0 lattice was selected to conduct this study and three separate fluid domains were prepared with mesh densities of 4.8 M, 7.6 M and 13.6 M. Result for the area averaged h on the channel wall and pressure drop along the channel are compared in Fig. 3.16. The results showed that the calculated area averaged h varied by 1.71% and then by 1.93% on changing the mesh density from 4.8 M to 7.6 M and from 7.6 M to 13.6 M, respectively. Similarly, the change in pressure drop was only 2.3% on for a 44.3% increase in mesh density from 7.6 M to 13.6 M. Thus, the 4.8 M mesh density was sufficient to resolve the underlying flow field physics in lattices and presented good compromise between the accuracy and computation cost.

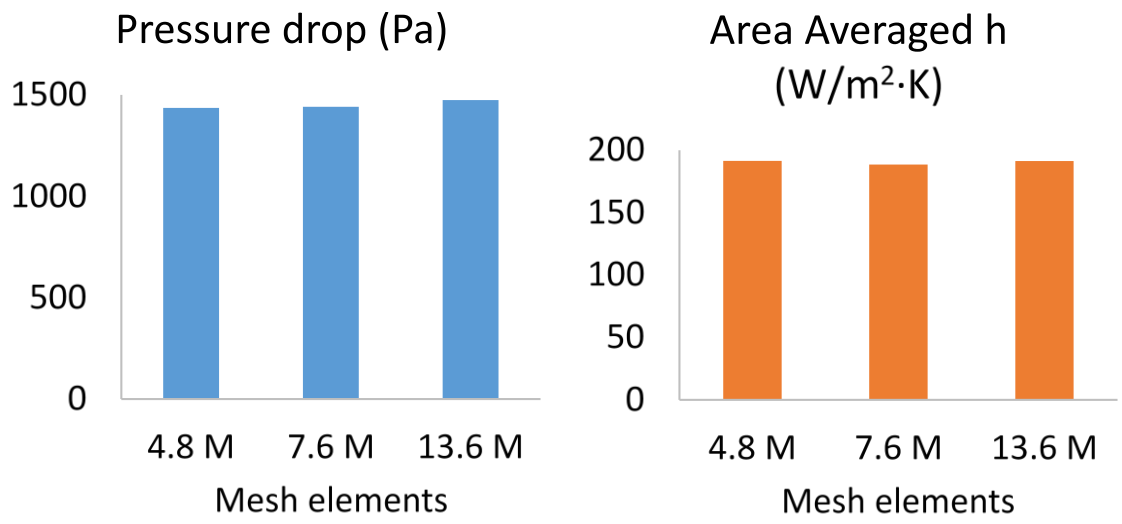

Figure 3.16 Result of grid independence study for area averaged h and pressure drop using BC0 lattice

3.6 Numerical Flow Field

The flow field for the lattices, as obtained from these numerical simulations, are summarized in Fig. 3.17 and Fig. 3.18. These numerical results revealed that the coolant flow formed virtual sub-channels which contained high-velocity flow. The shape and location of these sub-channels varied between the BC0, FC0, OCTA0, and Kagome0. Within BC0, the central body node diverted the flow towards the end walls. In addition, the relatively open area in the middle of the unit cells aligned, forming a continuous pathway for the coolant to flow through. This phenomenon was more evident in the FC0 lattice. In case of OCTA0, the presence of central node diverted the flow towards the sides, thus, creating a somewhat serpentine sub-channel. When the lattices were rotated, these flow pattern changed significantly. Interestingly, the flow pattern in

BC45 and FC45 resembled with the OCTA0, which was due to the relatively staggered arrangement of the vertices in these lattices. Similarly, the rotation of octahedral lattice to obtain OCTA45 caused the vertices to become relatively inline, thereby, causing the flow sub-channels to resemble those in BC0 and FC0. In case of Kagome0, the inclined ligaments caused the bulk coolant to move towards the bottom end wall, creating an asymmetrical flow field. This, in turn, led to a higher h on the bottom wall than the top wall, causing the asymmetry observed in experiments.

Figure 3.19 shows the velocity field for rows 2 – 4 on the xy plane located at a height of H/2 from the top end wall. Once again, the periodicity in the velocity field is evident. In case of the cubic lattices (BC, FC, and OCTA), once again, the flow at the center of the channel was largely dictated by the diversion created by the nodes. BC0, FC0, and FC45 lattices showed large wake regions with low speed flow near the center of the unit cells. Such low-speed flow regions were also present in wake of central node of Kagome0 unit cells. On the other hand, these regions were reduced in size in the BC45, OCTA0 and OCTA45 lattices. These results revealed quite unique flow field within single layer lattice geometries. The formation of virtual sub-channels with high-speed flow can be used to favorably redistribute the coolant within the flow channel, which is difficult to achieve using traditional geometries such as pin fin banks.

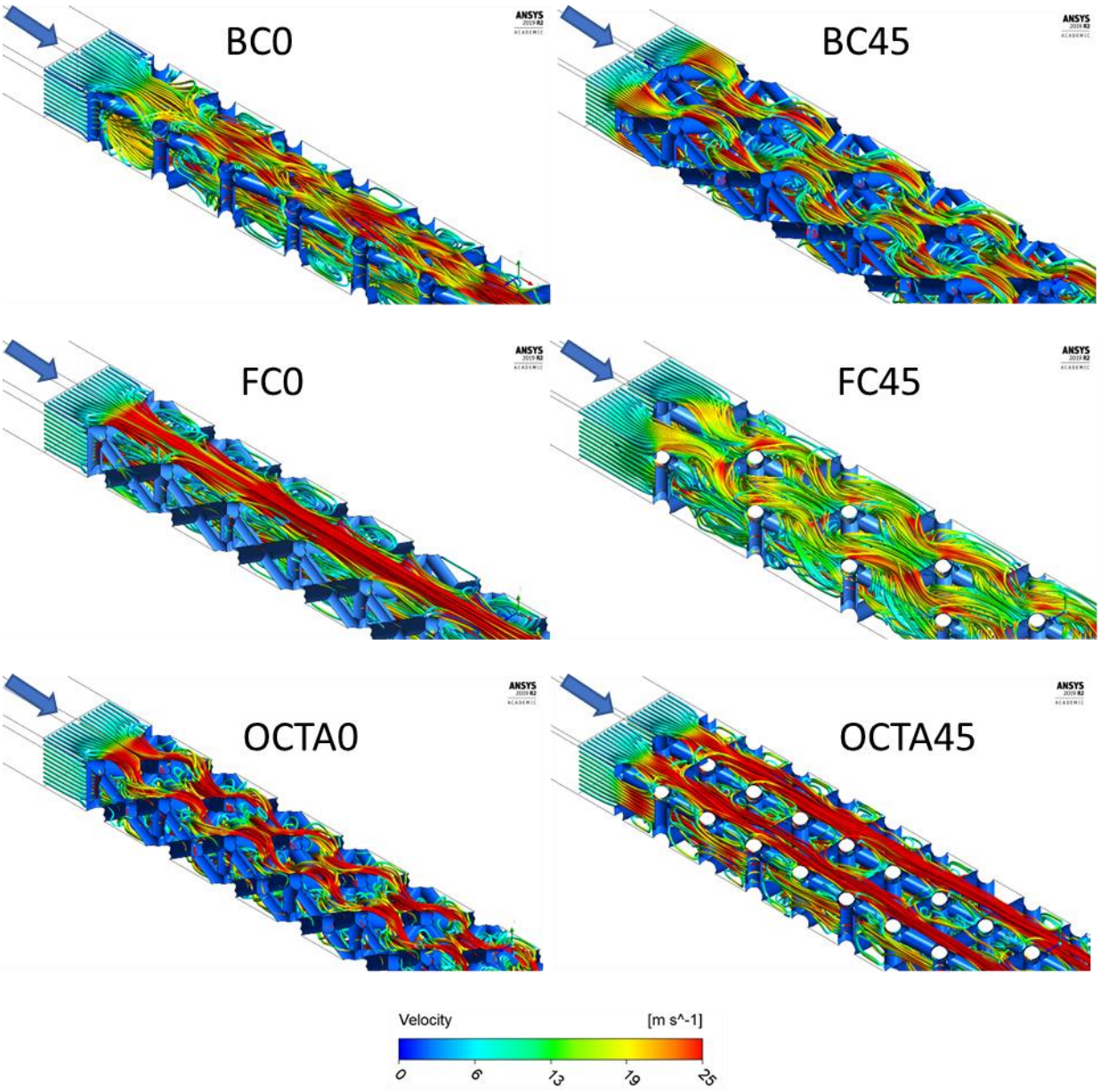

Figure 3.17 Velocity streamlines highlighting the sub-channel flow in BC, FC, and OCTA lattices with 0° and 45° orientations

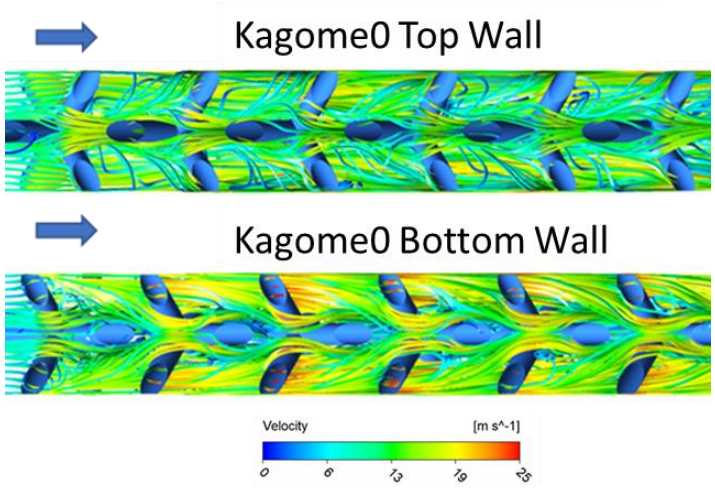

Figure 3.18 For Kagome0, the top plate experienced a slower flow compared to bottom plate

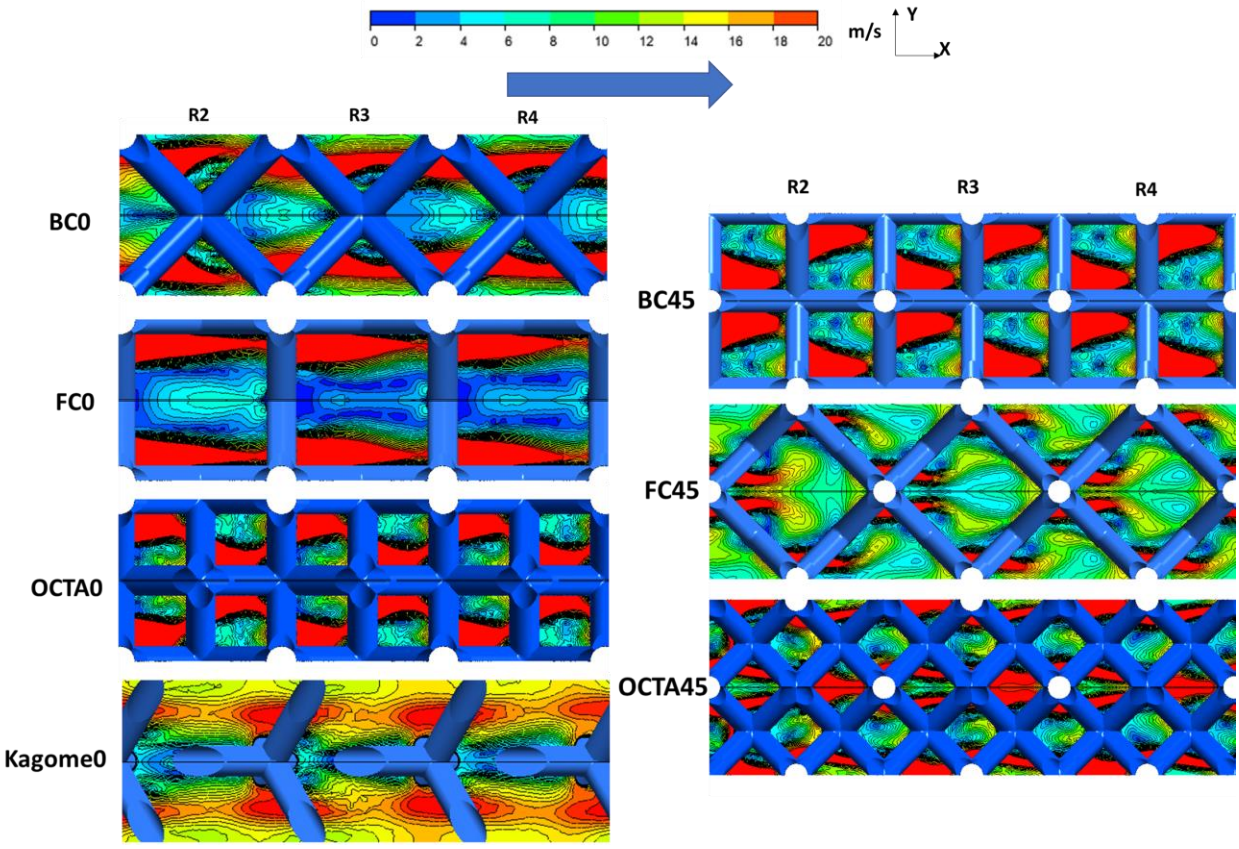

Figure 3.19 Comparison of velocity field at the horizontal plane at H/2 for rows 2-4

Figure 3.20 shows the distribution of the turbulence kinetic energy (TKE) within the lattice cooling channels on a plane 0.1H from the end wall. The yellow circles indicate the nodes which were submerged in the flow while the dashed line represents the outline of the unit cell. The TKE values were observed to be highest in the wake regions of both the nodes as well as the vertices. The distribution of h on a section of the end wall in the downstream region in also shown in a box. In each case, the location of the peak in h overlapped with that in near wall TKE.

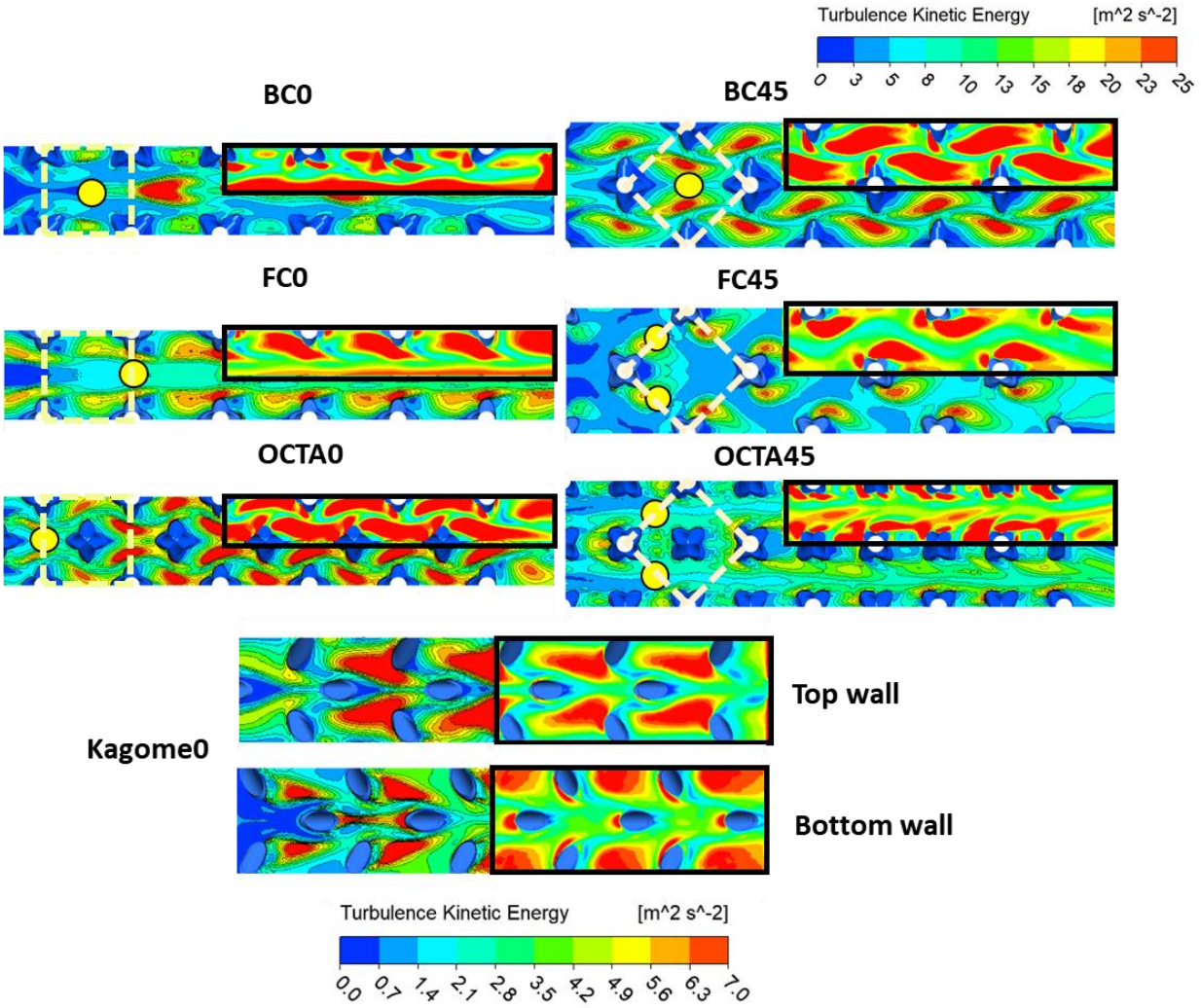

Figure 3.20 Distribution of TKE on a xy plane 0.1H below the end wall, and the predicted h (inset)

In summary, in this chapter, a high-resolution distribution of the local h on the channel end walls was obtained for four types of lattice geometries at two values of $\theta = 0°$ and 45°. Each lattice type had a unique distribution of end wall h, which was determined by the underlying arrangement of the ligaments within the bulk flow and the vertices on the end wall. It was shown that similar to the overall conjugate heat transfer, the end wall heat transfer was also dependent on both the topology and the orientation of the lattice in the flow. However, it was shown that the effect was confined to change in the distribution of local h on the walls, while the overall averaged heat transfer largely remained similar. Unique and complex patterns in h were identified for each of the rotated and non-rotated lattices which highlighted the possibility of tailoring the end wall heat transfer based on application. These results were contrasted with that of a standard pin fin bank under similar flow conditions. Finally, numerical simulations were conducted to show the formation of unique sub-channels in these geometries that confined the high-speed flow in certain areas of the channel. The shape of these subchannels near the end walls was shown to be guided primarily by the inline or staggered arrangement of the vertices. In addition, the end wall heat transfer was shown to closely follow the near wall TKE distribution.

4.0 Novel Integrated Lattice-Transpiration Cooling Architecture

In this chapter, a novel integrated lattice-transpiration cooling architecture (Fig. 4.1) has been proposed and characterized for its heat transfer performance. These architectures were realized by marrying transpiration cooling, which is an external cooling technology, with the developed internal cooling lattice geometries. There were two primary motivations behind such an integration. Firstly, transpiration cooling consists of perforated wall that forms the hot side wall of the cooling channel. As a result, these designs are not as strong as a fully dense wall or film cooling walls [61,62]. In practical application within an airfoil, transpiration walls would require a backend support structure to maintain the desired mechanical strength in high temperature, high pressure operational environment. Lattices are well known for providing such structural rigidity and strength. Secondly, transpiration pores are highly susceptible to blocking while the gas turbine engine is in operation. Such blockage will result in the loss of film protection on the outside of the turbine walls [124] and could lead to the premature failure of the airfoil. With their high heat transfer, as shown in Chapter 2 and 3, lattices could help mitigate the loss in cooling due to such blockages. Finally, compared to pin fins, which have been proposed as backend geometry in integrated effusion cooling architectures, lattices have a distinct advantage of providing very high surface area relative to their footprint area. This is highly desirable because a high footprint area, such as in pin fins, would cause large blockage of the transpiration pores and will prove detrimental to the overall cooling performance. Thus, lattices are uniquely suitable for such backend cooling applications.

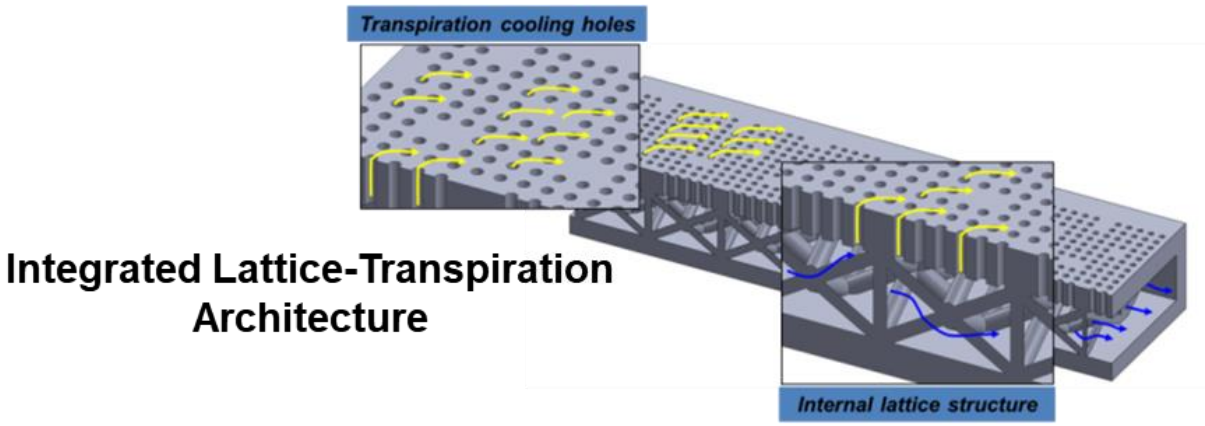

Figure 4.1 Proposed integrated lattice-transpiration cooling architecture

4.1 Geometries

The integrated design was achieved by laying two rows of a given lattice design on the back side of a 0.3 mm and 3D pitch transpiration coupon adopted from [62,63]. Four integrated lattice-transpiration test coupons were prepared corresponding to the four lattice unit cells. The lattices were selected as the 0° orientation with 0.75 mm ligament diameter for each type. These integrated coupons are shown in Fig. 4.2 and were fabricated by DMLS of IN718 powder in EOS M290 system [95], similar to the samples in conjugate tests. A closeup of the fabricated coupon has been shown in Fig. 4.3. The dimensions of the lattice unit cells were constant across all the cases (l × b × h of 4 mm × 4 mm × 2.5 mm). Apart from these coupons, another set of coupons were prepared which did not have the backend lattice while they preserved the lattice footprint on the transpiration surface. The transpiration phenomenon is very sensitive to the blockage of the transpiration holes, thus, it was important to measure the effect of the blocking due to the lattice footprints on the cooling performance.

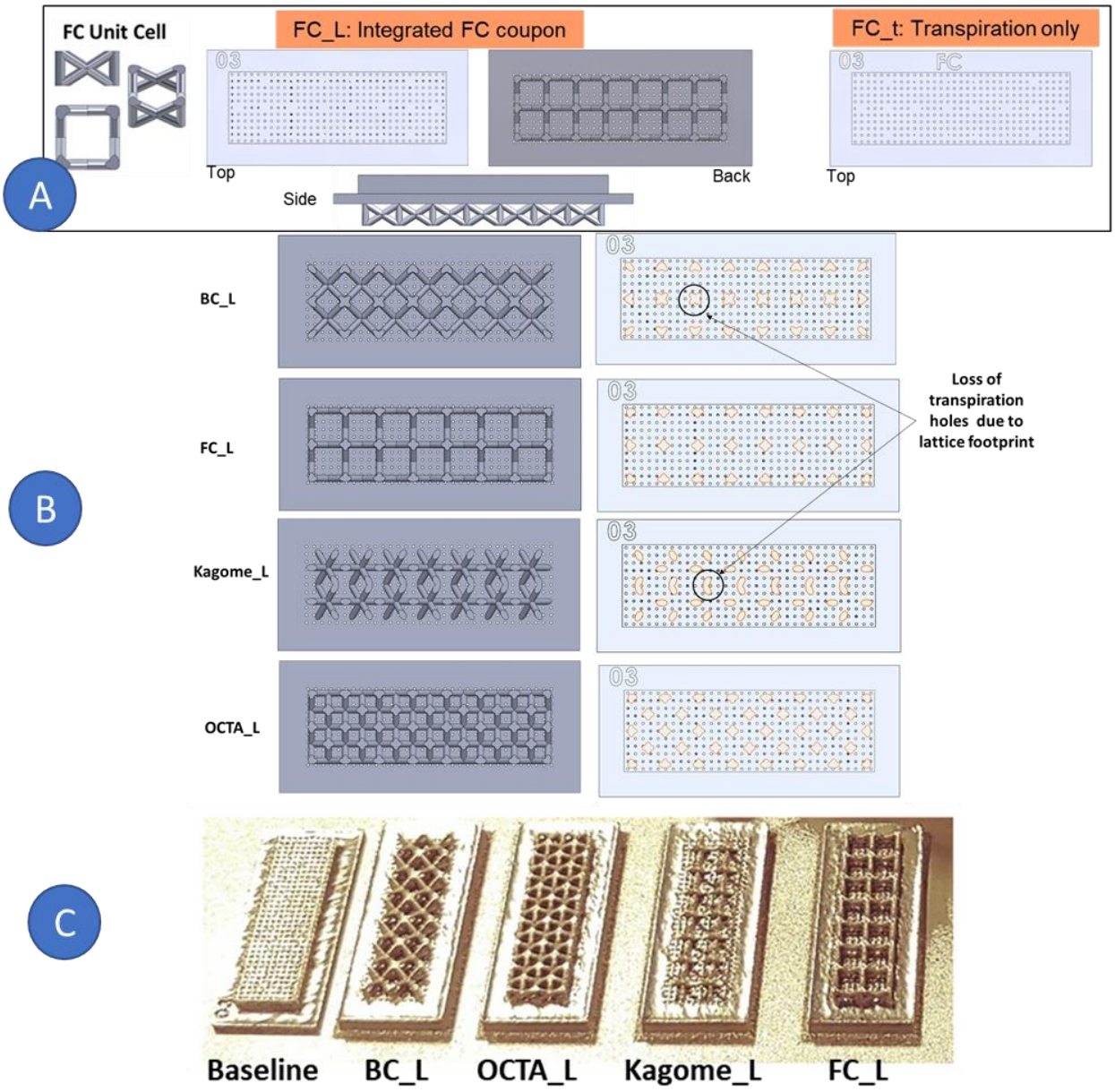

Figure 4.2 (A) Example of the integrated architecture shown for FC lattice, (B) transpiration cooling holes blocked by lattice footprint, and (C) integrated cooling test coupons fabricated using DMLS and IN718

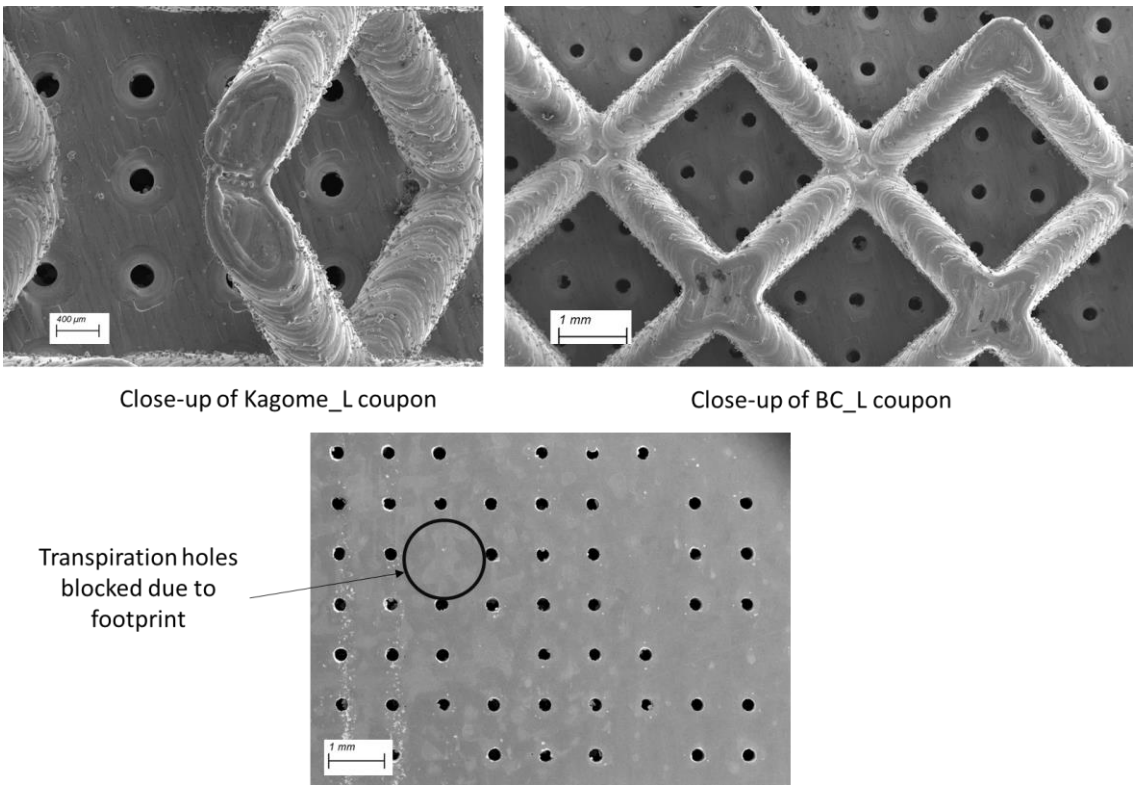

Figure 4.3 Close-up of Kagome_L and BC_L coupons showing the roughness on the ligaments (above), and holes blocked by lattice footprint in AM coupon (below)

There were two coolant feeding mechanism possible for the integrated architecture: plenum fed (PL-fed) and crossflow fed (CF-fed). In case of the PL-fed configuration, the coolant was introduced perpendicular to the target wall. As such, the coolant first flowed over the lattice and then through the transpiration holes to form the outer protective film coverage. In contrast, for the CF-fed configuration, the coolant flowed parallel to the target wall. There was an additional back wall located behind the lattice, forming a channel with the target wall with lattice embedded inside. The coolant was introduced from one end then flowed over the lattice and simultaneously leaked through the transpiration holes to form the outer film coverage. As a result of continuous loss of coolant through the transpiration wall, the coolant flow rate over the lattice diminished in the downstream direction. At the same time, the flow through the transpiration also changed over the

length of the channel, diminishing in the downstream direction due to the lower pressure difference between the internal and external flow. Thus, it was expected that the cooling effectiveness on the external end wall in CF-fed configuration would be different compared to that in the PF-fed configuration. The comparison between the coolant flow for both the plenum-fed and the crossflow-fed configurations is shown in Fig. 4.4.

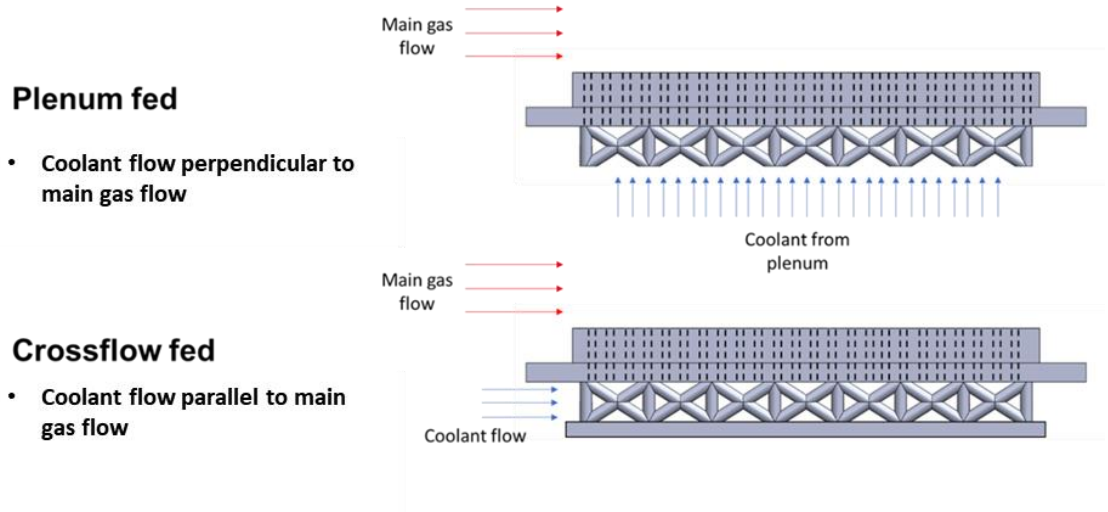

Figure 4.4 Schematic comparing the coolant flow in plenum-fed and crossflow-fed configurations

4.2 Experimental Technique and Methodology

The conjugate heat transfer and the TLC tests provided details about the internal heat transfer in a channel that contained lattice geometry embedded inside. However, in order to obtain the thermal performance of the integrated lattice-transpiration coupons, the overall cooling effectiveness, φ, needed to be evaluated, which is defined as

$$\varphi = \frac{T_g - T_w}{T_g - T_c} \qquad (4.1)$$

where, T_g is the main gas temperature, T_w is the external wall temperature on the hot side, and T_c is the reference coolant temperature. Thus, the tests for these coupons consisted of measurement of the temperature distribution on the external wall exposed to a hot main gas flow. This distribution was captured using infrared (IR) thermometry. The overall uncertainty in the measurement of φ was determined to range from 4.4% to 10.3% based on the method proposed in [105].

In order to minimize the effect of material and surface finish, the external surface of the test coupons was first polished and then sprayed painted using a matt black paint of emissivity ~0.9. A calibration curve was generated by first painting a surface using this black paint and embedding a thermocouple. The surface was heated using a hot plate to reach a steady state value and then the temperature reading from both the thermocouple and the IR camera were recorded. The step was repeated for a range of temperature expected during the experiments. A polynomial curve was then fitted to the data in order to obtain the correlation between the measurement of the IR camera and the reference thermocouple. This curve was used to correct the reading of the IR camera at each pixel of the recorded IR image.

The test setup (Fig. 4.5) was similar to that used by [62,63] with appropriate modifications to accommodate the integrated coupons and achieve the two types of coolant flow schemes. These tests required two gas streams: 1) an external main gas flow at elevated temperature, and 2) a coolant flow. The main gas flow was obtained using a wind tunnel test rig using a blower. The high-pressure air from the blower was passed through an inline heater to obtain the desired mainstream temperature. This heated air was then passed through a flow development section and introduced in the main channel where the test sections were located. The mainstream temperature

and flow rate was maintained constant throughout the test process and the coolant flow rate was varied to obtain three blowing ratios, defined as

$$M = \frac{\rho_c U_c}{\rho_g U_g} \qquad (4.2)$$

where, $\rho_c$is the coolant density, ρ_g is the main gas density, U_c is the mean velocity of coolant through the transpiration holes, and U_g is the mean velocity of the main gas flow, determined using a pitot tube. Separate test plate assemblies were developed for the PL-fed and the CF-fed coolant flow configurations and are discussed in the next section.

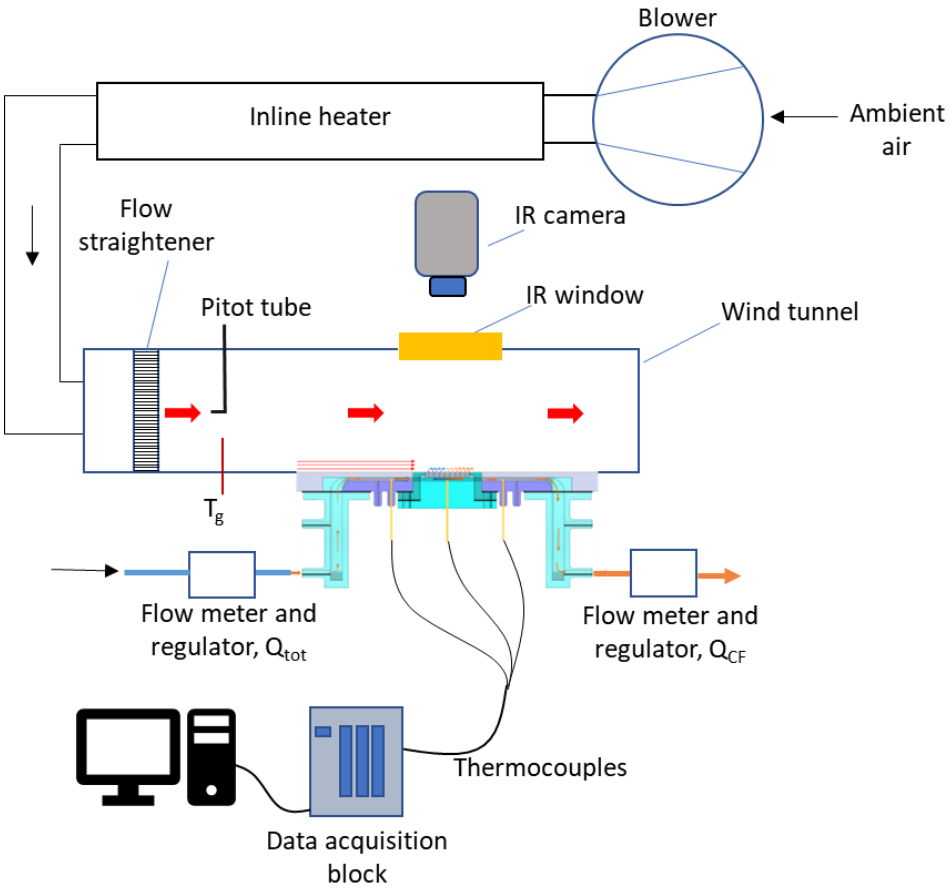

Figure 4.5 Overview of the wind tunnel with the test plate assembly installed

4.2.1 Test Plate for The Plenum-Fed Configuration

This setup was similar to that used by [62,63] to test their transpiration cooling designs. The PL-fed configuration consisted of a plenum that received the compressed coolant air from the flow conditioning section. This coolant air first flowed over the embedded lattice structures which were exposed in the plenum, and then through the transpiration holes to form the external protective film. The temperature of the coolant air in the plenum, T_{plenum}, was used as the reference temperature to obtain the overall effectiveness. The plenum and coupon assembly is shown in Fig. 4.6.

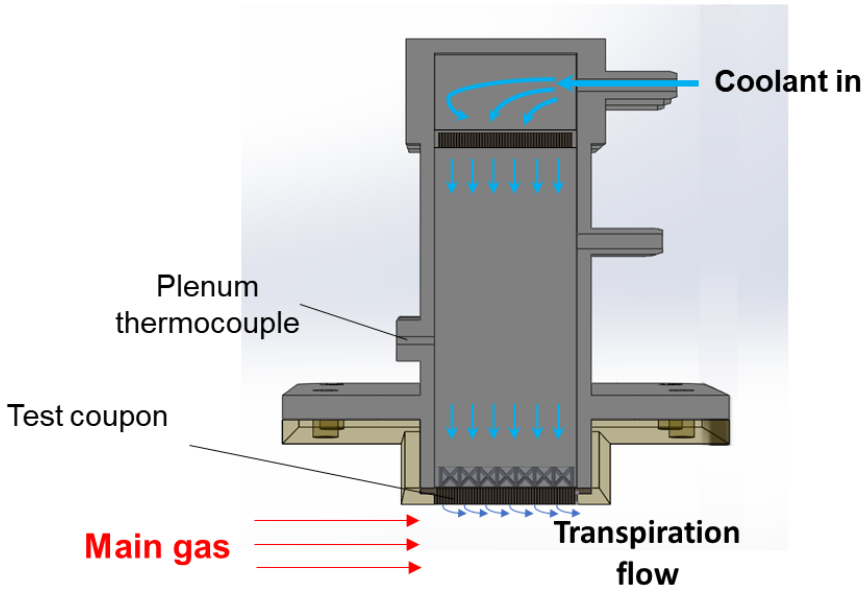

Figure 4.6 Plenum and test coupon assembly for PL-Fed configuration

4.2.2 Test Plate for Crossflow-Fed Configuration

In CF-fed tests, the coolant entered into the inlet plenum with a total flow rate of Q_{tot}. The coolant then moved through a flow development channel before entering the test channel

containing the coupon. Within the test channel, the coolant flowed over the backend lattice and simultaneously leaked through the transpiration holes at a flow rate of Q_{tran}. By controlling a flow regulator on the outlet side, either all the coolant could be forced through the transpiration holes, or only partial coolant could be allowed through the transpiration holes by allowing some coolant to escape through the outlet plenum with a rate of Q_{CF}. Thus, the total flow rate can be given as

$$Q_{tot} = Q_{tran} + Q_{CF} \quad (4.3)$$

While the temperature distribution on the external wall was measured using an IR camera, there were multiple thermocouples installed along each of the internal flow channel to measure the coolant temperature at the inlet, middle, and outlet of the test channel. During the current tests, the middle thermocouple, T_{plenum}, was used to obtain the overall cooling effectiveness. The coupons used for these tests were same as those used for the PF-fed tests. This test plate assembly was mounted on one of the walls of the wind tunnel used for testing the previous coupons. The overall schematic of the rig is shown in Fig. 4.7.

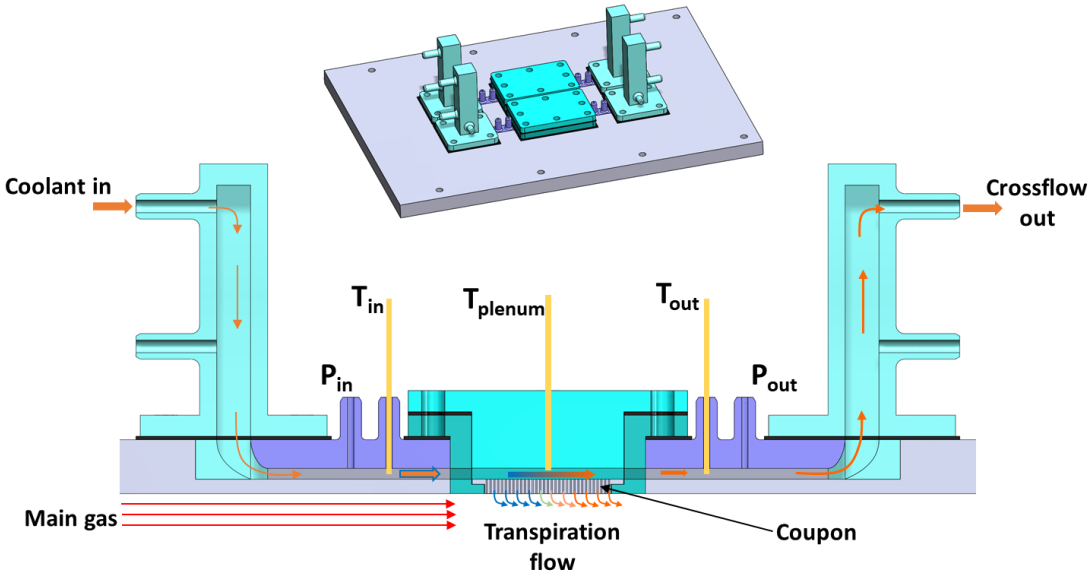

Figure 4.7 Schematic of the crossflow-fed test plate assembly and the tested coupons

The PL-fed tests were performed similar to the transpiration cooling tests done in [62,63]. The coupons were attached to the plenum such that the transpiration wall was facing the main hot gas while the coolant flowed perpendicular to the transpiration wall. During the tests, the coolant flow rate was metered and varied using flow regulators in order to achieve a range of blowing ratio from M = 0.1 to 0.5. For each blowing ratio, the coupon temperature was allowed to reach a steady state following which the temperature of the coolant, main gas, and the transpiration wall, along with the coolant flow rates and pressure of pitot tube in main flow were recorded. This process was repeated for all values of M.

The test procedure for the CF-fed coupons was different. There were two sets of tests performed for each coupon. The first set of tests was performed under a zero-crossflow condition, wherein the Q_{CF} was set as zero. The next set of tests consisted of a variable Q_{CF} in order to observe the effect of crossflow on the performance of the coupons. Similar to the PF-fed tests, the coupons were allowed to reach a steady state before the readings from the thermocouples, IR camera, pitot tube, and flow meters were recorded. The test matrix for the two types of flow configurations is shown in Table 4.1.

Table 4.1 Summary of blowing ratio and crossflow rate for tested geometries

Coupon	Coolant flow configuration	M	CF	
			Fixed Q_{CF}, varying Q_{tot} (Q_{CF}/Q_{tot})	Fixed Q_{tot}, varying Q_{CF} (Q_{CF}/Q_{tot})
Baseline transpiration, BC_t, BC_L, FC_t, Kagome_t, Kagome_L	PL-fed	0.125	-	-
		0.25	-	-
		0.5	-	-
	CF-fed	0.125	0	-
		0.25	0	-
		0.5	0	-
		0.25	0.29	-
		0.50	0.18	-
		0.37	-	0.21
		0.34	-	0.27
		0.31	-	0.33
		0.28	-	0.39
FC_L	PL-fed	0.125	-	-
		0.25	-	-
		0.5	-	-
	CF-fed	0.125	0	-
		0.25	0	-
		0.5	0	-
		0.25	0.29	-
		0.50	0.18	-
		0.37	-	0.21
		0.34	-	0.27
		0.31	-	0.33
OCTA_t, OCTA_L	PL-fed	0.125	-	-
		0.25	-	-
		0.5	-	-
	CF-fed	0.125	0	-
		0.25	0	-
		0.5	0	-
		0.25	0.18	-
		0.50	0.29	-
		0.41	-	0.15
		0.39	-	0.21
		0.36	-	0.27
		0.34	-	0.30

4.3 Results and Discussions

4.3.1 Overall Cooling Effectiveness of Transpiration Only Coupons

Transpiration cooling depends on the effectiveness of the film being produced by the coolant leaking through perforate holes on the hot gas side of the end wall. A blockage in these holes could be detrimental to the overall performance of the transpiration design. Compared to the baseline transpiration coupon, some of the transpiration holes in the integrated design coupons were prominently blocked by the lattice footprint. In case of the BC and FC integrated coupons, the transpiration open area was ~6%-7% smaller than that in the baseline coupon. On the other hand, for OCTA and Kagome, the blockage was even higher and the open area was ~12% smaller than the baseline coupon. Thus, it was important to assess the effect of this blockage alone on the overall performance of the coupon before evaluating the coupons with integrated lattices.

While comparing the performance of these coupons, it was important to note that the reference temperature used to calculate φ was different in the two flow configurations. For the PL-fed coupons, the air temperature within the plenum served as T_{ref}, while for the CF-fed coupons, the temperature near the coolant inlet served as T_{ref}. The locations of corresponding thermocouples are shown in Fig. 4.6 and 4.7.

Fig. 4.8 shows the averaged overall cooling effectiveness on the transpiration wall of the PL-fed transpiration only coupons and baseline transpiration coupon. Within these coupons, φ followed the trend Baseline > FC_t > BC_t > OCTA_t ~ Kagome_t which coincided with inverse of the ratio between transpiration area in integrated coupons, $A_{integrated}$, to that in baseline, $A_{Baseline}$. For instance, in Kagome_t, ~11% blockage ratio led to ~12% decrease in overall cooling effectiveness at M = 0.5 compared to the Baseline transpiration coupon. In case of the CF-fed

transpiration only coupons (Fig. 4.9), the same trend was largely followed wherein the averaged φ was inversely proportional to the opening area ratio, except for the FC_t coupon. FC_t coupon showed the lowest effectiveness compared to the others in this flow configuration. This could largely be attributed to manufacturing artifacts resulting from the DMLS process, as have been highlighted in [102] for similar coupons.

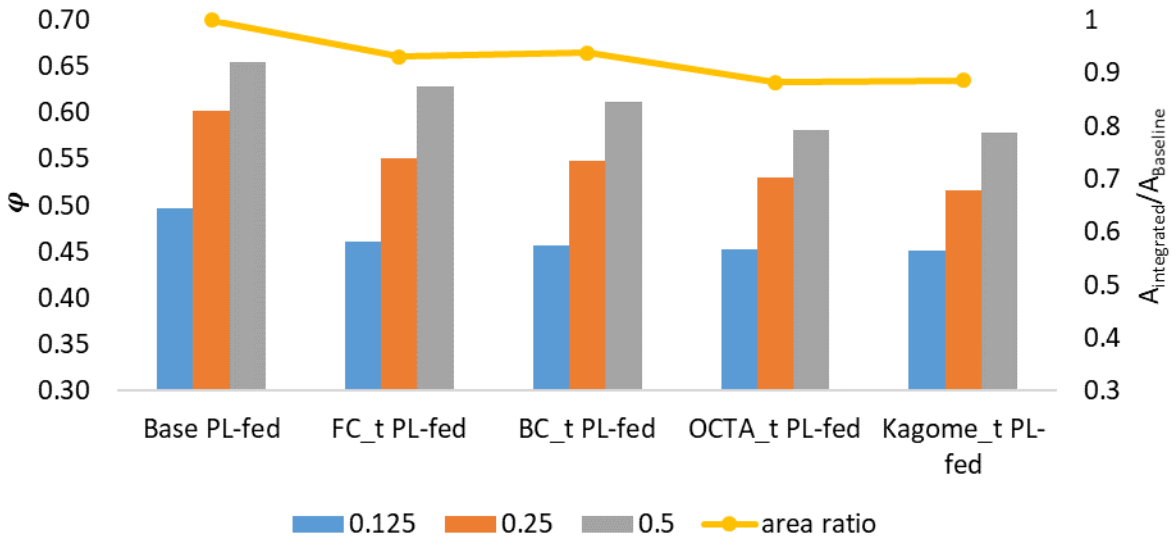

Figure 4.8 Comparison of overall cooling effectiveness between PL-fed transpiration only coupons

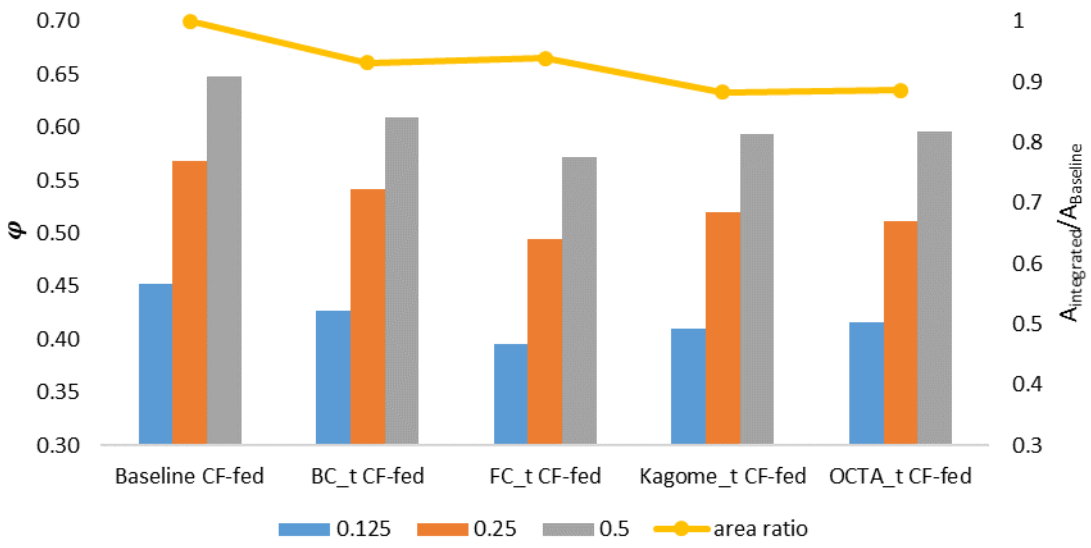

Figure 4.9 Comparison of overall cooling effectiveness between CF-fed transpiration only coupons

4.3.2 Overall Cooling Effectiveness of Integrated Lattice-Transpiration Coupons

4.3.2.1 PL-Fed Coupons

The local distribution of φ for the PL-fed integrated lattice-transpiration coupons for three blowing ratios has been shown in Fig. 4.10. For any given coupon, the value of φ increased in the downstream direction and reached maximum value near the middle of the coupon and then slightly diminished near the trailing edge. The low cooling effectiveness on the leading edge was because the film was not fully developed to provide adequate protection from the incoming hot main gas flow. In the downstream regions from the leading edge, the film thickness increased due to the addition of coolant from each successive rows of transpiration cooling holes. This thicker film coverage prevented the hot main gas flow from coming in contact with the coupon surface, resulting in higher value of local φ. As expected, the strength of cooling increased with an increase in M due to the coolant picking up additional heat from the walls of the transpiration holes which further lowered the coupon temperature.

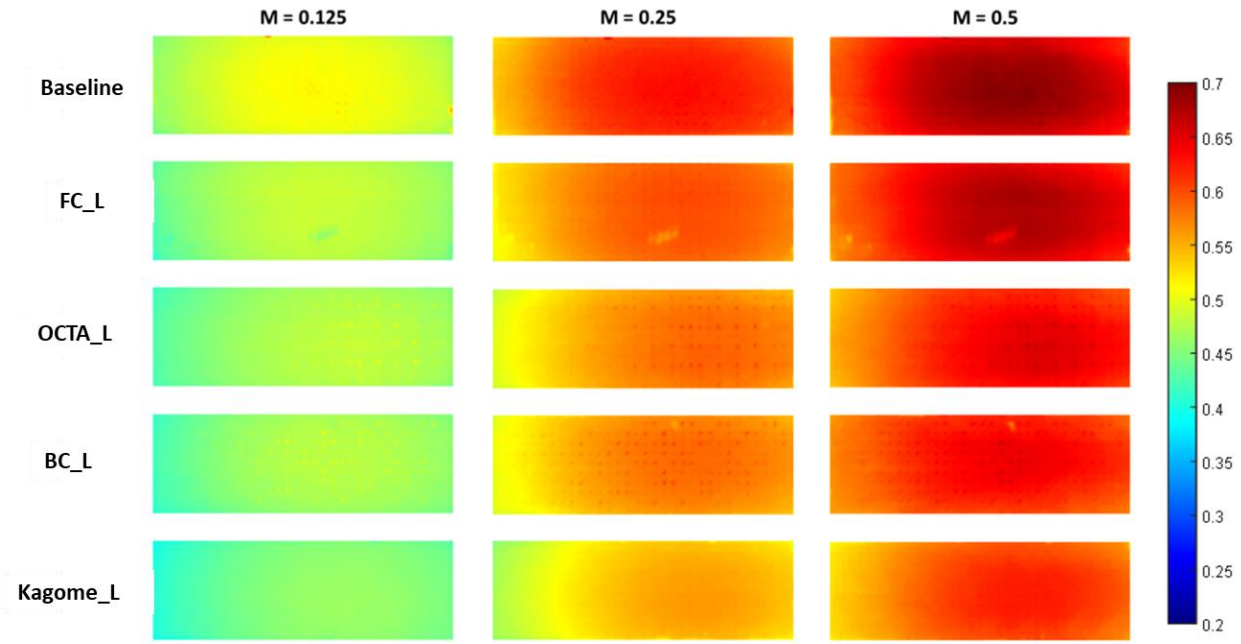

Figure 4.10 Local distribution of φ on integrated lattice-transpiration coupons in PL-fed configuration

The area averaged cooling effectiveness for these coupons have been shown in Fig. 4.11 and followed a trend where Baseline > FC_L > BC_L ~ OCT_L > Kagome_L. In order to eliminate the edge effects, only the central 5 rows of holes have been considered for evaluating the results. The higher performance in baseline coupon was due to the absence of any blockage of transpiration holes, maximizing the film coverage. In case of the integrated coupons, some of the transpiration holes were blocked by the lattice footprint, $A_{footprint}$, thus, the film coverage was expected to be lower. However, the backend lattice also provided additional surface area, $A_{lattice}$, for heat transfer from the end wall into the coolant which was expected to improve the overall cooling effectiveness. Fig. 4.11 also showed the area averaged φ for the transpiration only coupons for comparison. In all cases, addition of the backend lattice led to a ~2%-~6% improvement in the averaged φ for M = 0.25 and 0.5. The OCTA_L integrated coupon with the highest $A_{lattice}$ showed the most significant increase (~ 6% increase at M = 0.25 and 0.5) of φ compared to the OCTA_t coupon.

In case of the remaining coupons, the improvement was very similar, about 2% - 3% for the tested M. Therefore, the presence of lattices on the coolant side compensated part of the performance loss caused by the footprint blocking the transpiration holes.

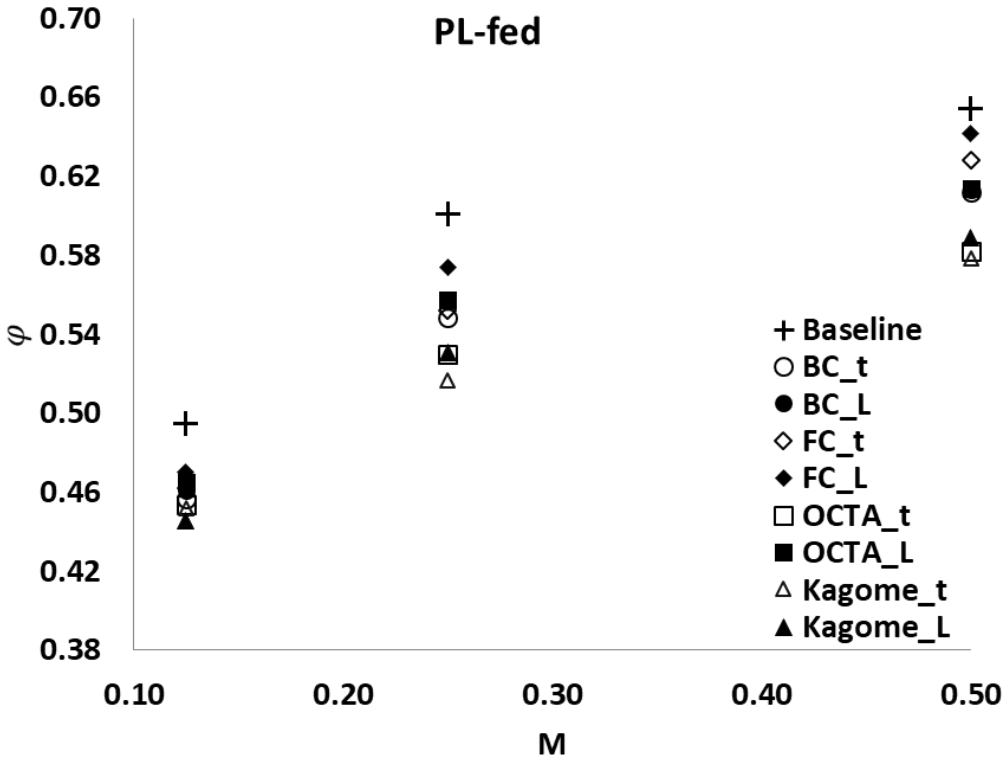

Figure 4.11 Comparison between overall cooling effectiveness between integrated cooling coupons and the corresponding transpiration only coupons

4.3.2.2 CF-Fed Coupons

As mentioned in Table 4.1, two cases were tested in order to assess the impact of the crossflow on the φ of coupons with integrated cooling architecture. The first case consisted of tests with zero crossflow, i.e. $Q_{CF} = 0$, while the second case consisted of a fixed crossflow rate of $Q_{CF}/Q_{tot} = 0.18$ and 0.29. For CF-fed coupons, it was more convenient to discuss the results in terms of the streamwise and spanwise averaged φ, as shown in Fig. 4.12, for both these flow cases.

4.3.2.2.1 Fixed Q_{CF} and Varying Q_{tot}

For a given M, when the Q_{CF} was maintained as 0, the upstream regions of the integrated coupons showed a higher spanwise averaged φ, which remained somewhat constant until x/L = 0.4 – 0.6, and then decreased in the downstream direction. The presence of the backend lattice in these integrated coupons created a much higher flow resistance for the coolant entering the channel. This resulted in a streamwise decreasing pressure difference between the channel and the main flow. As a result, the flow of coolant from the upstream transpiration holes was stronger due to the larger pressure difference between the coolant and main gas flow, forming strong coolant jets. These strong jets penetrated deeper into the main gas flow, causing film lift-off and diminished local film cooling in the upstream regions. Additionally, the increased mixing and turbulence due to interaction of the upstream transpiration flow with the main flow caused further deterioration of the upstream film coverage, similar to the PL-fed cases. At the same time, these jets also provided a shielding effect for the immediate downstream regions by diverting the hot gas flow away from the coupons. The lattice in these coupons also acted as extended heat transfer surface and the fast, low-temperature coolant entering the channel provided additional heat removal from the upstream lattices and transpiration holes. As a result of these effects, the upstream region of the transpiration plate had lower temperature and higher φ. The crossflow weakened in the downstream direction due to the loss of the coolant from transpiration holes, thus, decreasing the heat transfer from the lattices. Moreover, the lower coolant flow meant that the film coverage also decreased, therefore leading to a decreasing φ along the remaining transpiration surface.

When Q_{CF} was increased from 0 to a constant value, an increase in φ was observed for all coupons and at all values of M. Under this flow condition, the Q_{tot} at any given M was higher than

that in the corresponding case with Q_{CF} = 0. As shown in Fig. 4.12, the spanwise averaged φ improved along the complete length of the integrated coupons. The reason for this observed augmentation in φ could be attributed to the increased heat transfer from the backend lattices. As shown in the Chapter 2, the averaged Nu increased with an increase in the coolant flow rate in channels containing lattice geometries, which was the case in CF-fed configuration. The crossflow to total flow rate ratio, Q_{CF}/Q_{tot} was 0.29 and 0.18 for M = 0.25 and 0.5, respectively. Thus, M = 0.25 had a greater increase in φ compared to M = 0.5.

To highlight the impact of the backend lattices in CF-fed configuration, Fig. 4.12 also shows the spanwise averaged φ for transpiration only coupons, BC_t, FC_t, OCTA_t, and Kagome_t. In these coupons, the improvement in performance with non-zero crossflow was observed mainly in the downstream half of the coupons. The increased crossflow meant that the coolant carried larger streamwise momentum. In addition, the total flow rate was also higher at any given M. This meant that the downstream transpiration holes received more coolant, leading to better film coverage and local cooling. As expected, the trends in the transpiration only coupons were very similar to that observed for the Baseline transpiration coupon, shown in Fig. 4.13.

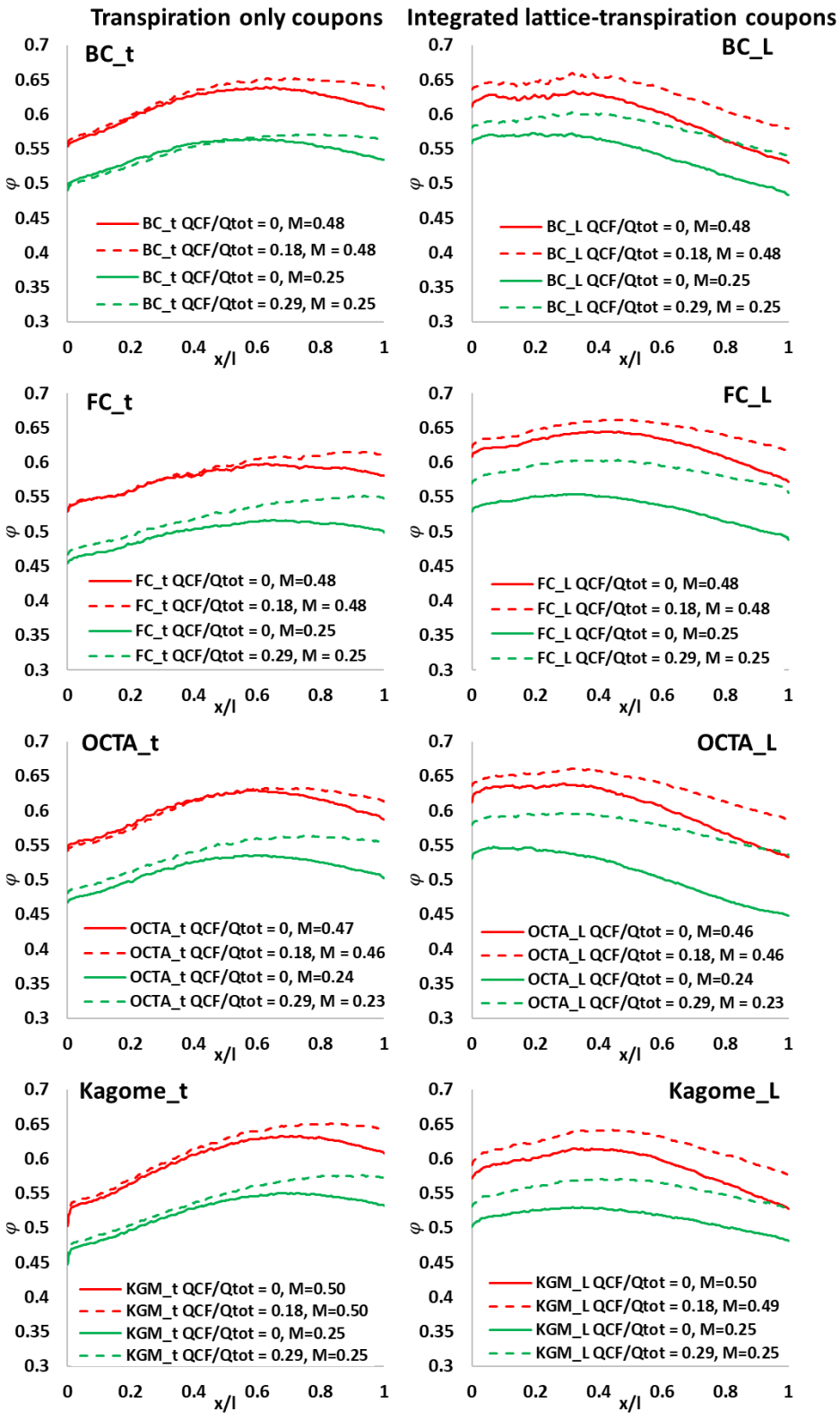

Figure 4.12 Spanwise averaged effectiveness, φ, for the tested integrated coupons

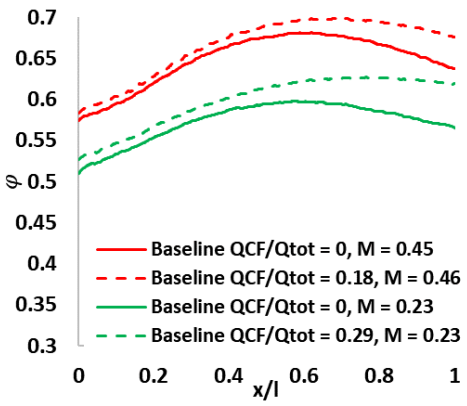

Figure 4.13 Spanwise averaged overall effectiveness, φ, for the tested baseline coupon

The overall averaged φ for these tests have been shown in Fig. 4.14. In all cases, the performance increased with the introduction of crossflow (red symbols) at a given M. In general, the higher Q_{CF}/Q_{tot} at M = 0.25 led to a greater increase (7% to 13%) than at M = 0.5 (4% - 5%). In addition, the gain was highest in the integrated lattice coupons compared to the transpiration only coupons. Among the integrated lattice coupons, OCTA_L benefitted the most and BC_L the least from an increased crossflow.

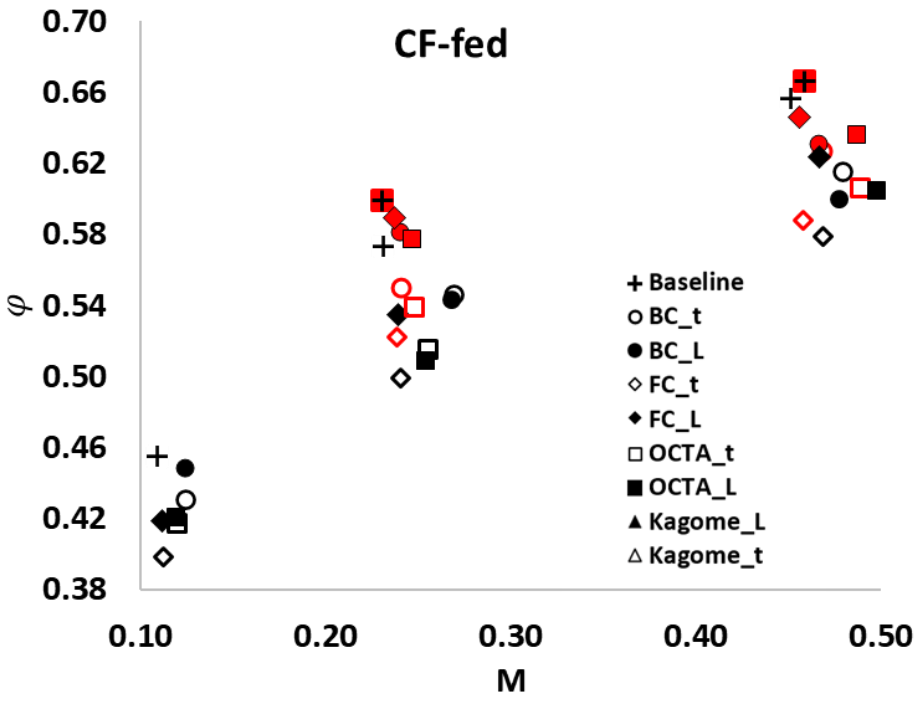

Figure 4.14 Overall cooling effectiveness for all the CF-fed integrated lattice coupons highlighting the impact of fixed crossflow with varying total flow

4.3.2.2.2 Fixed Q_{tot} and Varying Q_{CF}

The previous section discussed the performance of the integrated architecture under a fixed Q_{CF}. In this section, instead of Q_{CF}, the Q_{tot} was fixed and the Q_{CF} was gradually increased to measure the impact of varying crossflow on φ. The results are shown in Fig. 4.15. Under this flow condition, M value decreased with an increase in Q_{CF} because less and less coolant flowed through the transpiration holes. It was observed that the impact of increasing Q_{CF} at fixed Q_{tot}, was relatively low and the φ remained somewhat constant in the integrated coupons. On the other hand, in case of the transpiration only coupons, the overall averaged φ decreased with an increase in Q_{CF}, caused mainly due to the decrease in the transpiration cooling at lower M values. This trend indicated that the presence of an increasing crossflow on the backend lattices helped to mitigate the effects of loss of transpiration cooling. This is an important conclusion from the point of view

of real-world application of these cooling designs. Over the lifespan of an airfoil, the small cooling holes, such as in transpiration cooling, get blocked due to debris. As a result, external film protection decreases, leading to an increased risk of failure due to overheating of the airfoil. Such a condition is similar to the CF-fed configuration with constant Q_{tot} and varying Q_{CF}. By maintaining a relatively stable φ even with decreasing M, the proposed architecture could greatly reduce the harmful effects of blockage. This indicated that the backend lattices were capable of providing the required cooling when there is blockage of the transpiration holes. Fig. 4.16 compares all of the tested transpiration only and integrated lattice-transpiration coupons and summarizes the relative performance under the different flow configurations.

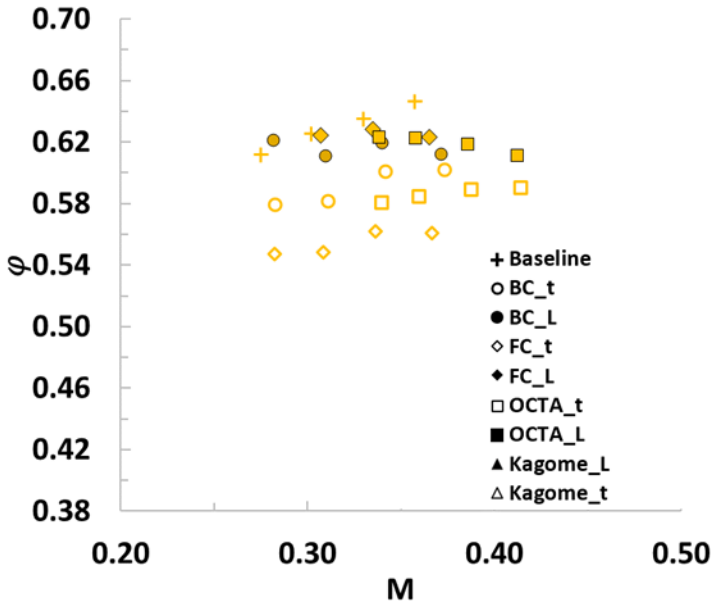

Figure 4.15 Overall cooling effectiveness for all the CF-fed integrated lattice coupons highlighting the impact of fixed total flow rate with varying crossflow

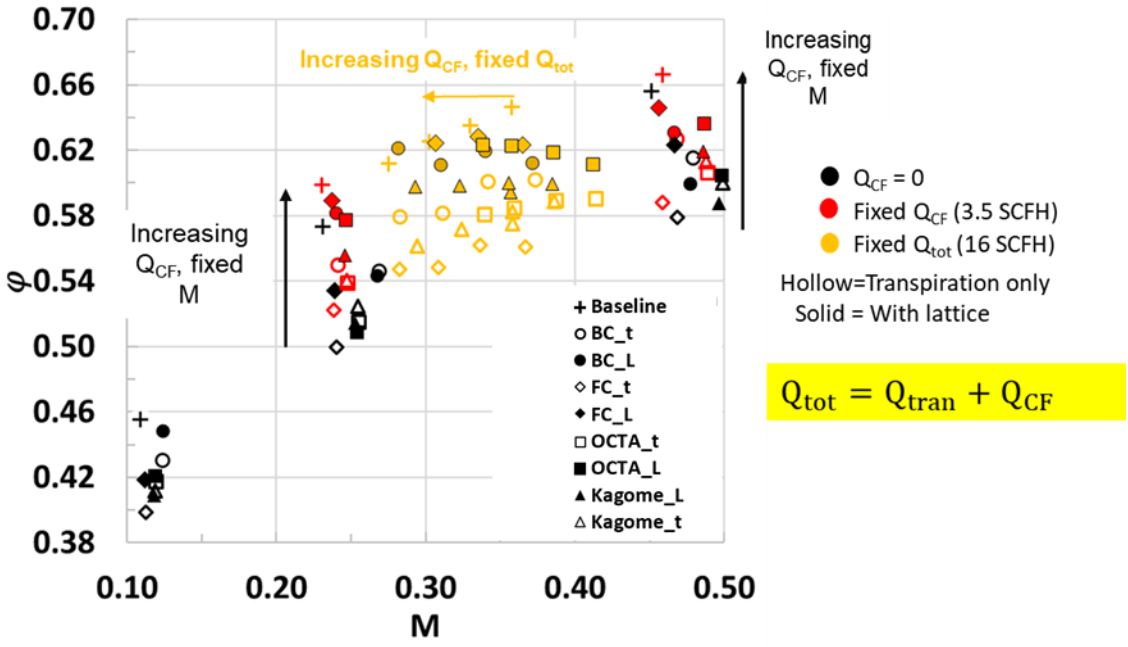

Figure 4.16 Comparison between the overall averaged φ for all the tested cases

In summary, the presented chapter introduced a novel integrated cooling architecture for the gas turbine airfoils. The architecture was realized by combining the advanced transpiration cooling on the external side and the developed lattice cooling on backend for internal cooling. These geometries were fabricated using IN718 and DMLS process and were investigated for their overall cooling effectiveness. The results showed that integration of lattices with the transpiration cooling provided cooling performance that matched with that of a traditional transpiration cooling system. The performance was slightly lower for these designs due to the obstruction of some of the transpiration holes owing to the lattice footprint on the end wall. Two types of coolant flow schemes were investigated and it was found that the CF-fed scheme is better among the two. This was because the crossflow present in this scheme extracted more heat from the backend lattices and allowed higher performance. It was also shown that the CF-fed scheme could mitigate any impact on the overall cooling effectiveness caused due to blockage of the transpiration pores

during operation, potentially elongating the life of the airfoils. Although the overall performance was smaller than that of the baseline transpiration coupon, it should be noted that transpiration alone is very difficult to achieve due to weak wall, and almost always will require a backend support structure. Here, it has been shown that lattices are a superior choice for such designs compared to the pin fins due to their extremely high surface to footprint area ratio.

5.0 Second Law Analysis and Topology Optimization for Lattice Geometries

In the presented chapter, second law analysis has been introduced to study the aerothermal performance of lattice geometries. As seen in the previous chapters, the augmentation of heat transfer rate was also followed by an increase in the pressure loss. This meant that a higher pumping power was required in order to maintain the desired coolant flow rate, compared to a smooth channel. Thus, it is desirable to perform optimization of such cooling geometries to reduce the accompanying pressure penalty. Using second law-based analysis, the relative strength of the heat transfer and viscous loss mechanisms can be directly compared in terms of local entropy production rates, as was discussed in Chapter 1. As a result, high loss, low heat transfer regions within the flow domain can be identified by tracking Bejan number, Be. The presented work showed that by using this definition of Be along with one of the proposed filtering criteria, regions where dissipative losses are more dominant than the heat transfer rates could be precisely isolated. Using the insight provided by this analysis, a topology optimization scheme has also been proposed and demonstrated here for the BC0 lattice.

5.1 Lattice Geometry and Numerical Setup for Second Law Analysis

The unit cell geometry selected for this study was the BC unit cell and the lattice selected was BC0, similar to that used in the TLC tests (Chapter 3). All the ligaments were of constant diameter, d = 3.75 mm, while the base of the unit cell, a, was 20 mm × 20 mm, and the height, H, was 12.5 mm. The fluid domain was similar to that used in the numerical analysis of Chapter 3,

except that the lattice was made thermally active by assigning a conductive solid domain. Similarly, only a quarter of the BC0 lattice geometry was used to leverage the symmetry and reduce computation time. The simulation was conducted for *Re* ranging from 1300 to 20,000. The boundary conditions used for this simulation were also adopted from those used in the TLC experiments for BC0 lattice. The fluid domain consisted of air and the flow was modeled as incompressible, while the solid domain was defined as aluminum with k = 237 W/m·K. Once again, the SST-kω was selected as the turbulence model because this has been shown to perform well for lattice geometries [30–32].

Although a grid independence study was performed in Chapter 3 for a similar numerical setup, it was repeated here again but with an additional mesh density. The previous simulations were meant to mainly predict the heat transfer coefficients on the end walls. However, the present simulations were performed to obtain the local entropy generation rates, hence, a grid independence study with respect to S_f and S_h quantities was warranted. Thus, four different mesh densities were considered: 4.8 M, 7.6 M, 13.6 M, and 18.6 M, to assess the grid independence of the solution. The simulations were performed for Re_{ch} = 11,800, and the values of overall Nu, pressure drop across the channel, and for the S_f and S_h were compared. The results of these comparison are shown in Table 5.1. As the mesh density increased from 4.8 M to 7.6 M, S_f and S_h changed by 6.4% and 2.5%, respectively. However, the variation in the value of S_f and S_h was 5.2% and 1.6%, respectively, for a 37% increase in mesh density from 13.6 M to 18.6 M. On the other hand, the pressure drop changed by < 0.3% and the area averaged heat transfer coefficient values changed by < 0.7%. As a result, it was assumed that a further refinement was not required, and 18.6 M was selected as the final mesh density.

Table 5.1 Result of grid independence study

Mesh density (Millions)	S_f (W/K)	S_h(W/K)	Pressure drop (Pa)	Area averaged h (W/m^2K)
4.8	0.0016	0.0026	1495	278
7.6	0.0017	0.0027	1501	277
13.6	0.0019	0.0028	1537	276
18.6	0.0020	0.0028	1541	274

The Bejan number, Be, compared the relative magnitude of $\dot{s}'''_h$ with the total entropy generation rate, $\dot{s}'''_{tot}$, at any given location within the flow field, and can range from 0 (typically within the bulk flow) to 1 (in the near-wall regions). From a heat transfer perspective, at any location, a high value of Be is desirable, since it would indicate that the flow work is primarily being utilized on strengthening the local heat transfer mechanisms. On the other hand, regions with low Be values utilize the flow work to primarily increase the viscous losses. This is the advantage of utilizing entropy-based analysis as it facilitates a direct comparison between the relative magnitude of the two mechanisms, both being represented in the same units of measurement [85,86,89,90]. The present work shows that it is possible to isolate fluid regions where one mechanism dominates the other by a defined threshold value. This threshold was defined by setting a specific value of Be, referred to as Be_{cutoff}, and all fluid regions that met the criterion of local Be $\leq Be_{cutoff}$, were filtered. The combined volume of the filtered fluid regions was referred to as V_{Be}. For example, defining Be_{cutoff} as 0.05 filtered out all flow locations having Be = 0 (regions with only viscous dissipation) to Be = 0.05 (regions where heat transfer contributed to only 5% of the total local entropy generation rate). When this step was repeated by progressively increasing the Be_{cutoff} from 0 to 1 with a defined step value, the selected fluid volume changed from highlighting the undesirable viscous-loss dominated regions (Be $\rightarrow$ 0) to highlighting the desirable heat transfer

dominated regions (Be → 1). An example is shown in Fig. 5.1 for two Be_{cutoff} values of 0.01 and 0.05, and three Re values of 5000, 11,800, and 20,000 for the BC0 lattice geometry. When the Be_{cutoff} was increased from 0.01 to 0.05 while keeping a constant Re, there was a corresponding increase in the volume of the selected fluid regions. In addition, the volume of selected fluid region also increased when the Re was increased from 5000 to 20,000 while keeping the Be_{cutoff} constant.

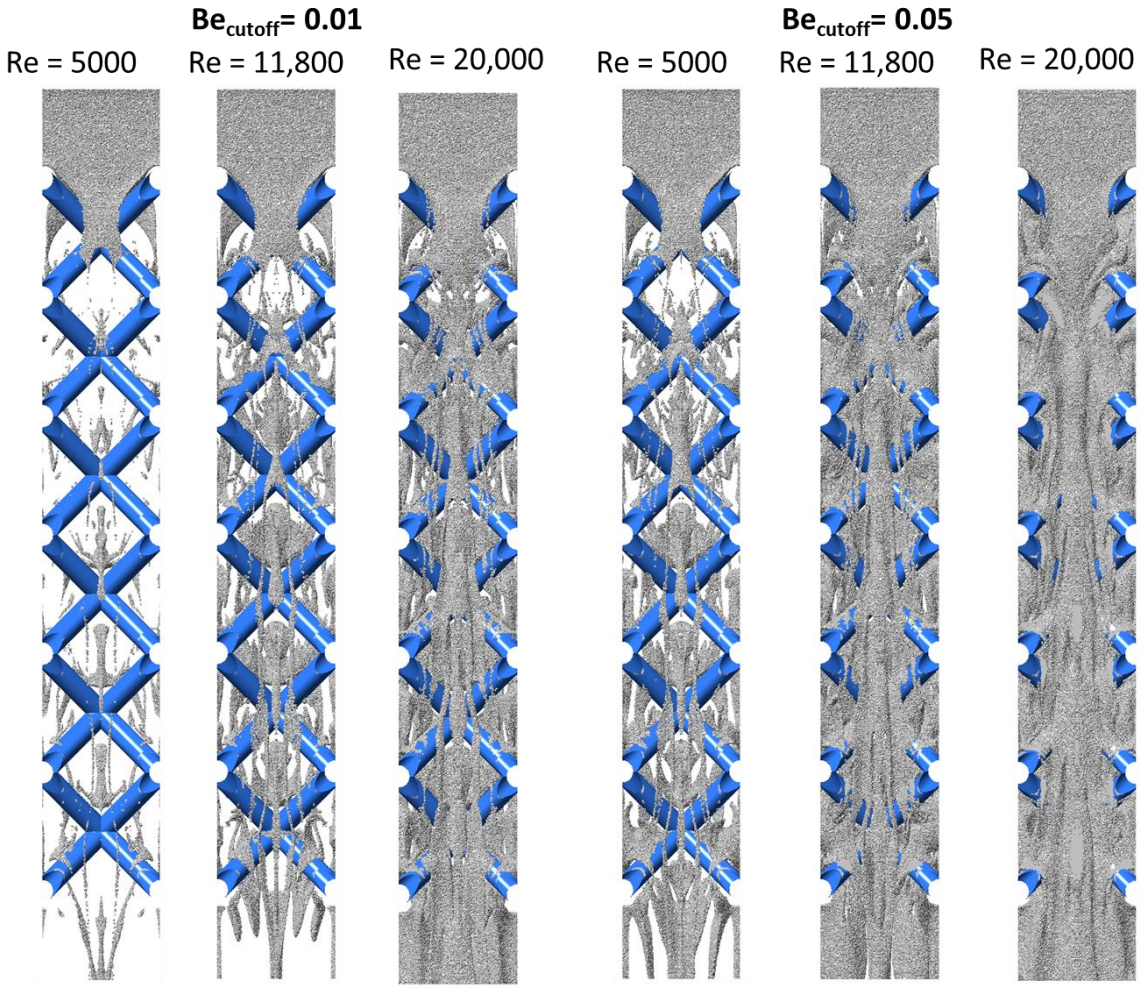

Figure 5.1 Comparison of filtered fluid volume, V_{Be}, by selecting two different Be_{cutoff} and varying Re

Three distinct zones were present within the simulated channel (Fig. 5.2). The first zone, Zone 1, extended from the inlet of the channel to the center of first z-ligament, the second zone, Zone 2, comprised of the lattice array, and the third zone, Zone 3, extended from the center of last

z-ligament to the channel exit. Within the first zone near the channel inlet, a large portion of the flow consisted of low Be regions because the thermal boundary layer was still developing there. Thus, most of the entropy generation occurred due to the viscous losses. When the flow entered row R1 in Zone 2, the local Be increased within the flow due to the increased heat transfer from the ligament surfaces. In addition, the development of complex flow structure promoted turbulence and mixing, leading to larger, better heat transfer within the bulk of the flow in R1. However, this intense mixing led to a more uniform temperature within the bulk flow in the downstream rows while the strong velocity gradients still prevailed, once again reducing the local Be values. Finally, the flow entered the Zone 3 after leaving the lattice array, and the local Be values again dropped due to further diminished temperature gradients and continued mixing within the wake.

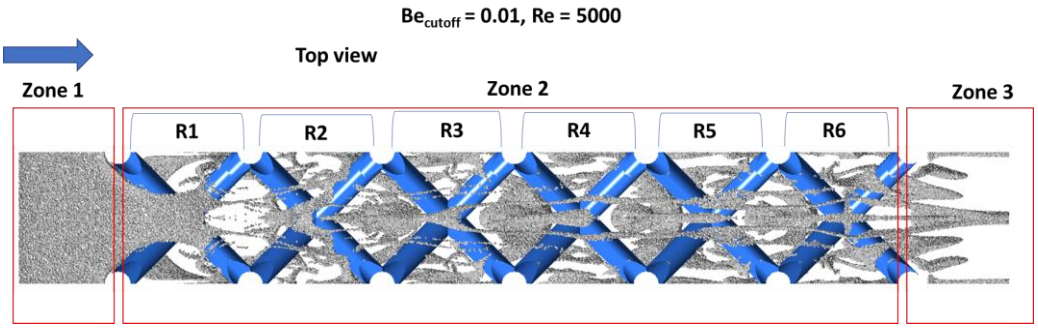

Figure 5.2 The three zones in the channel based on flow field (shown for Be_{cutoff} = 0.01 and *Re* = 5000)

In the above discussion, the application of Be_{cutoff} criterion alone to the whole channel resulted in V_{Be}, which consisted of all the fluid regions where $Be \leq Be_{cutoff}$. However, these regions were observed to be spread throughout the bulk flow. A more productive approach, from optimization point of view, would be to apply an additional filtering criterion to down-select fluid regions which could be associated with prominent flow field features, and in turn, to the topology of the lattice itself. Although such fluid regions would still be a subset of the V_{Be}, these regions would be better suitable for optimization through modification of shape or topology of the lattice.

Two such possible criteria, which can be combined with Be_{cutoff}, are: 1) based on streamwise velocity (u <= 0 m/s), and 2) based on the Q-criterion (Q > 0), which is the second invariant of the velocity gradient tensor and represents vortices within the flow [125]. For a given Be_{cutoff}, the fluid volume, V_{vel}, selected by using the velocity-based filtering, was located primarily in the wake regions of the ligaments and the body center nodes. On the other hand, fluid volume, V_Q, selected using the Q-criterion based filtering, was located within the vortices and highlighted a distinct connected fluid volume in the middle of the channel.

Figure 5.3 shows the three types of volumes V_{Be}, V_{vel}, and V_Q, resulting from applying the three filtering criteria, i.e. Be_{cutoff} alone, Be_{cutoff} + u ≤ 0 m/s, and Be_{cutoff} + Q > 0, respectively, for the case with Re = 11,800 and a Be_{cutoff} = 0.025. As can be observed from the figure, the fluid volume selected using the three criteria were markedly different. The velocity-based filtering eliminated Zone 1 present in V_{Be}, while the Q-criterion based filtering significantly reduced its size. Within the Zone 2, V_{vel} consisted of teardrop shaped regions located within the wake of the body center nodes, with small pockets of fluid volume located in the wake of the vertices. A part of both these wake regions were also present in V_Q, however, there were distinctly connected regions passing over the body center nodes located within local vortical structures (Fig. 5.4). Interestingly, the regions in V_{vel} formed only a subset of the actual wake flow regions (u < 0 m/s, shown in Fig. 5.4) indicating that some of the wake flow was responsible for high heat transfer rates. Similarly, regions in V_Q also consisted of only a portion of the total vortex flow, showing that some of the vortical flow helped enhance the heat transfer. Thus, using a filtering criterion not only helped in precisely isolating flow field dominated by viscous losses, but also can help associate a performance index to the various flow structures, showing the advantage of the proposed approach. Both V_{vel} and V_Q increased within the first 2-3 rows, showing that viscous

losses kept getting relatively stronger in the first few rows compared to heat transfer. This indicated that the upstream rows had a better thermal performance compared to the downstream rows.

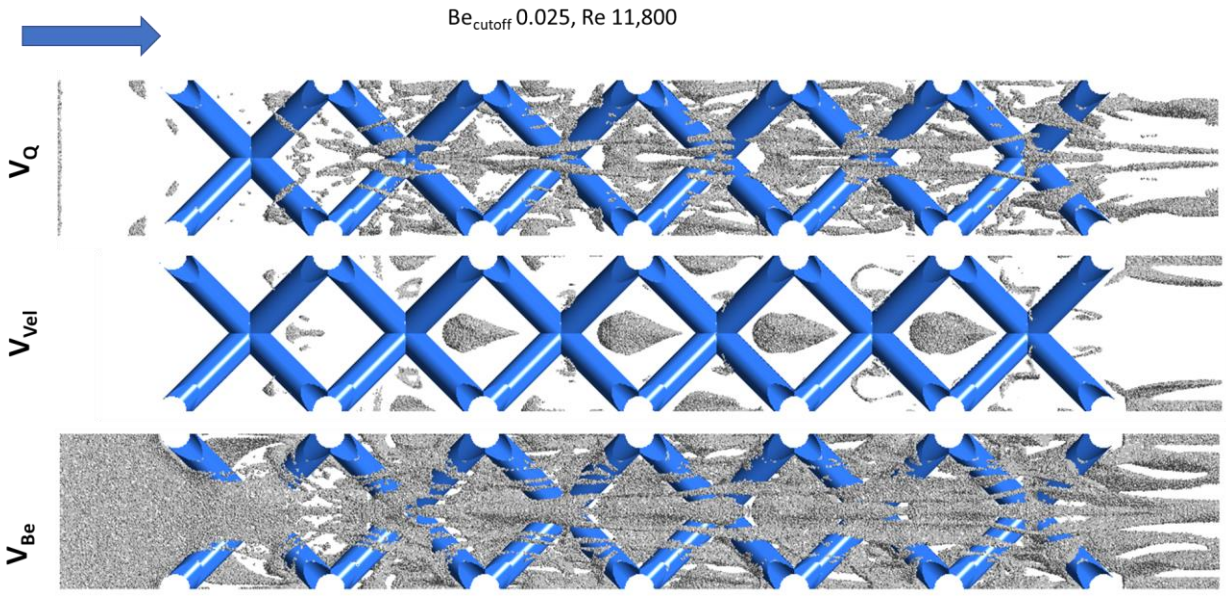

Figure 5.3 Effect of the filtering criterion on selection of fluid regions for Re = 11,800 and Be_{cutoff} = 0.025

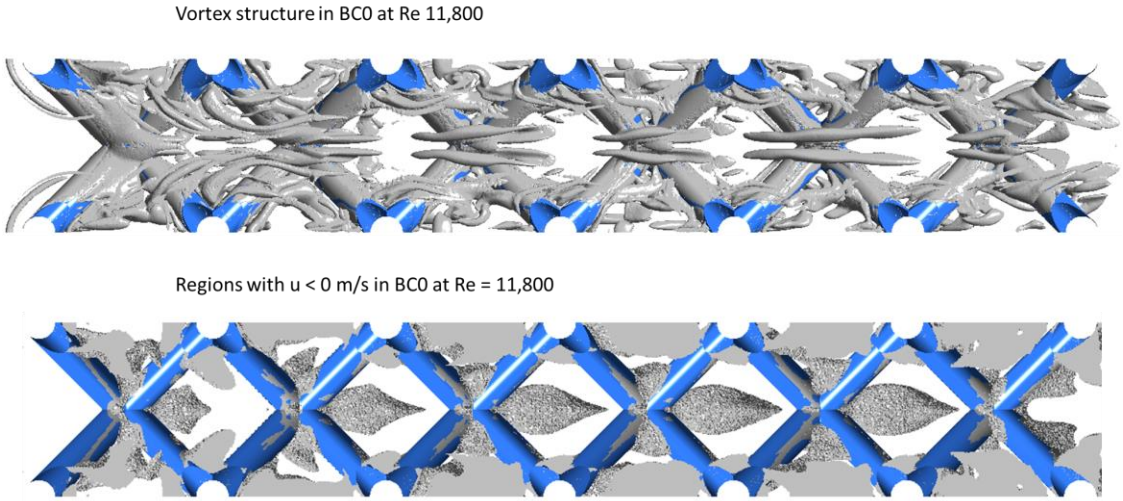

Figure 5.4 Vortex flow and regions with u < 0 m/s in BC0 lattice

5.2 Effect of Filtering Criteria

The effect of the Be_{cutoof} on the filtered volume can be analyzed by defining a ratio,

$$V_r = \frac{filtered\ fluid\ volume}{total\ channel\ volume} \quad (5.1)$$

where, "filtered fluid volume" referred to the cumulative V_{Be}, V_{vel}, or V_Q, based on the filtering criterion used. Figure 5.5 shows V_{Be}/V_{tot}, V_{vel}/V_{tot}, and V_Q/V_{tot} against Be_{cutoff} (x-axis), as well as the $S_h/S_{h,tot}$ and $S_f/S_{f,tot}$ ratios for this volume (y-axis). These values are shown only for Zone 2, since that's where most of the heat transfer and pressure losses took place. In all cases, the cumulative volume increased with an increase in the Be_{cutoff}. However, while V_{Be} became equal to the total fluid volume within the channel, V_{vel} and V_Q only reached a fraction of this value because negative streamwise velocity and vortical structures were not present everywhere within the flow domain. A similar trend was observed for the two entropy ratios, $S_h/S_{h,tot}$ and $S_f/S_{f,tot}$. In addition, an increase in the Re beyond 5000 led to a steep rise in the volume and entropy ratios at lower Be_{cutoff} values, which indicated that the low Be regions within bulk flow became more dominant with Re. In all cases, when the Be_{cutoff} was fixed, V_Q was greater than V_{vel} which showed that for BC0 lattices, the vortical structures were more dominant factor for both the heat transfer and the pressure losses, compared to the wakes. Thus, such plots also provide a new way of breaking down the flow filed composition.

The V_{Be}/V_{tot} and V_Q/V_{tot} curves (black) intersected with the corresponding $S_f/S_{f,tot}$ curve (red). On the left of this intersection point, the volume ratio was larger than the $S_f/S_{f,tot}$ ratio, while on the right side, it was smaller. This indicated that at the intersection point, the fluid region still unselected by the cutoff criteria had higher per unit volume dissipation rate. This behavior corresponded with fluid in the near wall regions where the prevalent high temperature and velocity

gradients in the boundary layer would lead to high entropy production from both modes. In case of V_Q, even the $S_h/S_{h,tot}$ curve (green) intersected with the corresponding V_r curve at higher Be_{cutoff} values for the same reason. Interestingly, the plots also indicated that the cumulative contribution of the vortical flows to S_h was > 40% while only constituting ~32% of the total channel volume. Similarly, in case of V_{vel}, the region lying beyond the intersection between the $S_f/S_{f,tot}$ and $S_h/S_{h,tot}$ curves indicated that within the still unselected wake regions, the entropy production due to heat transfer dominated that due to viscous-dissipation. Thus, these plots provided a way of directly comparing the relative contribution of wake regions, vortices, and near wall regions to the heat transfer and overall pressure loss in a complex geometry, such as the BC0 lattice. In addition, all the intersection points moved towards left with an increase in the Re because both the viscous dissipation and heat transfer mechanisms strengthened due to the increased turbulence intensity and secondary flows within the bulk flow with Re. From the above discussion, it can also be concluded that an efficient heat transfer design would exhibit a more gradual change in these ratios when plotted against the Be_{cutoff}.

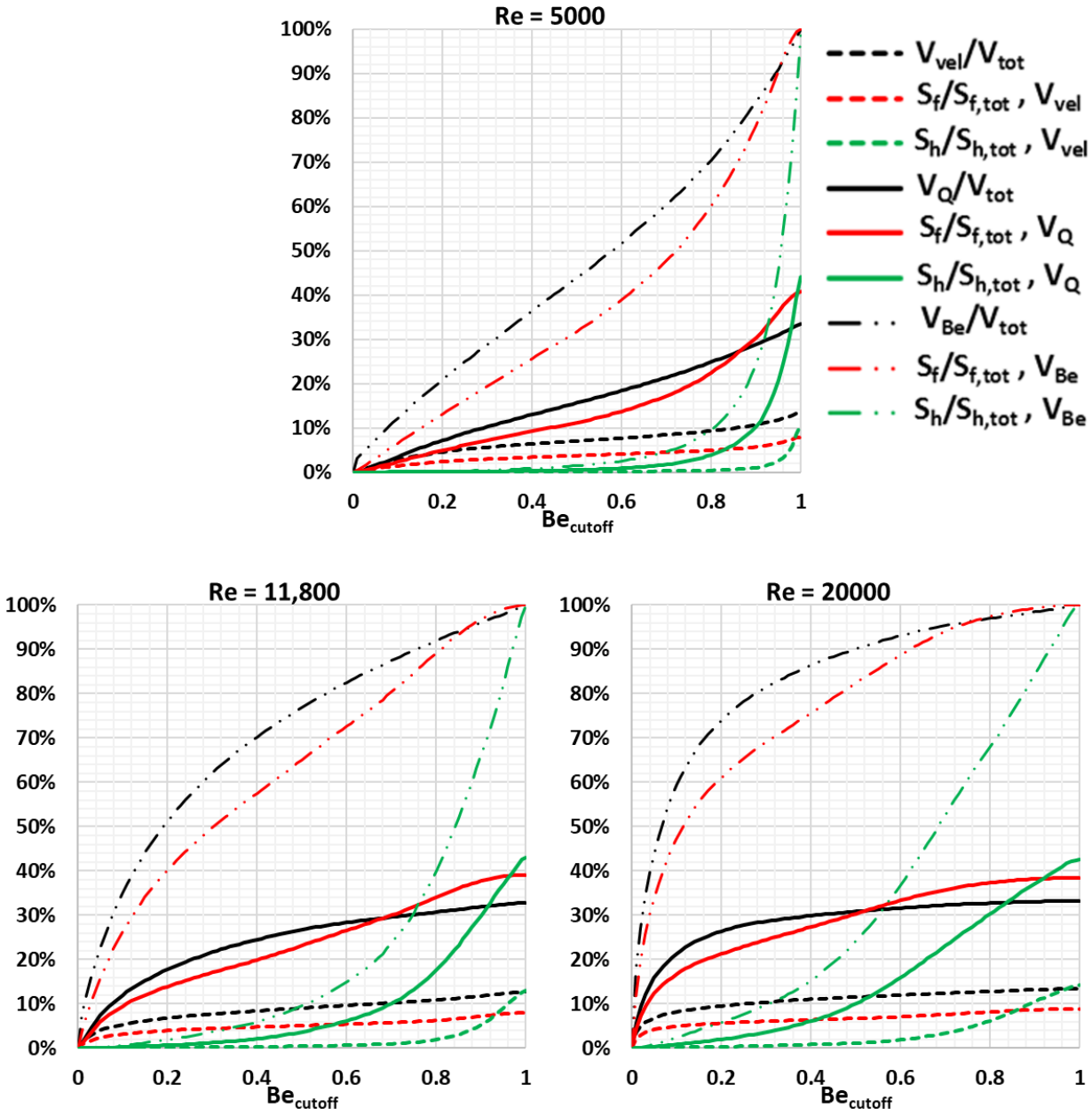

Figure 5.5 Plots comparing the cumulative change in volume and entropy generation rates of the filtered fluid region in Zone 2 using the three types of criteria at different Re

Figure 5.5 provided an insight into the contribution of prominent flow field features to overall entropy generation in the channel. In most applications, the regions of high losses (Be → 0) are of interest from the point of view of optimization of the thermal performance. One approach

of identifying such regions could be to fix a Be_{cutoff} value and obtain the corresponding V_{Be}, V_{vel}, or V_Q, as discussed in the previous sections, and then undertake lattice topology or shape optimization studies to eliminate these regions. Another approach of filtering such regions could be to fix the $S_f/S_{f,tot}$ at a desired value, get the corresponding Be_{cutoff} value for V_{Be}, V_{vel}, and V_Q. An example has been shown in Fig. 5.6, where the $S_f/S_{f,tot}$ was fixed at 0.025 and the corresponding Be_{cutoff} value was calculated to be 0.007 for $V_{Be,}$ 0.05 for V_{vel}, and 0.021 for V_Q for the case with Re = 11,800.

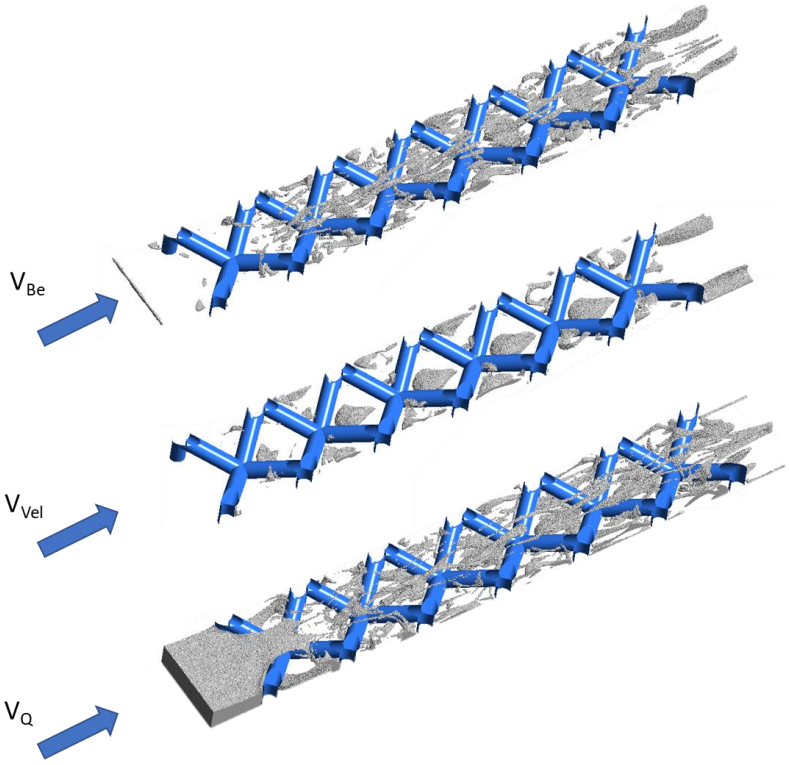

Figure 5.6 Comparison of fluid region (Re = 11,800) filtered by fixing the $S_f/S_{f,tot}$ = 0.025. The three resulting Be_{cutoff} values were 0.0075 for V_{Be}, 0.0585 for V_{vel}, and 0.0183 for V_Q.

In both these approaches, V_{vel} and V_Q, obtained by velocity-based and Q-criterion based filtering, respectively, provided a more useful volume selection criterion. They highlighted fluid regions located within physically significant flow features, like wakes and vortices, which were

very closely related to the geometry of the lattice. There is a possible benefit of selecting V_Q over V_{vel} because a smaller manipulation of lattice geometry near the origin of the vortical structures could result in larger performance gains throughout the channel. On the other hand, regions in V_{vel} were relatively independent because they were concentrated in the wake flow, and thus, more accessible for elimination through local geometry manipulations.

5.3 Topology Optimization of Unit Cell Using Second Law Analysis

5.3.1 Proposed Topology Optimization Scheme and Implementation

The proposed topology optimization process targeted the filtered fluid volume and replaced them with a thermally active solid domain. There were two advantages of this proposed approach: 1) the viscous dissipation-dominated fluid pockets were suppressed due to the presence of the solid volume, and 2) the conducting solid provided additional heat transfer surface area. Fig. 5.7 shows an overview of this scheme.

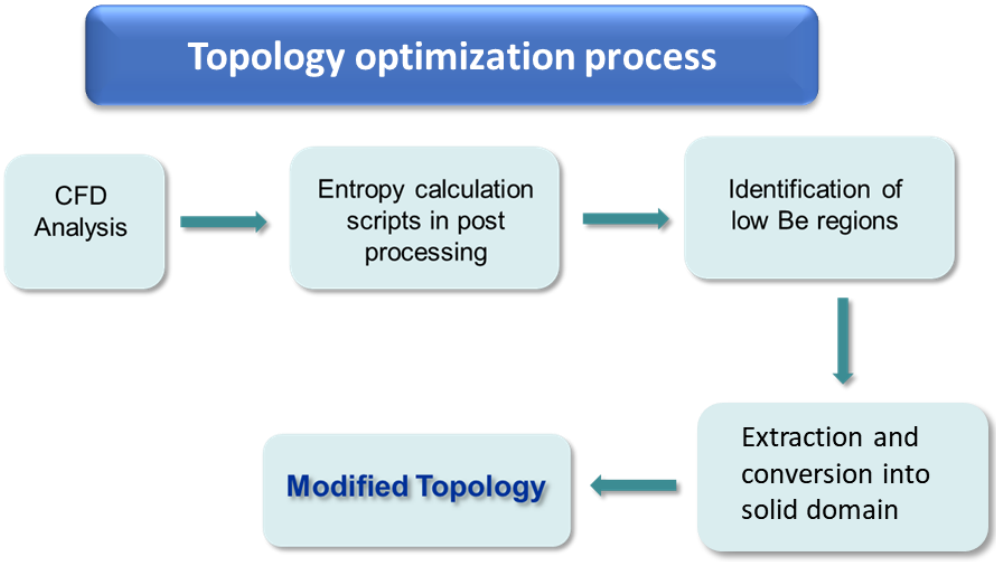

Figure 5.7 Overview of the proposed topology optimization sccheme using the second law analysis

5.3.2 Extracting Regions of Interest

For the topology optimization, only a single unit cell from the array was selected to simplify the process. Based on the results from the previous section, there were two possible volume selection methods: velocity based, *Q*-criterion based. One of the main differences between the two methods was the proportion of the total channel volume represented by each of them. The velocity-based filtering led to a smaller filtered volume among the two. This implied that this filtering criteria would result in a smaller modification in the unit cell design, hence, use of smaller amount of added material. Thus, for the present work, the use of velocity-based filtering was deemed a better choice compared to the Q-criterion filtering. The first step of filtering the desired volume was to determine the appropriate Be_{cutoff} value. To determine this value, at first, the $S_f/S_{f,tot}$ vs Be was plotted for V_{vel} to obtain the functional relationship between these two quantities. Next, an arbitrary value of the $S_f/S_{f,tot}$ was fixed, and the corresponding value of Be was calculated, which served as the desired Be_{cutoff}. This arbitrary value of $S_f/S_{f,tot}$, could be selected by the designer from

the performance point of view to only highlight fluid regions that had a prescribed contribution to the overall viscous losses in the channel.

Fig. 5.8 shows a single unit cell from the 2nd row with the filtered volume (Re = 11,800). As discussed earlier, two dominant features were present in the highlighted fluid regions. The first one was located in the wake of the body center node while the second feature was located in the wake of the upstream vertices.

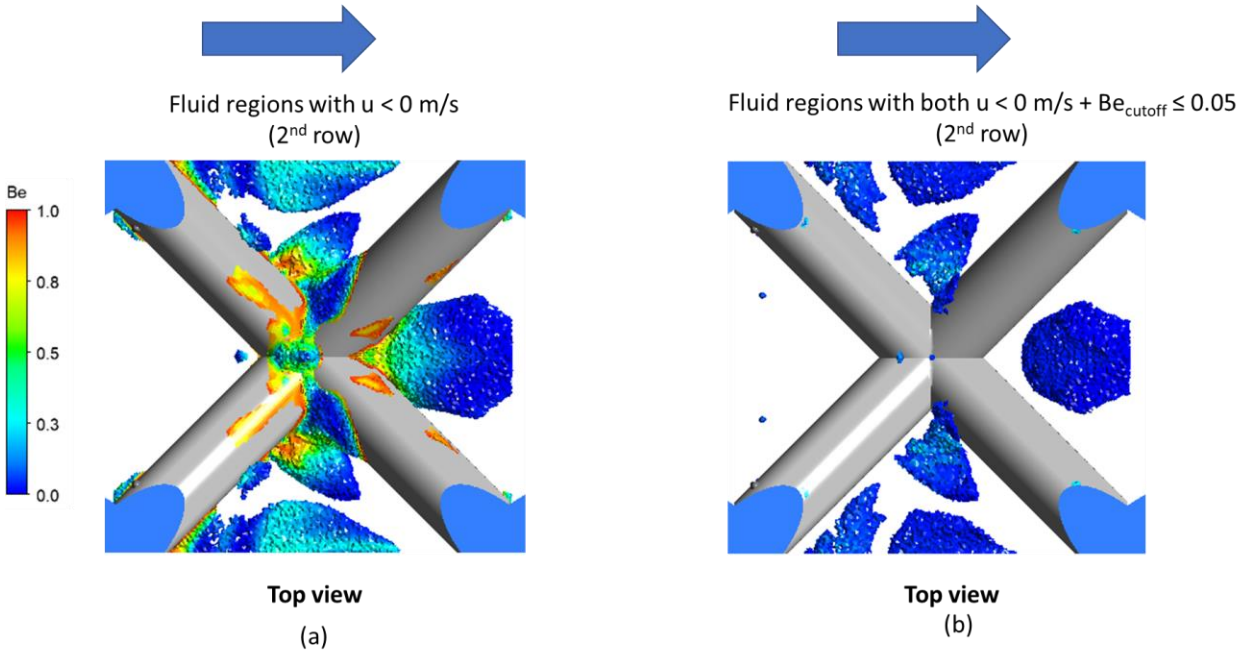

Figure 5.8 Selection of regions for topology optimization in BC0: (a) wake regions identified by u <= 0 m/s, and (b) after subtracting high Be regions (V_{vel})

In the next step, these fluid regions were extracted in the form of a point cloud (Fig. 5.9) and imported into SolidWorks [97] CAD package to generate solid volumes, which were then merged with the original unit cell. As a result, a modified topology of the unit cell was obtained as shown in Fig. 5.10 . The new topology consisted of new streamwise oriented ligaments and a modified body center node.

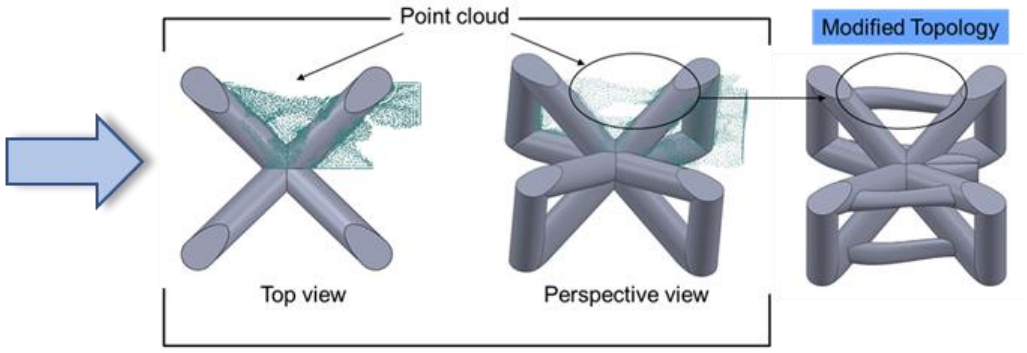

Figure 5.9 Exporting and converting the point cloud into solid domain to obtain the modified topology

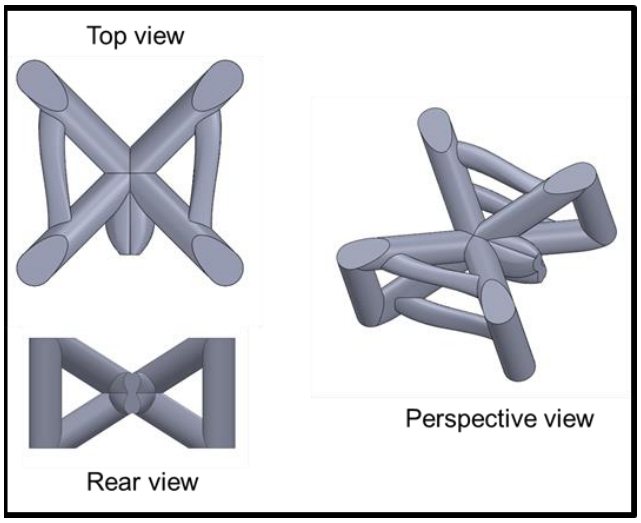

Figure 5.10 Optimized BC unit cell topology

5.3.3 Comparison of Performance

The steady state conjugate numerical simulation was re-run with a lattice similar to the original BC0, but generated with the optimized unit cells, and the aerothermal properties were compared over a range of channel Re values. The results from these simulations are summarized in Fig. 5.11. As shown, on comparing the two types of unit cells, the targeted low Be regions

(Be_{cutoff} = 0.05) were reduced by up to 80% after the TO. Overall, the results showed that the new topology resulted in a lower pressure drop while increasing the heat removal rate in the lattice. Figure 5.12 compares BC0 and BC0-Rev in terms of S_f and S_h at various channel Re. The modified topology of BC0-Rev resulted in an 8% decrease in S_f, at higher Re values. These results validated the developed topology optimization approach for enhancing the aero-thermal behavior of complex lattice geometries. In addition, this plot represents a unique capability to identify the optimal operation zone for a given heat transfer enhancement geometry. At about Re = 15,000, the two components became equal, and this indicated an optimum operation regime. This is because, beyond this point, an augmentation in the heat transfer mechanisms was accompanied with a greater increase in the mechanisms generating the viscous losses.

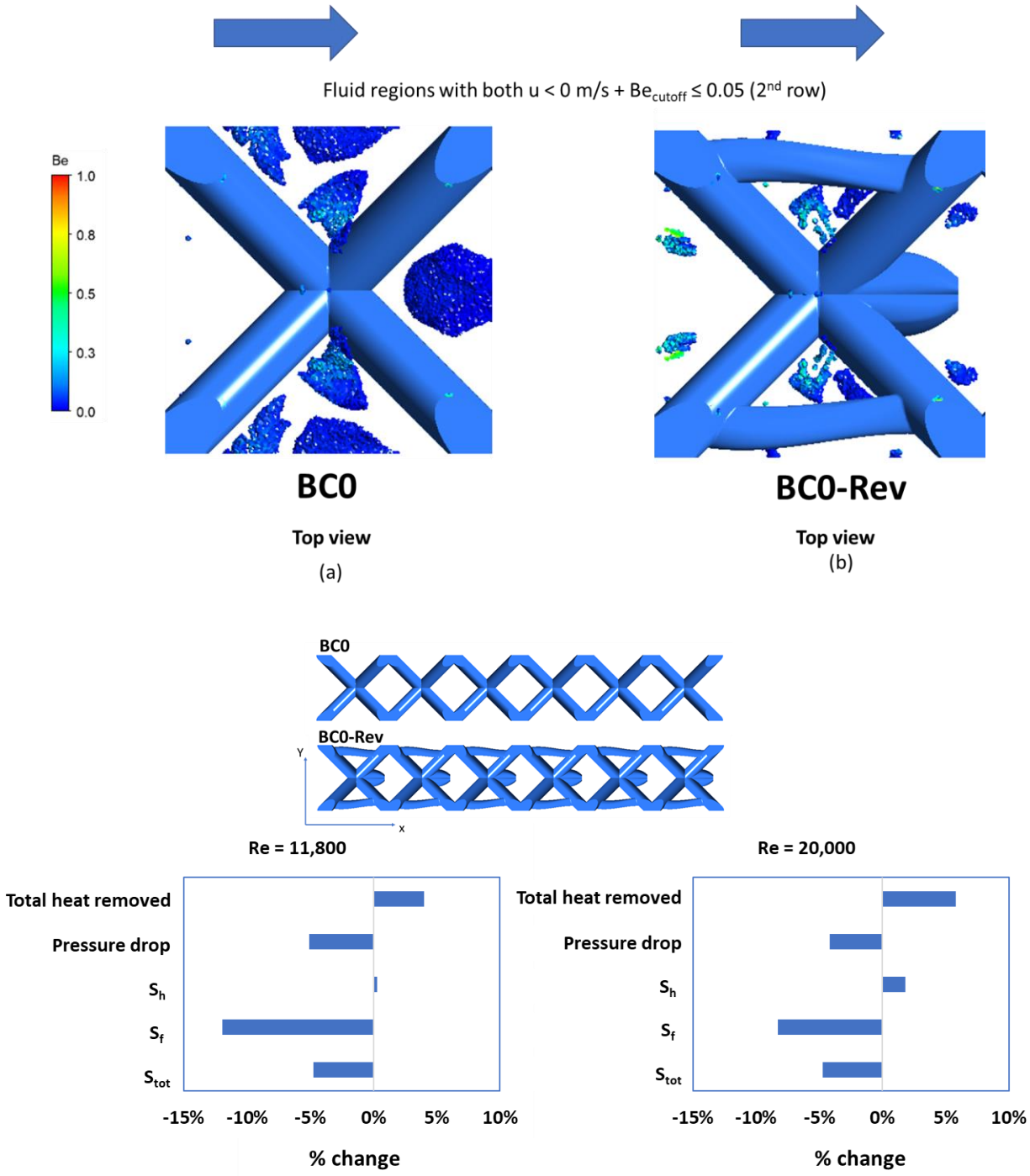

Figure 5.11 (Top) reduction in targetted low Be regions for 2nd row unit cell after TO. (Bottom) Comparison between original and modified topology simulation results. The x-axis represents the % change in BC0-Rev compared to the BC0 lattice

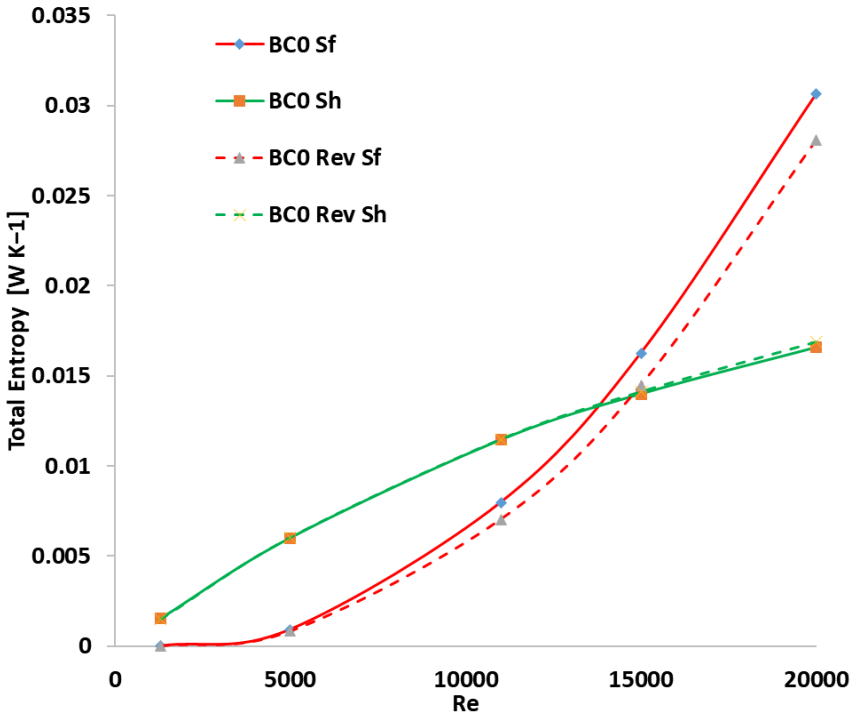

Figure 5.12 Comparison of total entropy generated by the two mechanisms between BC0 and BC0 Rev at different channel Re

Figure 5.13 plots the row-resolved entropy generation values for both BC0 and BC0-Rev topologies against the channel Re on logarithmic scale. As can be observed, the S_h curves for each of the rows lied on a distinct curve. The first row of the lattice showed the highest S_h for any given Re due to high temperature difference between the coolant and the walls. This temperature difference diminished as the coolant flowed down the channel and picked up heat. Thus, the S_h values also decreased for the downstream rows. On the other hand, S_f curves showed that the row resolved value of S_f for R2-R6 were very close together and higher than that of R1 at all Re. The increase in the turbulence and mixing due to the development of secondary flows and wake shedding, led to a higher entropy generation in the downstream rows.

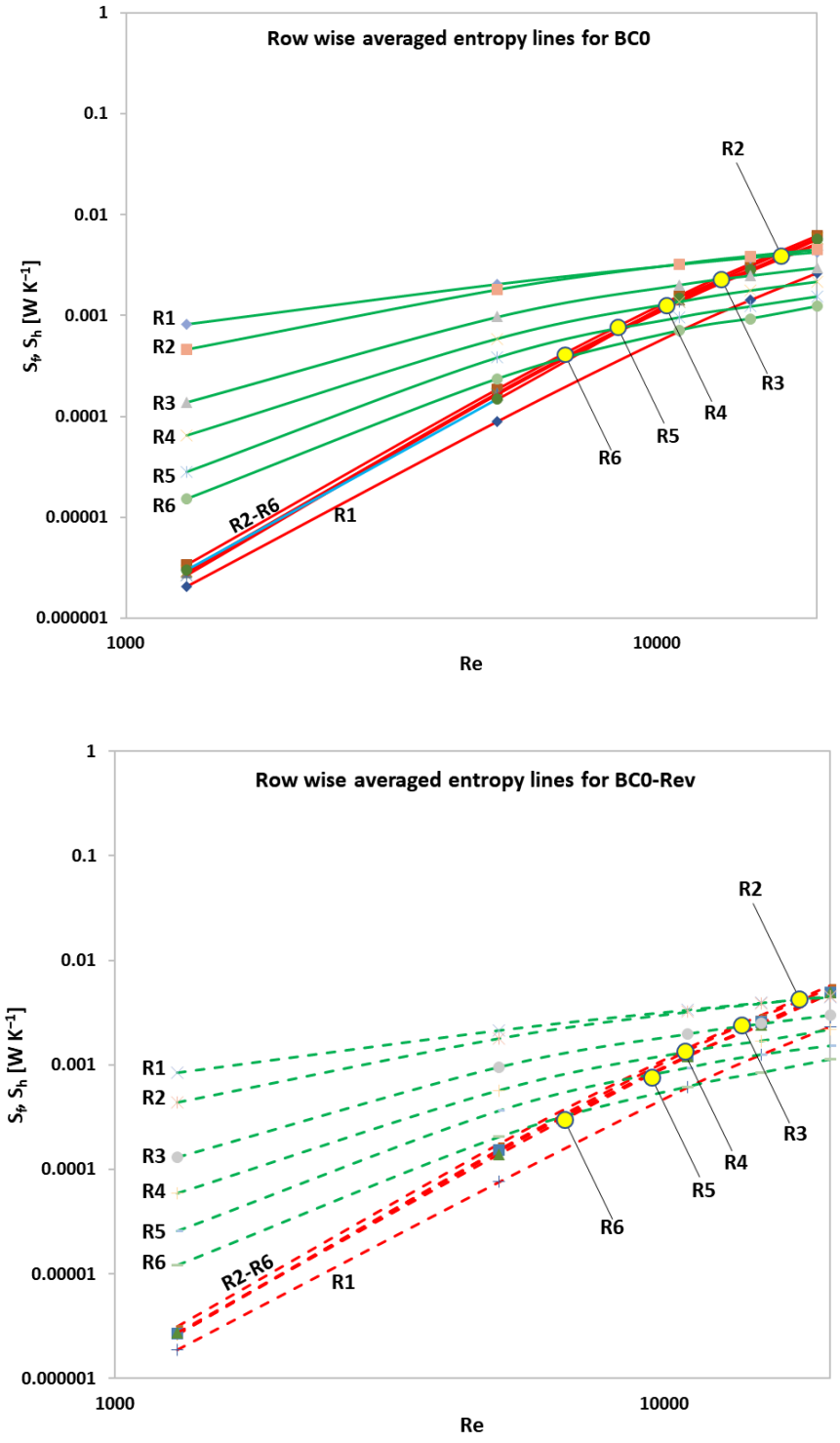

Figure 5.13 Variation of entropy generation in each row vs channel Re for BC0 (above) and BC0-Rev (below)

In summary, in this chapter, second law based analysis was extended to lattice type geometries. To the authors best knowledge, this is the first time this method has been applied to single layer lattice geometries for gas turbine application. By tracking the entropy generation rates due to local temperature gradient and viscous losses, it was shown that a deeper understanding of the origins of the loss in aerothermal performance could be obtained. Further, by introducing a method of tracking local Be and using one of the two proposed filtering criteria, it was possible to precisely isolate flow vortex dominant or wake flow regions responsible for a defined portion of the total viscous losses in the domain. As a result, a new level of insight was achieved through such an analysis. It was also shown that such an insight could be leveraged to optimize the topology of the lattice geometry and the method was demonstrated for BC0 lattice in turbulent flow. Furthermore, it was shown that second law analysis could be used to predict the optimal number of rows in these geometries. Such a knowledge is indispensable in extracting the maximum performance out of the complex lattice geometries.

6.0 Conclusions and Future Work

6.1 Major Accomplishments

The presented research work provides a deep understanding of heat transfer and pressure loss in lattice geometries which are suitable for application in internal cooling of gas turbine airfoils. DMLS AM process was demonstrated as a successful means to fabricate these complex geometries using commercial IN718 superalloy powder. The overall heat transfer and pressure loss in these complex geometries was investigated at realistic length scales. In addition, scaled up tests were performed using thermally inactive lattices to study the effect of these geometries on local heat transfer coefficient on channel end wall. Steady state numerical simulations were also conducted to reveal the prevalent flow field and its impact on the observed aerothermal performance of lattices. A new integrated architecture was proposed and investigated for the first time that marries advanced transpiration and lattice cooling together to provide simultaneous internal and external cooling to the airfoils. These geometries take full advantage of state-of-the-art metal additive manufacturing technology. Finally, entropy-based analysis of flow field was extended to lattice geometries and a new method of isolating and optimizing of low performance regions in the flow domain was proposed and demonstrated.

6.1.1 Conjugate Aerothermal Analysis of True-Scale Additively Manufactured Lattice Geometries

Four types of lattice geometries were designed and fabricated using DMLS AM process and IN718 superalloy powder. The lattices were fabricated by arranging a single layer of the corresponding unit cell in an inline array. In contrast to most of the current studies where the lattices are compared by making the porosity constant, this research fixed the dimensions of the unit cell, ligament diameter, and the orientation with respect to the incoming flow among the lattices to be compared. Such a comparison is more relevant for gas turbine cooling applications because single layer is the more favorable configuration for the airfoil's internal cooling channels. In such single layer lattices, the impact of each of the ligament becomes more important than in a multilayer design where the properties are averaged or approach stochastic in nature. It was shown that with other geometric parameters held constant, with an increase in the ligament diameter, the heat transfer and pressure drop increased in the tested Re range. This was attributed to both an increase in the surface area, and the enhanced secondary and wake flows with thicker ligaments. The effect of orientation on the aerothermal performance was more complex. A rotation from 0° to 45° led to an increase in heat transfer in all but OCTA lattices, where there was a 10% decline. Similarly, for the max-close orientation, the BC lattice was the only one that showed a further 7%-8% improvement. In terms of the pressure drop, the rotation from 0° to 45° led to a greater pressure loss in BC and Kagome lattices, and a decrease in OCTA lattice. Similarly, the maximum blockage orientation did not result in higher heat transfer and pressure loss in all the lattices. Thus, the relative arrangement of ligaments in a given lattice with respect to flow was shown to be an important consideration that has been relatively less explored in existing literature. The research also contrasted the performance of these lattices with traditional pin fin banks and identified the

fin efficiency as an important factor in extracting maximum performance. Overall, for applications with high heat transfer requirements, the OCTA lattices were found to be most suitable. On the other hand, for applications where both pressure drop and heat transfer have to be considered simultaneously, Kagome and the max-close variation of BC and FC are recommended.

6.1.2 Impact of Lattice Topology and Orientation on End Wall Heat Transfer Coefficient

The external end walls of the cooling channels located in a gas turbine airfoil are subjected to high heat flux from the hot combustion gases. As a result, it is very important to have a high cooling even in end wall regions where there is absence of any enhanced cooling geometries like pin fins and lattices. Thus, this research work investigated the distribution of heat transfer on the end walls of a channel embedded with the proposed lattice structures. The TLC tests were conducted to obtain high resolution h on the channel walls at a range of Re. It was shown that this distribution was highly dependent not only on the unit cell topology, but also on the orientation with respect to the flow. It was shown that compared to a traditional pin fin, where the highest heat transfer regions are located at the base of the pin owing to the horse-shoe vortices, the lattices showed multiple peaks in the h. These peaks appeared as a result of both horse-shoe type vortices as well as complex wake flow structures behind the vertices and the ligaments. In addition, the research revealed that each type of unit cell and its orientation created a unique distribution of h on the end walls. As such, the end wall h can be tailored using a combination of such unit cells to obtain the desired cooling effect and eliminate local hot spots. Numerical analysis was also performed on these lattices and it was shown that the end wall h was closely related to the TKE distribution near the walls. Since TKE is affected by the secondary flow structures and wake

shedding behind ligaments, these results once again emphasized the importance of considering both the topology as well as the orientation in lattice geometries.

6.1.3 Novel Integrated Lattice-Transpiration Cooling Architectures and Characterization of Their Overall Cooling Effectiveness

To answer the ever-growing challenge of achieving high cooling in gas turbine airfoils, the research proposed a novel integrated lattice-transpiration cooling architecture with high cooling effectiveness. This architecture fully leveraged the flexibility afforded by state-of-the-art DMLS AM process and combined together advanced transpiration cooling with the proposed lattice geometries. Four integrated cooling architectures were designed and fabricated using IN718 superalloy and DMLS AM process. The results for overall cooling effectiveness in plenum fed configuration showed that these geometries could reach near pure transpiration performance, with some loss in cooling due to transpiration holes being blocked by the footprint. This also demonstrated that the lattices are the most suitable geometries to be paired with transpiration cooling as they provide much higher surface area to footprint area ratio compared to traditional pin fins. The results for crossflow fed configuration showed that the overall cooling effectiveness increased with addition of the lattices for a non-zero crossflow. Additionally, it was revealed that under CF-fed configurations, these geometries provided a relatively stable overall cooling effectiveness even when the transpiration flow decreased. Thus, it was demonstrated that this architecture could counteract the effects of pore blockage during operation by providing additional cooling from the backend lattices.

6.1.4 Introduction of Second Law Based Analysis to Lattice Geometries and New Topology Optimization Scheme

In the final section, the presented research showed that implementing an entropy based analysis of the complex flow field present in the lattice type internal cooling geometries could provide significant benefits towards understanding their aerothermal behavior. The concept of applying Bejan number to precisely filter out desired flow field structures by defining two possible filtering criteria was developed and demonstrated for BC0 lattice. These filtering criteria allowed for isolation of fluid regions which contributed a prespecified portion of the total losses in the flow. This provided a powerful technique to perform precise geometry modifications to minimize such loss dominant regions and achieve improved aerothermal performance in lattices. This modification was achieved by replacing the isolated flow regions with thermally conducting solid domain. This substitution suppressed the viscous losses in these loss dominant regions and improved local heat transfer through newly add surfaces. The key advantages of proposed topology optimization scheme were that it can be implemented as a post processing step and did not require a custom solver. In addition, this scheme can handle complex geometries in a turbulent flow which is difficult to achieve through traditional optimization schemes. Apart from optimization of geometries, second law analysis also provided a quantitative insight into an optimal number of rows in the lattice geometries for a given channel Re.

6.2 Future Work

A comprehensive work was undertaken in this research to design, additively manufactured, characterize, and optimize lattice-type internal and integrated cooling geometries. The proposed novel geometries and topology optimization method has opened up new pathways to tailor the heat transfer within advanced airfoils. Thus, several lines of research could be pursued in order to build upon the results presented here.

In terms of true-scale additively manufactured geometries, although the effect of some of the key geometric parameters was measured (Chapter 2), there is an extremely wide variety of possible combinations of topologies and related geometric parameters for lattices. Therefore, a systematic and concentrated effort is needed to explore their impact on the aerothermal performance of these geometries. Although the effect of roughness was quantified for an additively manufactured smooth channel, future work is needed to characterize the fabrication tolerance and roughness in lattices and their effect on the performance. Additionally, a study on the impact of channel wall curvature and rotation on the overall aerothermal behavior is warranted for these relatively new internal cooling geometries.

As shown in Chapter 3, each unit cell depicted a unique distribution of h on the end walls of the channel. This indicated that the end wall heat transfer could be tailored to meet the location-specific cooling in turbine airfoils. Such tailoring could be achieved by not only combining different unit cell topologies but also by varying the ligament diameter and orientation for a given unit cell. This opens up a new paradigm in the design of internal cooling of airfoils which was not possible with traditionally used geometries. Thus, future research efforts are required in this aspect of lattice cooling.

The novel integrated cooling architecture proposed in Chapter 4 has the potential of making the highly sought-after transpiration cooling concept realizable through AM. This is because this architecture answers two of the most important issues with transpiration designs: 1) lack of wall strength and 2) susceptibility to blockage. However, only a single transpiration design was considered with the four types of lattices. There is a need to study the impact of combining various possible AM transpiration designs with the lattices on the backend. In addition, the impact of varying the porosity of the lattices, either through changing ligament thickness or by combining different unit cells, needs to be investigated. Such a design could achieve simultaneous optimization on both internal and external cooling and would take full advantage of the advanced AM processes.

The combination of Bejan number based analysis with the proposed filtering criteria is capable of quantifying the impact of individual flow field structures on aero-thermal losses in highly complex geometries. Chapter 5 studied this approach only for the BC0 lattice. Thus, the next step would be to analyze the remaining lattice designs and perform topology optimization using the proposed method. The presented results were derived through numerical calculations. As such, fabrication and experimental quantification of the performance of these optimized geometries should be carried out. The proposed method was implemented as a single post-process step. It would be very interesting to see the TO results by implementing this approach in an iterative fashion to generate the topology using seed points, especially by using the Q-criterion based approach.

Bibliography

[1] Dahl, J., 2007, *Diagram of a Typical Gas Turbine Jet Engine.*

[2] Services, P.-P. E., 2007, *Türkçe: Aeroderivative Gaz Türbinlerine Ait Tüm Paket Parçalarını Müşterilerimize Tedarik Ediyoruz. LM2500 ve LM6000 Serilerinde Sağladığımız Yedek Parça Hizmetleri, Ihtiyaclarınız Ile Ilgili Teknik Değerlendirme, Yönlendirme ve Gaz Türbine & Paket Desteğini de Içermektedir.*

[3] Alvin, M. A., Pettit, F., Meier, G. H., Yanar, M., Helminiak, M., Chyu, M., Siw, S., Slaughter, W. S., Karaivanov, V., Kang, B. S., Feng, C., Tannebaum, J. M., Chen, R., Zhang, B., Fu, T., Richards, G. A., Sidwell, T. G., Straub, D., Casleton, K. H., and Dogan, O. M., 2008, *Materials and Component Development for Advanced Turbine Systems*, DOE/NETL-IR-2008-235; NETL-TPR-2230, National Energy Technology Laboratory (NETL), Pittsburgh, PA, Morgantown, WV, and Albany, OR.

[4] Chyu, M. K., and Alvin, M. A., 2010, "Turbine Airfoil Aerothermal Characteristics in Future Coal-Gas-Based Power Generation Systems," HTR, **41**(7).

[5] Boyce, M. P., 2012, *Gas Turbine Engineering Handbook*, Elsevier/Butterworth-Heinemann, Amsterdam ; Boston.

[6] Chyu, M. K., 2012, "Recent Advances in Turbine Heat Transfer—With A View of Transition to Coal-Gas Based Systems," J. Heat Transfer, **134**(3).

[7] Han, J.-C., and Rallabandi, A. P., 2010, "TURBINE BLADE FILM COOLING USING PSP TECHNIQUE," Frontiers in Heat and Mass Transfer, **1**(1).

[8] "Gas Turbine Handbook," netl.doe.gov [Online]. Available: https://netl.doe.gov/carbon-management/turbines/handbook. [Accessed: 21-Sep-2022].

[9] Han, J. C., Dutta, S., and Ekkad, S., *Gas Turbine Heat Transfer and Cooling Technology*, CRC Press, Boca Raton, FL.

[10] Ligrani, P., 2013, "Heat Transfer Augmentation Technologies for Internal Cooling of Turbine Components of Gas Turbine Engines," International Journal of Rotating Machinery, **2013**, pp. 1–32.

[11] Incropera, F. P., DeWitt, D. P., Bergman, T. L., and Lavine, A. S., eds., 2007, *Fundamentals of Heat and Mass Transfer*, Wiley, Hoboken, NJ.

[12] Chyu, M. K., and Natarajan, V., 1996, "Heat Transfer on the Base Surface of Threedimensional Protruding Elements," International Journal of Heat and Mass Transfer, **39**(14), pp. 2925–2935.

[13] Goldstein, R. J., Chyu, M. K., and Hain, R. C., 1985, "Measurement of Local Mass Transfer on a Surface in the Region of the Base of a Protruding Cylinder with a Computer-Controlled Data Acquisition System," International Journal of Heat and Mass Transfer, **28**(5), pp. 977–985.

[14] Choi, I. K., Kim, T., Song, S. J., and Lu, T. J., 2007, "Endwall Heat Transfer and Fluid Flow around an Inclined Short Cylinder," International Journal of Heat and Mass Transfer, **50**(5–6), pp. 919–930.

[15] Chyu, M., Yu, Y., and Ding, H., 1999, "Heat Transfer Enhancement in Rectangular Channels with Concavities," J Enh Heat Transf, **6**(6), pp. 429–439.

[16] Siw, S. C., Chyu, M. K., and Alvin, M. A., 2013, "Effects of Pin Detached Space on Heat Transfer in a Rib Roughened Channel," J. Turbomach, **135**(2).
[17] Chyu, M. K., Siw, S. C., and Moon, H. K., 2010, "Effects of Height-to-Diameter Ratio of Pin Element on Heat Transfer From Staggered Pin-Fin Arrays," American Society of Mechanical Engineers Digital Collection, pp. 705–713.
[18] Axtmann, M., von Wolfersdorf, J., and Meyer, G., 2015, "Application of the Transient Heat Transfer Measurement Technique in a Low Aspect Ratio Pin Fin Cooling Channel," Journal of Turbomachinery, **137**(12), p. 121006.
[19] Žukauskas, A., 1972, "Heat Transfer from Tubes in Crossflow," *Advances in Heat Transfer*, Elsevier, pp. 93–160.
[20] VanFossen, G. J., 1982, "Heat-Transfer Coefficients for Staggered Arrays of Short Pin Fins," Journal of Engineering for Power, **104**(2), pp. 268–274.
[21] Lu, Z. L., Cao, J. W., Jing, H., Liu, T., Lu, F., Wang, D. X., and Li, D. C., 2013, "Review of Main Manufacturing Processes of Complex Hollow Turbine Blades: This Paper Critically Reviews Conventional and Advanced Technologies Used for Manufacturing Hollow Turbine Blades," Virtual and Physical Prototyping, **8**(2), pp. 87–95.
[22] Amin Yavari, S., Ahmadi, S. M., Wauthle, R., Pouran, B., Schrooten, J., Weinans, H., and Zadpoor, A. A., 2015, "Relationship between Unit Cell Type and Porosity and the Fatigue Behavior of Selective Laser Melted Meta-Biomaterials," Journal of the Mechanical Behavior of Biomedical Materials, **43**, pp. 91–100.
[23] Maskery, I., Aboulkhair, N. T., Aremu, A. O., Tuck, C. J., and Ashcroft, I. A., 2017, "Compressive Failure Modes and Energy Absorption in Additively Manufactured Double Gyroid Lattices," Additive Manufacturing, **16**, pp. 24–29.
[24] Smith, M., Guan, Z., and Cantwell, W. J., 2013, "Finite Element Modelling of the Compressive Response of Lattice Structures Manufactured Using the Selective Laser Melting Technique," International Journal of Mechanical Sciences, **67**, pp. 28–41.
[25] Leary, M., Mazur, M., Elambasseril, J., McMillan, M., Chirent, T., Sun, Y., Qian, M., Easton, M., and Brandt, M., 2016, "Selective Laser Melting (SLM) of AlSi12Mg Lattice Structures," Materials & Design, **98**, pp. 344–357.
[26] Zhang, X. Z., Leary, M., Tang, H. P., Song, T., and Qian, M., 2018, "Selective Electron Beam Manufactured Ti-6Al-4V Lattice Structures for Orthopedic Implant Applications: Current Status and Outstanding Challenges," Current Opinion in Solid State and Materials Science, **22**(3), pp. 75–99.
[27] Kim, T., Hodson, H. P., and Lu, T. J., 2005, "Contribution of Vortex Structures and Flow Separation to Local and Overall Pressure and Heat Transfer Characteristics in an Ultralightweight Lattice Material," International Journal of Heat and Mass Transfer, **48**(19–20), pp. 4243–4264.
[28] Gao, L., and Sun, Y. G., 2014, "Fluid Flow and Heat Transfer Characteristics of Composite Lattice Core Sandwich Structures," Journal of Thermophysics and Heat Transfer, **28**(2), pp. 258–269.
[29] Shen, B., Yan, H., Xue, H., and Xie, G., 2018, "The Effects of Geometrical Topology on Fluid Flow and Thermal Performance in Kagome Cored Sandwich Panels," Applied Thermal Engineering, **142**, pp. 79–88.
[30] Parbat, S., Min, Z., Yang, L., and Chyu, M., 2020, "Experimental and Numerical Analysis of Additively Manufactured Inconel 718 Coupons With Lattice Structure," Journal of Turbomachinery, **142**(6), p. 061004.

[31] Liang, D., Chen, W., Ju, Y., and Chyu, M. K., 2021, "Comparing Endwall Heat Transfer among Staggered Pin Fin, Kagome and Body Centered Cubic Arrays," Applied Thermal Engineering, **185**, p. 116306.
[32] Liang, D., He, G., Chen, W., Chen, Y., and Chyu, M. K., 2022, "Fluid Flow and Heat Transfer Performance for Micro-Lattice Structures Fabricated by Selective Laser Melting," International Journal of Thermal Sciences, **172**, p. 107312.
[33] Xi, L., Xu, L., Gao, J., Zhao, Z., and Li, Y., 2021, "Study on Flow and Heat Transfer Performance of X-Type Truss Array Cooling Channel," Case Studies in Thermal Engineering, **26**, p. 101034.
[34] Dixit, T., Nithiarasu, P., and Kumar, S., 2021, "Numerical Evaluation of Additively Manufactured Lattice Architectures for Heat Sink Applications," International Journal of Thermal Sciences, **159**, p. 106607.
[35] Yang, Z., Luo, X., Chen, W., and Chyu, M. K., 2021, "Mitigation Effects of Body-Centered Cubic Lattices on the Heat Transfer Deterioration of Supercritical CO2," Applied Thermal Engineering, **183**, p. 116085.
[36] Wen, M.-Y., and Jang, K.-J., 2002, "Forced Convection Heat Transfer at an Inclined and Yawed Round Tube," International Journal of Heat and Mass Transfer, **45**(10), pp. 2031–2042.
[37] Zhao, M., Cheng, L., and Zhou, T., 2009, "Direct Numerical Simulation of Three-Dimensional Flow Past a Yawed Circular Cylinder of Infinite Length," Journal of Fluids and Structures, **25**(5), pp. 831–847.
[38] Liang, H., and Duan, R.-Q., 2019, "Effect of Lateral End Plates on Flow Crossing a Yawed Circular Cylinder," Applied Sciences, **9**(8), p. 1590.
[39] Narato, P., Wae-hayee, M., Vessakosol, P., and Nuntadusit, C., 2017, "Effect of Inclined Angle of Pin Arrays on Flow and Heat Transfer Characteristics in Flow Channel," IOP Conf. Ser.: Mater. Sci. Eng., **243**, p. 012005.
[40] Younis, M. Y., Alam, M. M., and Zhou, Y., 2016, "Flow around Two Non-Parallel Tandem Cylinders," Physics of Fluids, **28**(12), p. 125106.
[41] Ali, H. M., and Arshad, W., 2017, "Effect of Channel Angle of Pin-Fin Heat Sink on Heat Transfer Performance Using Water Based Graphene Nanoplatelets Nanofluids," International Journal of Heat and Mass Transfer, **106**, pp. 465–472.
[42] Park, J. S., Kim, K. M., Lee, D. H., Cho, H. H., and Chyu, M., 2009, "Heat Transfer in Rotating Channel With Inclined Pin-Fins," *Volume 3: Heat Transfer, Parts A and B*, ASMEDC, Orlando, Florida, USA, pp. 669–678.
[43] Bogard, D. G., and Thole, K. A., 2006, "Gas Turbine Film Cooling," Journal of Propulsion and Power, **22**(2), pp. 249–270.
[44] Albert, J. E., and Bogard, D. G., 2013, "Measurements of Adiabatic Film and Overall Cooling Effectiveness on a Turbine Vane Pressure Side With a Trench," Journal of Turbomachinery, **135**(5), p. 051007.
[45] Yu, Y., Yen, C.-H., Shih, T. I.-P., Chyu, M. K., and Gogineni, S., 2002, "Film Cooling Effectiveness and Heat Transfer Coefficient Distributions Around Diffusion Shaped Holes," Journal of Heat Transfer, **124**(5), pp. 820–827.
[46] Chen, S. P., Chyu, M. K., and Shih, T. I.-P., 2011, "Effects of Upstream Ramp on the Performance of Film Cooling," International Journal of Thermal Sciences, **50**(6), pp. 1085–1094.

[47] Zhang, Y., Xu, Z., Zhu, Y., and Zhu, D., 2016, "Machining of a Film-Cooling Hole in a Single-Crystal Superalloy by High-Speed Electrochemical Discharge Drilling," Chinese Journal of Aeronautics, **29**(2), pp. 560–570.
[48] Zhang, Y., Xu, Z., Zhu, D., Qu, N., and Zhu, Y., 2016, "Drilling of Film Cooling Holes by a EDM/ECM in Situ Combined Process Using Internal and Side Flushing of Tubular Electrode," Int J Adv Manuf Technol, **83**(1–4), pp. 505–517.
[49] Sezer, H. K., Li, L., Schmidt, M., Pinkerton, A. J., Anderson, B., and Williams, P., 2006, "Effect of Beam Angle on HAZ, Recast and Oxide Layer Characteristics in Laser Drilling of TBC Nickel Superalloys," International Journal of Machine Tools and Manufacture, **46**(15), pp. 1972–1982.
[50] Bunker, R. S., 2010, "Film Cooling: Breaking the Limits of Diffusion Shaped Holes," Heat Trans Res, **41**(6), pp. 627–650.
[51] Ramesh, S., Ramirez, D. G., Ekkad, S. V., and Alvin, M. A., 2016, "Analysis of Film Cooling Performance of Advanced Tripod Hole Geometries with and without Manufacturing Features," International Journal of Heat and Mass Transfer, **94**, pp. 9–19.
[52] Andrews, G. E., Asere, A. A., Gupta, M. L., and Mkpadi, M. C., 1990, "Effusion Cooling: The Influence of the Number of Holes," Proceedings of the Institution of Mechanical Engineers, Part A: Journal of Power and Energy, **204**(3), pp. 175–182.
[53] Arcangeli, L., Facchini, B., Surace, M., and Tarchi, L., 2008, "Correlative Analysis of Effusion Cooling Systems," J. Turbomach., **130**(1), p. 011016.
[54] Harrington, M. K., McWaters, M. A., Bogard, D. G., Lemmon, C. A., and Thole, K. A., 2001, "Full-Coverage Film Cooling With Short Normal Injection Holes," Journal of Turbomachinery, **123**(4), pp. 798–805.
[55] Krewinkel, R., 2013, "A Review of Gas Turbine Effusion Cooling Studies," International Journal of Heat and Mass Transfer, **66**, pp. 706–722.
[56] Arai, M., and Suidzu, T., 2013, "Porous Ceramic Coating for Transpiration Cooling of Gas Turbine Blade," J Therm Spray Tech, **22**(5), pp. 690–698.
[57] Liu, Y.-Q., Jiang, P.-X., Jin, S.-S., and Sun, J.-G., 2010, "Transpiration Cooling of a Nose Cone by Various Foreign Gases," International Journal of Heat and Mass Transfer, **53**(23–24), pp. 5364–5372.
[58] Jiang, P.-X., Yu, L., Sun, J.-G., and Wang, J., 2004, "Experimental and Numerical Investigation of Convection Heat Transfer in Transpiration Cooling," Applied Thermal Engineering, **24**(8–9), pp. 1271–1289.
[59] Lombardo, S., Moskowitz, S. L., and Schnure, S. A., 1967, "Experimental Results of a Transpiration-Cooled Turbine Operated in an Engine for 150 Hours at 2500 F Turbine Inlet Temperature," *ASME 1967 Gas Turbine Conference and Products Show*, American Society of Mechanical Engineers, Houston, Texas, USA, p. V001T01A028.
[60] Polezhaev, J., 1997, "The Transpiration Cooling for Blades of High Temperatures Gas Turbine," Energy Conversion and Management, **38**(10), pp. 1123–1133.
[61] Huang, G., Min, Z., Yang, L., Jiang, P.-X., and Chyu, M., 2018, "Transpiration Cooling for Additive Manufactured Porous Plates with Partition Walls," International Journal of Heat and Mass Transfer, **124**, pp. 1076–1087.
[62] Min, Z., Parbat, S. N., Yang, L., and Chyu, M. K., 2019, "Thermal-Fluid and Mechanical Investigations of Additively Manufactured Geometries for Transpiration Cooling," American Society of Mechanical Engineers Digital Collection.

[63] Min, Z., Huang, G., Parbat, S. N., Yang, L., and Chyu, M. K., 2019, "Experimental Investigation on Additively Manufactured Transpiration and Film Cooling Structures," Journal of Turbomachinery, **141**(3), p. 031009.
[64] Andrews, G. E., Asere, A. A., Gupta, M. L., and Mkpadi, M. C., 1985, "Full Coverage Discrete Hole Film Cooling: The Influence of Hole Size," International Journal of Turbo and Jet Engines, **2**(3).
[65] Huang, G., and He, L., 2019, "Influence of Inhomogeneous Porosity on Effusion Cooling," International Journal of Heat and Mass Transfer, **144**, p. 118675.
[66] Murray, A. V., Ireland, P. T., and Romero, E., 2019, "Development of a Steady-State Experimental Facility for the Analysis of Double-Wall Effusion Cooling Geometries," Journal of Turbomachinery, **141**(4), p. 041008.
[67] Ngetich, G. C., Murray, A. V., Ireland, P. T., and Romero, E., 2019, "A Three-Dimensional Conjugate Approach for Analyzing a Double-Walled Effusion-Cooled Turbine Blade," Journal of Turbomachinery, **141**(1), p. 011002.
[68] Walton, M., and Yang, Z., 2014, "Numerical Study of Effusion Cooling Flow and Heat Transfer," Int. J. CMEM, **2**(4), pp. 331–345.
[69] Jung, E. Y., Lee, D. H., Oh, S. H., Kim, K. M., and Cho, H. H., 2010, "Total Cooling Effectiveness on a Staggered Full-Coverage Film Cooling Plate With Impinging Jet," *Volume 4: Heat Transfer, Parts A and B*, ASMEDC, Glasgow, UK, pp. 1889–1896.
[70] Jung, E. Y., Chung, H., Choi, S. M., Woo, T., and Cho, H. H., 2017, "Conjugate Heat Transfer on Full-Coverage Film Cooling with Array Jet Impingements with Various Biot Numbers," Experimental Thermal and Fluid Science, **83**, pp. 1–8.
[71] Murray, A., Ireland, P., Wong, T., Tang, S., and Rawlinson, A., 2018, "High Resolution Experimental and Computational Methods for Modelling Multiple Row Effusion Cooling Performance," IJTPP, **3**(1), p. 4.
[72] Chen, G., Liu, Y., Rao, Y., He, J., and Qu, Y., 2019, "Numerical Investigation on Conjugate Heat Transfer of Impingement/Effusion Double-Wall Cooling with Different Crossflow Schemes," Applied Thermal Engineering, **155**, pp. 515–524.
[73] Singh, P., and Ekkad, S. V., 2017, "Effects of Spent Air Removal Scheme on Internal-Side Heat Transfer in an Impingement-Effusion System at Low Jet-to-Target Plate Spacing," International Journal of Heat and Mass Transfer, **108**, pp. 998–1010.
[74] Ligrani, P., Click, A., Ritchie, D., Liberatore, F., Patel, R., and Ho, Y.-H., 2020, "Double Wall Cooling of an Effusion Plate with Cross Flow and Impingement Jet Combination Internal Cooling: Comparisons of Main Flow Contraction Ratio Effects," International Journal of Heat and Mass Transfer, **150**, p. 119196.
[75] Rhee, D. H., Choi, J. H., and Cho, H. H., 2003, "Flow and Heat (Mass) Transfer Characteristics in an Impingement/Effusion Cooling System With Crossflow," Journal of Turbomachinery, **125**(1), pp. 74–82.
[76] Hong, S. K., Rhee, D.-H., and Cho, H. H., 2006, "Heat/Mass Transfer with Circular Pin Fins in Impingement/Effusion Cooling System with Crossflow," Journal of Thermophysics and Heat Transfer, **20**(4), pp. 728–737.
[77] Nakamata, C., Okita, Y., Matsuno, S., Mimura, F., Matsushita, M., Yamane, T., Fukuyama, Y., and Yoshida, T., 2005, "Spatial Arrangement Dependance of Cooling Performance of an Integrated Impingement and Pin Fin Cooling Configuration," *Volume 3: Turbo Expo 2005, Parts A and B*, ASMEDC, Reno, Nevada, USA, pp. 385–395.

[78] Rao, Y., Liu, Y., and Wan, C., 2018, "Multiple-Jet Impingement Heat Transfer in Double-Wall Cooling Structures with Pin Fins and Effusion Holes," International Journal of Thermal Sciences, **133**, pp. 106–119.
[79] Sigmund, O., and Maute, K., 2013, "Topology Optimization Approaches," Struct Multidisc Optim, **48**(6), pp. 1031–1055.
[80] Dilgen, C. B., Dilgen, S. B., Fuhrman, D. R., Sigmund, O., and Lazarov, B. S., 2018, "Topology Optimization of Turbulent Flows," Computer Methods in Applied Mechanics and Engineering, **331**, pp. 363–393.
[81] Pietropaoli, M., Ahlfeld, R., Montomoli, F., Ciani, A., and D'Ercole, M., 2017, "Design for Additive Manufacturing: Internal Channel Optimization," J. Eng. Gas Turbines Power, **139**(10).
[82] Dilgen, S. B., Dilgen, C. B., Fuhrman, D. R., Sigmund, O., and Lazarov, B. S., 2018, "Density Based Topology Optimization of Turbulent Flow Heat Transfer Systems," Struct Multidisc Optim, **57**(5), pp. 1905–1918.
[83] Bejan, A., 1996, *Entropy Generation Minimization: The Method of Thermodynamic Optimization of Finite-Size Systems and Finite-Time Processes*, CRC Press, Boca Raton.
[84] Herwig, H., and Kock, F., 2006, "Direct and Indirect Methods of Calculating Entropy Generation Rates in Turbulent Convective Heat Transfer Problems," Heat Mass Transfer, **43**(3), pp. 207–215.
[85] Herwig, H., and Schmandt, B., 2014, "How to Determine Losses in a Flow Field: A Paradigm Shift towards the Second Law Analysis," Entropy, **16**(6), pp. 2959–2989.
[86] Kock, F., and Herwig, H., 2004, "Local Entropy Production in Turbulent Shear Flows: A High-Reynolds Number Model with Wall Functions," International Journal of Heat and Mass Transfer, **47**(10–11), pp. 2205–2215.
[87] Alfonsi, G., 2009, "Reynolds-Averaged Navier–Stokes Equations for Turbulence Modeling," Applied Mechanics Reviews, **62**(4), p. 040802.
[88] Paoletti, S., Rispoli, F., and Sciubba, E., 1989, "Calculation of Exergetic Losses in Compact Heat Exchanger Passages," ASME AES, **10**(2), pp. 21–29.
[89] Wang, W., Zhang, Y., Liu, J., Wu, Z., Li, B., and Sundén, B., 2018, "Entropy Generation Analysis of Fully-Developed Turbulent Heat Transfer Flow in Inward Helically Corrugated Tubes," Numerical Heat Transfer, Part A: Applications, **73**(11), pp. 788–805.
[90] Jin, Y., and Herwig, H., 2014, "Turbulent Flow and Heat Transfer in Channels with Shark Skin Surfaces: Entropy Generation and Its Physical Significance," International Journal of Heat and Mass Transfer, **70**, pp. 10–22.
[91] Sahiti, N., Krasniqi, F., Fejzullahu, Xh., Bunjaku, J., and Muriqi, A., 2008, "Entropy Generation Minimization of a Double-Pipe Pin Fin Heat Exchanger," Applied Thermal Engineering, **28**(17), pp. 2337–2344.
[92] Xie, G., Song, Y., Asadi, M., and Lorenzini, G., 2015, "Optimization of Pin-Fins for a Heat Exchanger by Entropy Generation Minimization and Constructal Law," Journal of Heat Transfer, **137**(6), p. 061901.
[93] Trancossi, M., and Pascoa, J., 2018, "A New Dimensionless Approach to General Fluid Dynamics Problems That Accounts Both the First and the Second Law of Thermodynamics," MMEP, **5**(4), pp. 331–340.
[94] Iandoli, C. L., and Sciubba, E., 2005, "3-D Numerical Calculation of the Local Entropy Generation Rates in a Radial Compressor Stage."

[95] “EOS M 290 - Industrial 3D Printed Parts from Metal Materials” [Online]. Available: https://www.eos.info/eos-m290. [Accessed: 20-Mar-2020].
[96] “EOS Industrial 3D Printing - Process, Method and Benefits” [Online]. Available: https://www.eos.info/additive_manufacturing/for_technology_interested?_scrivito_display_mode=view&_scrivito_workspace_id=published. [Accessed: 20-Mar-2020].
[97] “3D CAD Design Software” [Online]. Available: https://www.solidworks.com/home-page-2020. [Accessed: 21-Mar-2020].
[98] “Effects of Different Recoater Materials in Metal AM” [Online]. Available: https://www.eos.info/en/blog-articles/recoater_whitepaper. [Accessed: 01-Oct-2022].
[99] Kaji, F., and Barari, A., 2015, “Evaluation of the Surface Roughness of Additive Manufacturing Parts Based on the Modelling of Cusp Geometry,” IFAC-PapersOnLine, **48**(3), pp. 658–663.
[100] Stimpson, C. K., Snyder, J. C., Thole, K. A., and Mongillo, D., 2017, “Scaling Roughness Effects on Pressure Loss and Heat Transfer of Additively Manufactured Channels,” Journal of Turbomachinery, **139**(2), p. 021003.
[101] Parbat, S. N., Yang, L., Min, Z., and Chyu, M. K., 2019, “Experimental and Numerical Analysis of Additively Manufactured Coupons With Parallel Channels and Inline Wall Jets,” Journal of Turbomachinery, **141**(6), p. 061004.
[102] Min, Z., Wu, Y., Yang, K., Xu, J., Parbat, S. N., and Chyu, M. K., 2021, “Dimensional Characterizations Using Scanning Electron Microscope and Surface Improvement With Electrochemical Polishing of Additively Manufactured Microchannels,” Journal of Engineering for Gas Turbines and Power, **143**(4), p. 041020.
[103] Bergman, T. L., Lavine, A., and Incropera, F. P., 2017, *Fundamentals of Heat and Mass Transfer*.
[104] Gnielinski, V., 1976, “New Equations for Heat and Mass Transfer in Turbulent Pipe and Channel Flow,” International Chemical Engineering, **16**(2), pp. 359–368.
[105] Kline, S. J., and McClintock, F. A., 1953, “Describing Uncertainties in Single Sample Experiments,” Mechanical Engineering, **75**, pp. 3–8.
[106] “Data Acquisition (DAQ) Systems, Devices & Software” [Online]. Available: https://www.ni.com/en-us/shop/data-acquisition.html. [Accessed: 10-Nov-2022].
[107] Baughn, J. W., Ireland, P. T., Jones, T. V., and Saniei, N., 1989, “A Comparison of the Transient and Heated-Coating Methods for the Measurement of Local Heat Transfer Coefficients on a Pin Fin,” J. Heat Transfer, **111**(4), pp. 877–881.
[108] Ekkad, S. V., and Han, J.-C., 1996, “Heat Transfer inside and Downstream of Cavities Using Transient Liquid Crystal Method,” Journal of Thermophysics and Heat Transfer, **10**(3), pp. 511–516.
[109] Wagner, G., Kotulla, M., Ott, P., Weigand, B., and von Wolfersdorf, J., 2005, “The Transient Liquid Crystal Technique: Influence of Surface Curvature and Finite Wall Thickness,” Journal of Turbomachinery, **127**(1), pp. 175–182.
[110] Rao, Y., and Xu, Y., 2012, “Liquid Crystal Thermography Measurement Uncertainty Analysis and Its Application to Turbulent Heat Transfer Measurements,” Advances in Condensed Matter Physics, **2012**, pp. 1–8.
[111] “Stereolithography,” 3D Systems [Online]. Available: https://www.3dsystems.com/on-demand-manufacturing/stereolithography-sla. [Accessed: 22-Mar-2020].
[112] “Resources For Thermographic Liquid Crystal Or TLC Products” [Online]. Available: https://www.hallcrest.com/color-change-basics/resources. [Accessed: 14-Mar-2020].

[113]Poser, R., von Wolfersdorf, J., and Lutum, E., 2007, "Advanced Evaluation of Transient Heat Transfer Experiments Using Thermochromic Liquid Crystals," Proceedings of the Institution of Mechanical Engineers, Part A: Journal of Power and Energy, **221**(6), pp. 793–801.
[114]Ekkad, S. V., and Han, J.-C., 2000, "A Transient Liquid Crystal Thermography Technique for Gas Turbine Heat Transfer Measurements," Meas. Sci. Technol., **11**(7), pp. 957–968.
[115]Schulz, S., Brack, S., Terzis, A., von Wolfersdorf, J., and Ott, P., 2016, "On the Effects of Coating Thickness in Transient Heat Transfer Experiments Using Thermochromic Liquid Crystals," Experimental Thermal and Fluid Science, **70**, pp. 196–207.
[116]2019, *MATLAB Version 9.6.0.1072779 (R2019a)*, The Mathworks, Inc., Natick, Massachusetts.
[117]Press, W. H., and Teukolsky, S. A., 1990, "Savitzky-Golay Smoothing Filters," Comput. Phys., **4**(6), p. 669.
[118]Savitzky, Abraham., and Golay, M. J. E., 1964, "Smoothing and Differentiation of Data by Simplified Least Squares Procedures.," Anal. Chem., **36**(8), pp. 1627–1639.
[119]"Temperature Data Loggers & Indicators for Wireless Monitoring | SpotSee" [Online]. Available: https://spotsee.io/temperature. [Accessed: 02-Oct-2022].
[120]Chyu, M. K., Hsing, Y. C., Shih, T. I.-P., and Natarajan, V., 1999, "Heat Transfer Contributions of Pins and Endwall in Pin-Fin Arrays: Effects of Thermal Boundary Condition Modeling," Journal of Turbomachinery, **121**(2), pp. 257–263.
[121]Chyu, M. K., and Natarajan, V., 1996, "Heat Transfer on the Base Surface of Threedimensional Protruding Elements," International Journal of Heat and Mass Transfer, **39**(14), pp. 2925–2935.
[122]"Ansys® Academic Research ICEM CFD, 2020 R1."
[123]"ANSYS CFX: CFD Software" [Online]. Available: https://www.ansys.com/products/fluids/ansys-cfx. [Accessed: 21-Mar-2020].
[124]Yang, L., Min, Z., Parbat, S. N., and Chyu, M. K., 2018, "Effect of Pore Blockage on Transpiration Cooling With Additive Manufacturable Perforate Holes," *Volume 2D: Turbomachinery*, American Society of Mechanical Engineers, Oslo, Norway, p. V02DT47A004.
[125]Kolář, V., 2007, "Vortex Identification: New Requirements and Limitations," International Journal of Heat and Fluid Flow, **28**(4), pp. 638–652.